UNIONE EUROPEA
Fondo europeo di sviluppo regionale

PON Ricerca e Competitività 2007-2013

UNIVERSITÀ DELLA CALABRIA

UNIVERSITA' DELLA CALABRIA

Dipartimento di fisica

Scuola di Dottorato

Bernardino TELESIO

Indirizzo

Mesofasi e Materiali Molecolari

Con il contributo del MIUR PON NANOFTALM

In co-tutela di tesi con:

UNIVERSITY OF TUNIS EL MANAR

Physics department

Supervisore: Prof. Abdelhafidh GHARBI

Firma

CICLO

XXIX

TITOLO TESI

Optical sectioning microscopies and Forester Resonance Energy Transfer as biological imaging techniques to overcome the problem of spectral overlap

Settore Scientifico Disciplinare FIS07

Direttore: Prof. Roberto BARTOLINO

Firma

Supervisore: Prof. Riccardo BARBERI

Firma

Dottorando: Dott./ssa Ramla GARY

Firma

Contents

Chapter 1

Introduction

1.1 Introduction and Context

The analysis of biological systems requires combined investigations into a wide array of fields such as mathematics, physics, engineering, and computer science in addition to the biological sciences. During the last decade, different modalities of biophysics imaging techniques including optical microscopy, ultrasound, Computed Tomography (CT), Magnetic Resonance Imaging (MRI), Positron Emission Tomography (PET), molecular probes like quantum dots and nanoshells, etc, have been increasingly used to enable the interplay of experimental and theoretical biology [1-8]. Nevertheless, approaches which derive from optical microscopy technique remain the most popular to achieve biological imaging. These approaches bring exquisite sensitivity and specificity to molecular imaging and provides new insights into biology and disease at the cellular and tissue level, with immediate relevance to clinical applications [9-14]. This chapter summarizes the most important challenges that must be overcome when acquiring images of biological tissues with the advanced optical microscopies. The chapter will conclude with a description of the thesis goals and structure.

1.2 The wide field fluorescence microscope

The wide field Fluorescence microscopy developed in the 80's, relying on the fluorescence phenomena to acquire only structures of interests, is one of specialized optical microscopes [15-18]. Although, the spatial resolution for such a microscope is limited for a sample with a thickness higher than about 2 µm [19]. The contribution of the emitted signal from regions outside the focal plane with the emitted signal from structures in the plane of interest to the resulting image introduces blurring and contrast reduction [20].

1.3 Optical sectioning microscopies

Therefore, to reduce the blurring effect and gain in resolution, more advanced optical microscopy techniques have been investigated, either by applying imagery treatment techniques as deconvolution methods or by modifying the hardware design [21]. These advanced optical microscopies, known as optical sectioning microscopies, are able to acquire images of thin slices of thick specimens providing greater contrast and permitting three dimensional reconstructions by computationally combining the image data from a stack of images [20].

Confocal scanning microscope, a form of optical sectioning microscope, has radically offered immense progress in cellular biology, neurosciences, medical research [22-38]. For this microscope, the background caused by out-of-focus light is eliminated from the image through a confocal aperture called "a pinhole" in the detection beam path [39,40]. Moreover, the lateral and axial resolutions of such a microscope are improved beyond what is achievable with the conventional wide field microscope. Although, this microscope has several limits mainly when observing live specimen with thickness higher than about 100 µm [41,42]. Therefore, two photons excitation, another optical sectioning microscopy techniques equipped with pulsed infrared lasers, is more suitable to achieve deeper penetration into samples because longer excitation wavelengths are less scattered in biological tissues. Thus, the emitted signal is not degraded by scattering within the sample.

Moreover, the confocal aperture is unnecessary in this case, because all of the fluorescent light originates from the laser focus spot. Also, due to the laser special confinement into a spot, photobleaching and photoxicity are reduced, which is ideal for live cell imaging. Nevertheless, usually with a multiphoton-setup it's possible to take advantage of another non-linear optical effect, second-harmonic generation (SHG) [43,44]. SHG-signal is generated from non-centrosymmetric structures that compose the biological tissues as collagen fibres, microtubules, the striation pattern of muscles and starch granules. By applying this technique, no staining with fluorescent dyes is needed. Thus, SHG microscopy is the adequate tool for the ex/in-vivo imaging of tissues containing non-centrosymmetric structures, since it avoids problems related to the use of fluorescent dyes, as the decrease of their concentration with deepness and their repeatedly exposure to high-illumination, which gives rise to photobleaching and photoxicity [45,46].
Thus, the choice of the most suitable optical sectioning microscopies technique to acquire biological imaging depends strongly on the thickness and viability of the specimen.

1.4 Spectral overlap challenge

In fact, when performing biological imaging experiments, several others important challenges, as the emitted signals spectral overlap or crosstalk, should be taken into consideration, mainly when analyzing the spatial localization of different structures within the same tissue, that emit fluorescence with highly overlapping spectra. Today, a wide range of available dyes, fluorescent proteins and labelling techniques, allows the creation of complex multicolored samples to study intracellular localization by the mean of advanced fluorescent microscope (confocal of two photon-excitation microscopes). Biological samples may contain then, a combination of two or more fluorophores, where each fluorophore labels a different component within the sample [47]. In the case of a significant overlap of the fluorophores used to label the structures, analysis of labeled components localization and colocalization is often perturbed resulting to an incapability for distinct fluorophores discrimination.

1.5 Practical limits of linear unmixing technique

To address this problem, increasingly, advanced instruments used for optical sectioning imaging features a combination of multi-spectral or multichannel detectors and linear unmixing software [47-49]. Such a combination improves the ability to maximize signal collection and to separate partially overlapping signals to define the differential emitted light distribution from more than one structure or molecular species within single cells or tissues [50-57]. Although this technique is a very powerful tool to reduce or eliminate signal cross talk in fluorescence microscopy when imaging multiply labeled specimens, one should also be aware of potential artifacts and errors that can be introduced when linear unmixing is applied without adhering to the proper experimental conditions. As for most other imaging setups, noise is also one of the greatest problems for linear unmixing [58]. Without having a proper signal-to-noise ratio then linear unmixing will not give satisfactory results. Therefore, it should be taken into consideration that the significant autofluorescence emitted from biological samples irradiated under some exciation wavelengths (e.g. UV/blue light in mammalian cells or green light in plant cells) and the mounting media produce a high background signal affecting then results with linear unmixing due to the low signal-to-noise ratio. It should be noted, also, that fluorescent probes having spectral profiles with an excessively high degree of overlap (in effect, almost completely), cannot be distinguished with spectral imaging and linear unmixing. In additions to the high background signal and the significant overlap pitfalls, performing linear unmixing adds several steps to the workflow of an experiment as production of reference samples, acquiring reference images, calculation of crosstalk and applying linear unmixing algorithms [58,48]. Thus, due to these limits and the relatively long procedure of this technique many researchers might be discouraged and move towards other techniques rather than unmixing [46,59].

1.6 Thesis goals

In this context, the purpose of this thesis is to demonstrate the use of novel approaches based on an imaging modalities combination of optical sectioning microscopies and another fluorescent technique in countering pitfalls arising from spectral overlap between emitted signals from features within biological tissues. The fluorescent technique of choice is the Forester Resonance Energy Transfer between gold nanoparticles and fluorescent dyes. The suitable combination of these techniques has been chosen accordingly to the thickness and the viability of the biological specimen.

1.7 Thesis structure

To expose this work, the manuscript is divided into six chapters. The first chapter provides an introduction to the work and describes briefly the advantages of optical sectioning microscopies technique in bio-imaging. The most common problems, challenges and limitation inherent in linear unmixing technique used to separate overlapping signal in studies of biological tissues are also addressed in this chapter.

The second chapter details the principles of optical sectioning microscopies used throughout the work by highlighting the benefits difference between these techniques which depends strongly on the thickness and the viability of the biological sample. The second part of this chapter will be focused on the principle description of an other fluorescent technique (FRET, Fluorescence Resonance Energy Transfer o Förster Resonance Energy Transfer), which has been used in conjunction through this work with the LSCM technique. In the last part, and as a FRET application, the role of the Surface Plasmon Resonance (SPR) of Gold NanoParticles GNPs in altering the fluorescence of dyes will be explored.

Chapter 3 investigates the feasibility of combining the SHG and TPEF microscopies techniques to acquire images within the human cornea, which is used as an example of a thick specimen close to *ex vivo* conditions. This techniques combination is the adequate tool to observe the different structures within cornea without any staining. This method

allows also a rapid observations of samples with little to no preparation and with a minimum of cross talk thanks to the endofluorescence properties of biomolecules such as NAD(P)H or flavins and second-harmonic generation. Finally, the three-dimensional reconstructions of the cornea anatomy is obtained, which shows the potential of this method in morphological studies of live and thick tissues.

Chapters 4 and 5 demonstrate the feasibility of LSCM to acquire images within thin and labeled tissues. Moreover, in these chapters, the compatibility of the FRET with LSCM to discriminate distinct fluorophores with highly overlapping spectra will be explored. In fact, the adequate choice of the GNPs and fluorophores combination with improved characteristics can help to reduce this problem. These chapters explore then, the use of FRET in order to enhance the performance of optical biosensors. In other words, the enhanced performance of LSCM technique through the employment of GNPs will be investigated. In chapter 4, skeletal muscle cells from lungfish *Protopterus annectens* are served as an example for the localization of microstructures within fixed tissues with a thickness of several micrometers. The features of interest are the endothelial-like NOS protein labeled with FITC. FRET in this case is based on an enhancement of fluorescence. The FITC detected fluorescence intensity from GNPs-labelled cells was brighter than the emission intensity from unlabelled cells, which makes these protein signal distinguishable from the autofluorescence signal.

In chapter 5, the LSCM is used in combination to FRET to observe the double stranded DNA induced aggregate growth of cationic surfactants-capped GNPs. The observation is based in this case on a fluorescence quenching process. Nile Blue perchlorate (NB) is used as probe because, in addition to the NB molecules ability to be intercalated inside the DNA helix, it seems that this probe can be also entrapped within the hydrophobic part of the surfactants bilayer films coating the aggregated GNPs. This entrapment place this probe at proximity to metallic surfaces leading to FRET. Due to the strong GNPs absorption light at around the plasma resonance, a highly quenching fluorescence is produced allowing the localization of GNPs aggregates, which is ideal to discriminate aggregated GNPs from DNA/cationic surfactants complexes, which have a strong light scattering overlap.

Finally, Chapter 6 summarizes the results achieved during the research and revisits the objectives of the work and discusses future perspectives.

References

[1] A. R. Kherlopian, T. Song, Q. Duan, M. A. Neimark, M. J Po, J. K. Gohagan and A. F. Laine. A review of imaging techniques for systems biology. *BMC Systems Biology*. 2008, 2:74.

[2] Y. Meng, C. C. Shaw, X. Liu, M. C. Altunbas, T. Wang, L. Chen, S. J. Tu, S. C. Kappadath, C. J. Lai. Comparison of two detector systems for cone beam CT small animal imaging: a preliminary study. *Society of Photo-Optical Instrumentation Engineers*. 2006, 6142:21188.

[3] R. Weissleder. Scaling down imaging: molecular mapping of cancer in mice. *Nature reviews*. 2002, 2 (1):11-18.

[4] P.K. Dhar, H. Zhu, S. K. Mishra. Computational approach to systems biology: from fraction to integration and beyond. *IEEE Trans Nanobioscience*. 2004, 3:144-152.

[5] J. A. Jense. Medical ultrasound imaging. *Prog Biophys Mol Biol*. 2007, 93 (1-3): 153-165.

[6] J. P. Christiansen, J. R. Lindner. Molecular and Cellular Imaging with Targeted Contrast Ultrasound. *Proceedings of the IEEE*. 2005, 93 (4): 809-818.

[7] G. M. Lanza, S. A. Wicklilne. Targeted ultrasonic contrast agents for molecular imaging and therapy. *Prog Cardiovasc Dis*. 2001, 44 (1): 13-31.

[8] W. A. Kalender. X-ray computed tomography. *Phys Med Biol*. 2006, 51 (13): R29-43.

[9] J. Folling, V. Belov, D. Riedel, A. Schonle, A. Egner, C. Eggeling, M. Bossi, S. W. Hell. Fluorescence nanoscopy with optical sectioning by two-photon induced molecular switching using continuous-wave lasers. *Chemphyschem*. 2008, 9 (2): 321-326.

[10] R. Pepperkok, J. Ellenberg. High-throughput fluorescence microscopy for systems biology. *Nature reviews*. 2006, 7 (9): 690-696.

[11] K. Konig K. Multiphoton microscopy in life sciences. *J Microsc*. 2000, 200 (2): 83-104.

[12] E. M. Hillman. Optical brain imaging *in vivo*: techniques and applications from animal to man. *J Biomed Opt*. 2007, 12 (5): 051402.

[13] E. M Hillman, A. Devor, M. B. Bouchard, A. K. Dunn, G. W. Krauss, J. Skoch, B. J. Bacskai, A. M. Dale, D. A. Boas. Depth-resolved optical imaging and microscopy of vascular compartment dynamics during somatosensory stimulation. *Neuroimage*. 2007, 35 (1): 89-104.

[14] X. Chen, R. F. Murphy. Location proteomics: determining the optimal grouping of proteins according to their subcellular location patterns as determined from fluorescence microscope images. *Signals, Systems and Computers*. 2004, 1: 50-54.

[15] K. R. Spring, M. W. Davidson. Introduction to Fluorescence Microscopy. *Nikon MicroscopyU*. Retrieved, 2008, 09:28.

[16] A. D. Boas, C. Pitris, N, Ramanujam. *Handbook of biomedial Optics*.

[17] Y. Wang, L. Taylor. Fluorescence Microscopy of Living Cells in Culture.

[18] W. K. Dunn, M. M. Kamocka and J. H. McDOnalds. A practical guide to evaluating colocalization in biological microscopy. *Am J Physiol Cell Physiol*. 2011, 300(4): C723–C742.

[19] T. Wilson, Optical Sectioning in Confocal Fluorescence Microscopes, *Journal of Microscopy*, 1989, 154: 143-156.

[20] J. A. Conchello and J. W. Litchaman. Optical sectioning microscopies. *Nature methods*. 2015, 2 (12): 920-931

[21] P. J. Shaw. Comparison of Widefield/Deconvolution and Confocal Microscopy for Three-Dimensional Imaging. *Handbook of Biological Confocal Microscopy*, third edition, edited by James B. Pawley, SpringerScience+Business Media, New York, 2006.

[22] J. B. Pawley (ed.). Handbook of Biological Confocal Microscopy. *New York: Plenum Press*. 1995.

[23] S. W. Paddock (ed.). Confocal Microscopy: Methods and Protocols. *Totowa, New Jersey: Humana Press*. 1999.

[24] A. Diaspro (ed.). Confocal and Two-Photon Microscopy: Foundations, Applications, and Advances. *New York: Wiley-Liss*. 2002.

[25] B. Matsumoto (ed.). Cell Biological Applications of Confocal Microscopy, in Methods in Cell Biology. Volume 70, *New York: Academic Press*. 2002.

[26] C. J. R. Sheppard and D. M. Shotton. Confocal Laser Scanning Microscopy. *Oxford, United Kingdom: BIOS Scientific Publishers*.1997.

[27] M. Müller. Introduction to Confocal Fluorescence Microscopy. *Maastricht, Netherlands: Shaker*. 2002.

[28] A. R. Hibbs. Confocal Microscopy for Biologists. *New York: Kluwer Academic*. 2004.

[29] P. M. Conn. Confocal Microscopy. *in Methods in Enzymology, Volume 307, New York: Academic Press*. 1999.

[30] T. R. Corle and G. S. Kino. Confocal Scanning Optical Microscopy and Related Imaging Systems. *New York: Academic Press*. 1996.

[31] T. Wilson (ed.). Confocal Microscopy. *New York: Academic Press*. 1990.

[32] M. Gu. Principles of Three-Dimensional Imaging in Confocal Microscopes. *New Jersey: World Scientific*. 1996.

[33] B. R. Masters (ed.). Selected Papers on Confocal Microscopy. SPIE Milestone Series, Volume MS 131, Bellingham, Washington: *SPIE Optical Engineering Press*. 1996.

[34] W. T. Mason. Fluorescent and Luminescent Probes for Biological Activity. *New York: Academic Press*. 1999.

[35] E. J. G. Peterman, H. Sosa, and W. E. Moerner. Single-Molecule Fluorescence Spectroscopy and Microscopy of Biomolecular Motors. *Ann. Rev. Phys. Chem*. 2004, 55: 79-96.

[36] R. D. Goldman and D. L. Spector. Live Cell Imaging: A Laboratory Manual. *New York: Cold Spring Harbor Press*. 2005.

[37] W. B. Amos and J. G. White. How the Confocal Laser Scanning Microscope entered Biological Research. *Biology of the Cell*. 2003, 95: 335-342.

[38] D. K. Hamilton and T. Wilson, Scanning Optical Microscopy by Objective Lens Scanning. *Journal of Physics E: Scientific Instruments*. 1986, 19: 52-54.

[39] Minsky,M. Memoir on inventing the confocal scanning microscope. *Scanning.*1988, 10 : 128-139.

[40] M. Minsky. Microscopy Apparatus. *US Pat*. 3,013,467, 1961

[41] A. Diaspro (ed.). Confocal and Two-Photon Microscopy: Foundations, Applications, and Advances, New York: *Wiley-Liss*, 2002.

[42] M. Oheim, D. J. Michael, M. Geisbauer, D. Madsen, R. H. Chow. Principles of two-photon excitation fluorescence microscopy and other nonlinear imaging approaches. *Advanced Drug Delivery Reviews.* 2006, 58: 788–808.

[43] L. Moreaux, O. Sandre, S. Charpak, M. Blanchard-Desce, J. Mertz. Coherent scattering in multi-harmonic light microscopy. *Biophys. J*. 2001, 80:1568–1574.

[44] N. Moreno, J.A. Feijo, G. Cox. Implementation and evaluation of a detector for forward propagated second harmonic signals. *Micron*. 2004, 35 : 721–724.

[45] C. Ricard, B. Vacca, P. Weber. Three-dimensional imaging of small intestine morphology using non-linear optical microscopy and endogenous signals. *J. Anat*. 2012, 221: 279–283

[46] H.-H. Lin, K.H. Kim, W. Lo, Y. Sun, W.-C. Lin, S.-J. Lin, S.-H. Jee, P.T.C. So, C.-Y. Dong. Multiphoton Autofluorescence and Second-Harmonic Generation Imaging of the Ex Vivo Porcine Eye. *IOVS.* 2006, 47(3) :1216-1224.

[47] T. Zimmermann . Spectral Imaging and Linear Unmixing in Light Microscopy. Chapter Microscopy Techniques Volume 95 of the series Advances in Biochemical Engineering : 245-265.

[48] B. Kraus, M. Ziegler and H. Wolff . Linear fluorescence unmixing in cell biological research. Modern Research and Educational Topics in Microscopy. A. Méndez-Vilas and J. Díaz (Eds).

[49] T. Haraguchi1, T. Shimi, T. Koujin, N. Hashiguchi1 and Y. Hiraoka. Spectral imaging fluorescence microscopy. *Genes to Cells*. 2002, 7: 881–887.

[50] B. R. Frieden. Image enhancement and restoration, In picture processing and image filtering (ed. Huang, T.S.) *Springer-Verlag, New York.* 1975,179-248

[51] J. G. McNally, C. Preza, J-A, Conchello and L. J. Thomas. Artifacts in computational optical microscopy. *J. Opt. Soc. Am. A.* 1994, 11:1056-1067.

[52] D. A. Agard. Optical sectioning microscopy. *Annu. Rev. Biophys. Bioeng*. 1984, 13 : 191-219.

[53] W. A. Carrington. Image restoration in 3D microscopy with limited data in Bioimaging and two-diemnsional spectroscopy (ed. Smith, L. C) 72-83(SPIE press, Bellingham, Washington, 1990)

[54] Carrington, W. A and Fogarty. K. E. (US patent 5047968,1991).

[56] T. J. Holmes. Maximum-likehood image restoration adapted for noncoherent optical imaging. *J. Opt. Soc. Am*. 1988, A 5: 666-673.

[57] T. J. Holmes and Y-H. Liu. Richardson-Lucy/maximum likehood image restoration algorithm for fluorescence microscopy: further testing. *Appl. Opt*. 1989, 28: 4930-4398.

[58] http://zeisscampus.magnet.fsu.edu/articles/spectralimaging/considerations.html."Practical considerations for spectral imaging, Zeiss"

[59] Application Note. Imaging of Fluorescent Proteins. Visitech international . Vision Technology for Science.

Chapter 2

Theoretical background

2. 1 Introduction

This chapter describes principles of imaging modalities used throughout the work. In the first section of this chapter, the basic theory and concepts of confocal and nonlinear microscopies technique will be discussed. The focus of this section is concentrated on the ways in which the three techniques differ from each other, thus highlighting the advantages and disadvantages. The second part of this chapter will be dedicated for the description of the principle of an other fluorescent technique, which is the forester resonance energy transfer (FRET). Factors that influence this effect will be defined. In the last section of this chapter, the role of the surface plasmon resonance (SPR) of GNPs in altering the fluorescence of dyes will be explored as a FRET application.

2.2 Optical sectioning microscopies

2.2.1 Laser scanning confocal microscope

2.2.1.1 Principle

The laser scanning confocal principle is diagrammatically presented in Figure 2.1. The excitation light is directed by the scanning mirror and focused into the specimen via the objective lens. The fluorescent emission is separated from the excitation by the combination of the dichroic mirror and the barrier filter. Before reaching the detector, emitted light from the location of the scanning spot crosses the pinhole. As shown in Figure 2.2, the scanning spot is at the center of the in-focus-plane. Light emitted from the in-focus plane (solid lines) is focused into the confocal pinhole located in the image plane. Light not emitted from the location of the scanning spot is rejected since it's focused on the opaque portions of the pinhole aperture. The out-of focus emitted light (dashed lines) from planes below or above the in-focus plane are focused respectively in front or behind the aperture plane. Thus, most of this extraneous light is not detected by the photomultiplier and it does not contribute to the resulting image. Because this microscope requires scanning the illumination spot and due to the location of the pinhole aperture, which is conjugated to the focal point of the objective lens, the instrument is called a confocal scanning microscope [1-3].

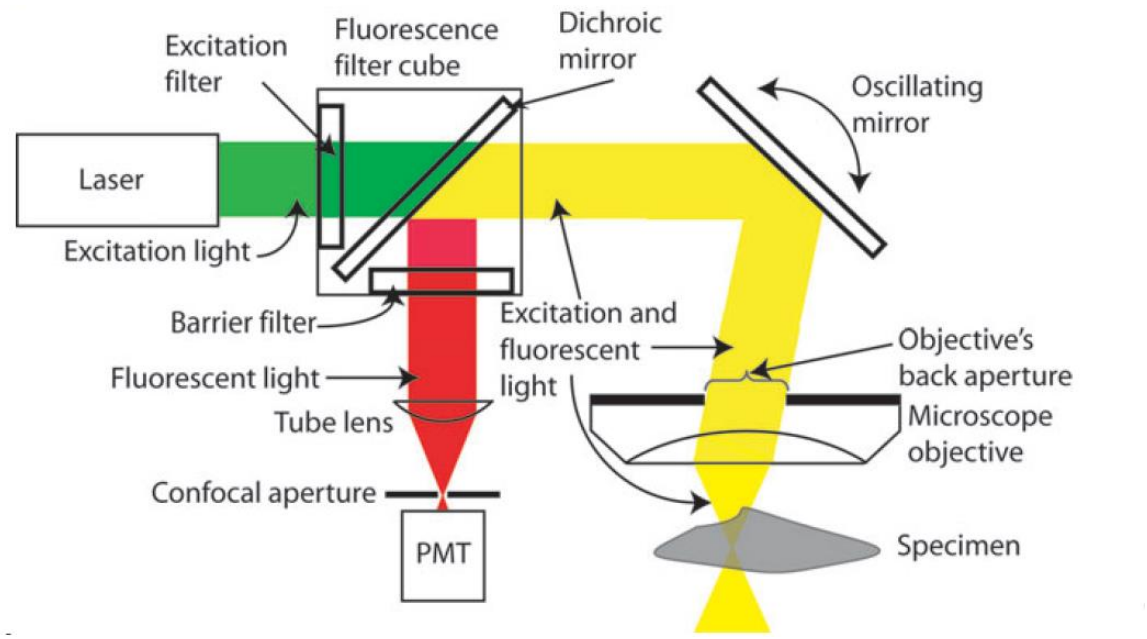

Figure 2.1: Layout of the laser scanning confocal microscope [1]

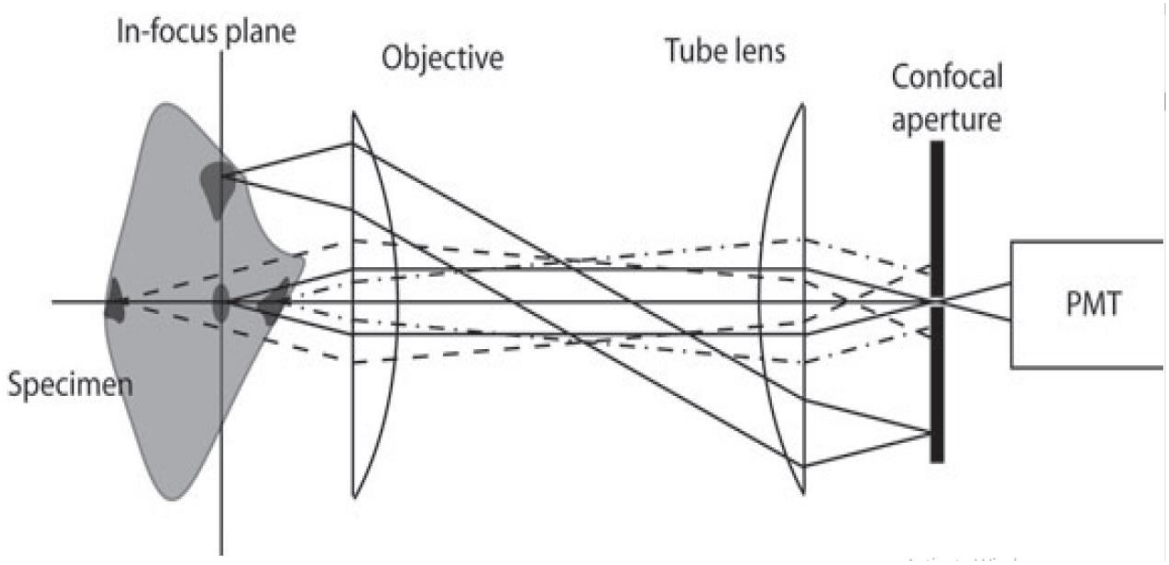

Figure 2.2 : The pinhole role : rejecting the out-of-focus light [1]

2.2.1.2 Comparison with the wide field fluorescence microscope

- **Illumination**

When contrasting the similarities and differences between widefield and confocal microscopes, it is often useful to compare the character and geometry of specimen illumination utilized for each of these techniques. As shown in Figure 2.3, in traditional widefield epi-fluorescence microscopy, a large volume of the specimen is subjected to an intense, uniformly and simultaneously illumination from an incoherent mercury or xenon arc-discharge lamp. Via the objective, the excitation light is focused into a wide cone within the specimen. The emitted background light generating from the outside of the focal plane contributes to the image formation [4,5].

In the case of confocal microscopy, the laser is (coherent light) used as the light source for excitation which is focused into a much more smaller cone within the specimen via the objective. Thus, to make an image, the scope needs to sample each spot within the specimen plane with the same way through the system of two galvanometric mirrors [3,6]. The spot size is determined by the microscope design, wavelength of incident laser light, objective characteristics, scanning unit settings, and the specimen [4]. The diffraction limited size ranges from approximately 0.25 to 0.8 micrometers laterally (depending upon the objective numerical aperture) and 0.5 to 1.5 micrometers axially.

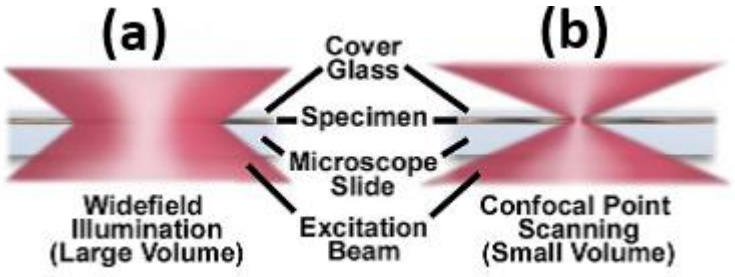

Figure 2.3: a comparison between the typical illumination cones of a widefield (Figure 2.3(a)) and point scanning confocal (Figure 2.3(b)) microscope at the same numerical aperture.

- Point spread function and resolution

As discussed in the previous paragraph, due to the one spot illumination/scanning mode in the plane of focus center used in confocal microscopy technique in conjunction with an aligned pinhole in a conjugate plane in the return light path, the detected light originates only from one spot scanned in one plane. This method, provides excellent contrast because if the exciting light is focused on a spot within a region of the sample free from fluorophores, a dark area is detected. Whereas, in the presence of fluorophores, only light emitted from those fluorophores where the spot is focused, is detected. The accumulated result is a dramatic improvement in contrast and a thin optical section [7-9].

In fact, the concept of resolution is inseparable from contrast, and is defined as the minimum separation between two points that results in a certain level of contrast between them [10]. The properties of the intensity Point Spread Function (PSF) in the image plane as well as in the axial direction are major factors in determining the resolution of a microscope.

i. Point spread function

The intensity PSF is the visible image of the point source formed in the microscope and recorded by its imaging system. In 3D, the PSF of the wide field fluorescence microscope has the shape of a double cone structure modulated by diffraction Airy ring pattern and having their apexes united at the point source, rendering an hourglass shape. Figure 2.4 shows a measured PSF with a wide field microscope having an oil immersed objective with a numerical aperture of 1.3.

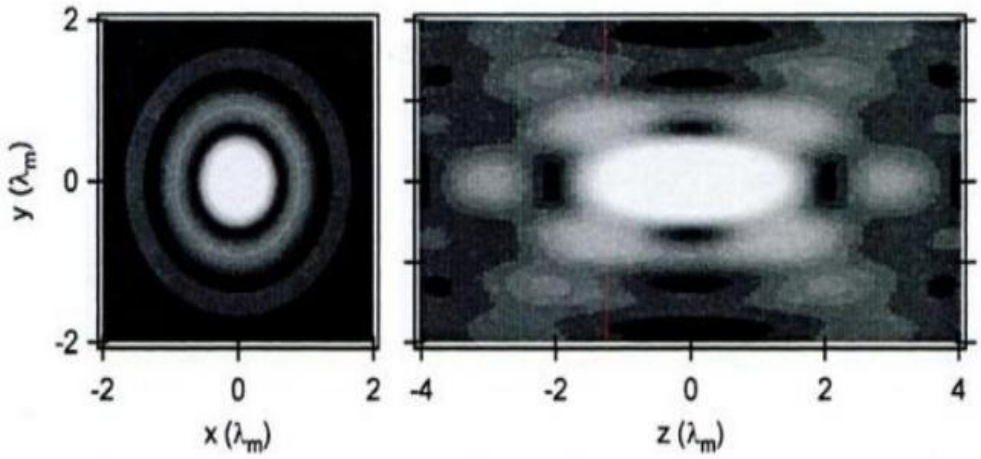

Figure 2.4: Wide field fluorescence microscope focal-field intensity distribution according to diffraction theory for focusing with an oil-immersion microscope objective with NA = 1.3. The left panel shows a lateral plane, i.e., perpendicular to the optical axis. The right panel shows an axial plane centered on the optical axis [11].

For a confocal microscope, due to the presence of the pinhole, the imaging becomes a two steps process [12]. Firstly, the microscope objective focuses laser light onto the specimen and after that, the microscope objective images the generated fluorescence onto the detection pinhole. The hole process, excitation and confocal detection can be described then by a single confocal PSF, which is the product of excitation and emission/detection PSF.

$$PSF_{conf}(x, y, z) = PSF_{exc}(x, y, z) \cdot PSF_{det}(x, y, z)$$

This product provides a significant reduction in the intensity of the side lobes and a narrower bandwidth of the PSF [12,13]. Figure 2.5 shows the confocal PSF distribution in the lateral and axial plane according to diffraction theory for focusing with an oil-immersion microscope objective with a numerical aperture of 1.3. The effect of the detection pinhole is demonstrated even more clearly in this figure, where the entire lateral side lobe structure is suppressed, whereas some axial contributions remain [11].

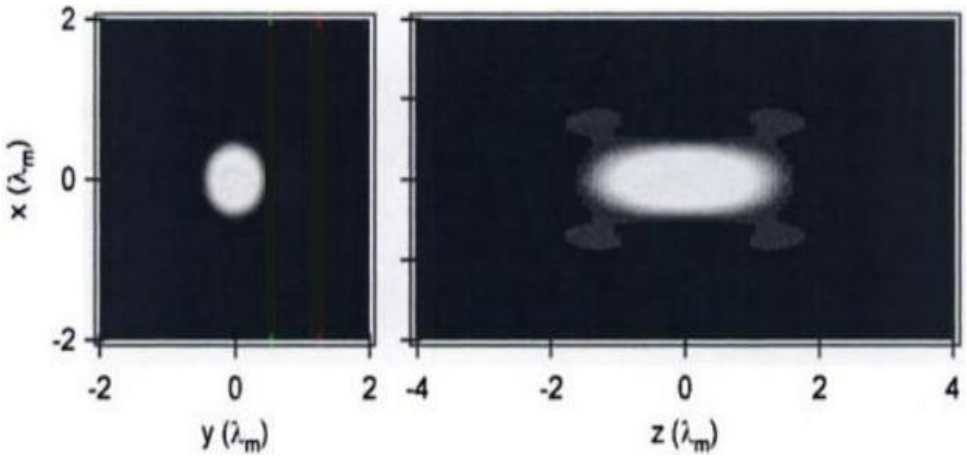

Figure 2.5: LSCM focal-field intensity distribution according to diffraction theory for focusing with an oil-immersion microscope objective with NA = 1.3. The left panel shows a lateral plane, i.e., perpendicular to the optical axis. The right panel shows an axial plane centered on the optical axis [11].

ii. Resolution:

- lateral resolution:

The beam quality is typically ensured by using a single mode optical fiber to deliver the excitation laser light as a Gaussian point source, which is then collimated and focused into a diffraction-limited beam [10,13]. In an aberration-free imaging system, obtained by using the highest quality optical elements, the size of this focus spot, assuming uniform illumination, is a function of excitation wavelength (λ_{EX}) and Numerical Aperture (NA) of the objective lens, as seen in the following equation :

$$Spot\ Size = \frac{1.22\lambda_{EX}}{NA}$$

Resolution can be defined as the separation distance at which two objects are imaged with a certain contrast value. It is common, however, to specify that greater contrast is necessary to adequately distinguish two closely spaced points visually, and the well-known Rayleigh criterion for resolution states that two points of equal intensity should be considered to be just resolved when the principal intensity maximum of one Airy disk

coincides with the first intensity minimum of the second Airy disk. In general, r_0 is used to define the lateral resolution in a wide field fluorescence microscope, which is also the half of the diffraction limited spot size [10,13]. Thus, from the previous equation, r_0 can be deducted as the following:

$$r_0 = 0.61\,\lambda / NA$$

As previously mentioned, due to the presence of the pinhole in the case of confocal microscopy, the resolution is determined by the product of the excitation and detection PSF. In fact, the excitation and detection PSF are equal in shape but slightly different in dimension, due to the Stokes shift between excitation and detection ($\lambda_{exc} < \lambda_{det}$). Using classical theory and assuming for simplicity, equal excitation and detection wavelengths ($\lambda_{exc} = \lambda_{det}$), the confocal PSF is then the square of the PSF of excitation:

$$PSF_{conf} = |PSF_{exc}|^2$$

In this case, the intensity distribution of the central Airy disk is narrowed due to this squaring (Figure 2.6) .

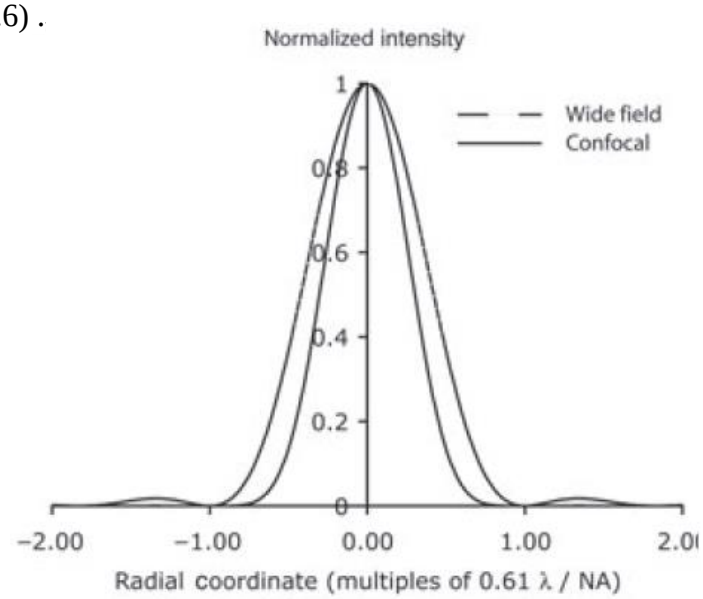

Figure 2.6 :PSF of the wide field and confocal microscopes [13]

The Rayleigh criterion cannot be used directly to define the resolution in confocal microscope because the position of the first minimum in the distribution has been changed [10]. Therefore, since that the position of the maximum didn't change, the distance in x or in y that connects the 50 % intensities on both sides of an intensity profile, which is called the "Full Width Half Maximum" (FWHM), is used to define the resolution in confocal microscope [13-16](Figure 2.7). As a reasonable approximation, the width of the lateral distribution ($FWHM^r$) equals the distance to the first minimum,

$$FWHM^r \sim r_0$$

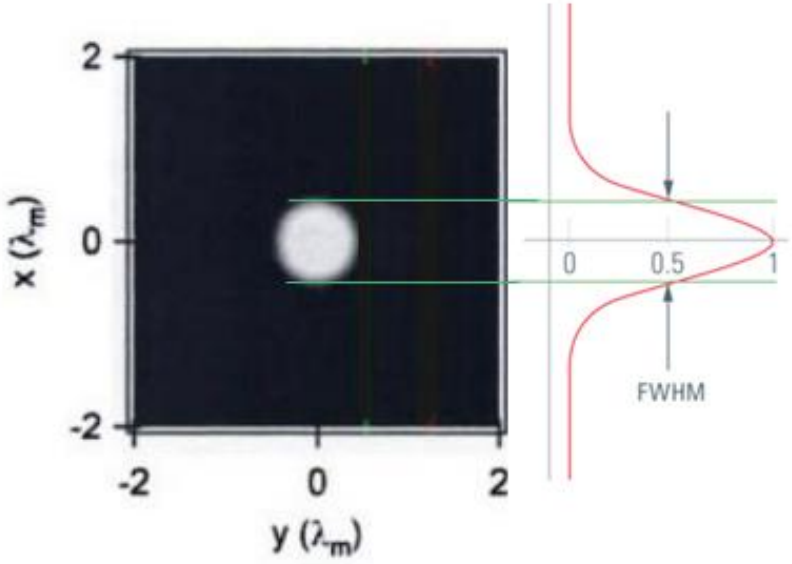

Figure 2.7: Full Width Half Maximum (FWHM) of the intensity profile in x direction is used to define the resolution in LSCM. The point spread function – generated by a sufficiently small latex bead – is recorded by collecting the intensity in an xy profile section. The intensity profile in the center of the diffraction pattern is displayed (here in red) and the distance in z between the 50% intensities values is measured (green indicators)[13]

The FWHM of the lateral confocal PSF ($FWHM^r_{conf}$) is then determined by the square of the excitation PSF and hence

$$FWHM^r_{conf} \sim \frac{1}{\sqrt{2}} FWHM^r_{exc}$$

$$\sim 0.37\,\lambda/NA$$

The $\frac{1}{\sqrt{2}}$ factor is derived after assuming a Gaussian-shaped PSF. The lateral resolution of confocal microscope is then optimized by this factor compared to the lateral resolution of the widefiled microscope [14,17].

- **Axial resolution**

The dramatic reduction of the wings intensity for the axial PSF distribution of the confocal microscope, as shown in the previous Figure, offers the optical sectioning capability advantage over the wide field microscope. The optical sectioning properties of the confocal microscope result from the characteristics of the integrated intensity point spread function, which has a maximum in the focal plane when evaluated as a function of depth. The equivalent integral of intensity point spread function for the conventional widefield microscope is constant as a function of depth, producing no optical sectioning capabilities [15,14].

The axial resolution for confocal microscopy corresponds to the thinnest section achievable depending on limitations by optical diffraction. In the literature, a variety of equations are presented that pertains to different models for calculating axial resolution for various microscope configurations. The ones most applicable to fluorescence emission are similar in form to the expressions evaluating depth of field [14]. In fact the axial resolution depends on several parameters. The most obvious is the wavelength, which controls the size of the PSF proportionally. The shorter the wavelength, the thinner the slice. The second parameter is NA of the objective lens. The higher the NA, the thinner the optical section. The axial resolution depends also on the refractive index of medium affecting then the sectioning performance. The dependence of the slice's size *dz* on these parameters is given by the following formula :

$$dz \cong \frac{0.64 \cdot \lambda_{exc}}{n - \sqrt{n^2 - NA^2}}$$

The third parameter is the pinhole diameter in the detection path, which is assumed to be zero for the formula given above. Therefore, this formula gives the best value one can expect for fluorescence imaging, which is of course only of theoretical interest because for a pinhole with zero diameter it's impossible to generate bright images. Also, in practice, when the pinhole diameter is restricted, resolution and confocality are improved, but the amount of signal reaching the detector is reduced. Therefore to have a good balance between signal strength, resolution and confocality, the pinhole diameter is usually set to be 1 Airy. Taking into consideration all these parameters with a suitable setting helps to estimate the performance of confocal microscope to acquire images with thin slices (optical section) that can reach a thickness down to 0.5 µm through a thick specimen [1]. These optical sectioning capabilities provides greater contrast and permits three-dimensional reconstructions by computationally combining the image data from a stack of images.

2.2.1.3 Fluorophores

The confocal microscope relies as any fluorescence microscope on the use of fluorescence to provide image contrast in order to detect the distribution of proteins or other molecules of interest. Sometimes called dyes, probes, stains or labels, the fluorophores may be naturally be present in the specimen, in which case the intrinsic fluorescence is denoted by autofluorescence, or be artificially added [13,18]. In fact, there is a diverse range of techniques for fluorescent staining of biological samples. These techniques are based on a chemical bonds between fluorophores and the target of interest [19,20]. Fluorophores with high specificity to functional groups of the features of interest can be attached directly or via the intermediary of an antibody through the immunofluorescence technique. This section provides the absorption and fluorescence processes characteristics of the fluorophore.

- **Absorption**

In the absorption process, energy is transferred from the light field (i.e. the photons) to matter (i.e. the atoms and molecules). For a typical fluorophore, the absorption of the

photon brings the molecule from its ground state to the first electronically excited state. In another words, the energy of the exciting photon has to approximately match the energy difference between the excited state and the ground state (Figure 2.8). At room temperature, absorption of a photon takes place from the vibrational ground state S_0 within $\sim 10^{-18}$ s. The energy of a photon is given by:

$$E = \frac{h}{\nu} = \frac{hc}{\lambda}$$

Where *h* is Plank's constant, *c* is the light speed, λ is the light wavelength, and ν is its frequency. The energy of the photon is of the order of $2.8 \times 10^{-19} - 5 \times 10^{-19}$ J for visible light. In a typical fluorescing molecule, this amount of energy is sufficient for an electronic energy transition. In fact, this absorption of visible light gives a fluorophore its color.

- Fluorescence

Fluorescence occurs when a photon is absorbed by a fluorophore, raising an electron to an excited energy state, from which it relaxes to the electronic ground state and emits a lower energy photon (Figure 8). In fact, due the process of internal conversion, the surrounding molecules (solvents) absorb the excess of energy as heat. Therefore, the molecules quickly relaxes to the lowest energy level of electronically excited state. From this level, the electronically excited molecule loses part of the remaining excess molecular energy by emitting in a random direction a photon with an energy of $h\nu_{flu}$. Thus, the molecule fluoresces, thereby returning to the lowest electronic state. This emitted fluorescent photon is of lower energy (i.e., longer wavelength) than the photon originally absorbed, a phenomenon known as the Stokes shift (Figure 2.9).

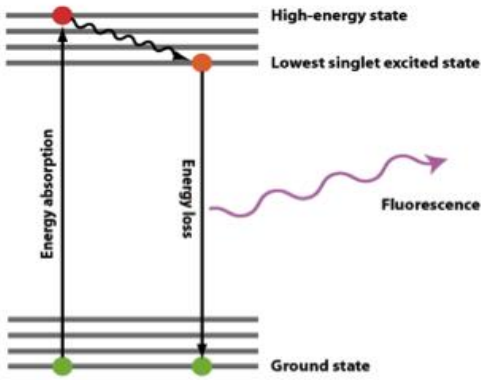

Figure 2.8 : The Jablonski diagram of a typical fluoresceing molecule. The electronic energy levels and their vibrational substructure are shown with horizontal lines, and the physical processes that cause transitions between these levels are depicted by vertical arrows.

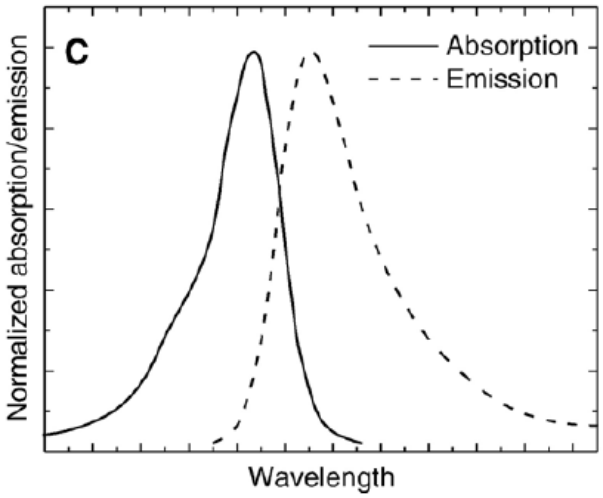

Figure 2.9 : Schematic drawing of the absorption and fluorescence emission spectra of a fluorophore. Spectra are normalized to peak absorption and emission, respectively [21].

2.2.1.4 Potential problems

Despite the several advantages offered by the LSCM microscope, when working with biological samples, serious problems can occur mainly when imaging details within a relatively thick layer of tissue or for a specimen with live cells [22,23].

- Depth limit

In fact, when imaging in thick samples, there is a fundamental limit to the depth at which images can be effectively acquired. As the imaging depth is increased, a greater proportion of the light will scatter. The excitation and emission photons must travel through the tissue where molecular interactions will change their directions. In the presence of scattering, some fluorescence generated at the focus will scatter outside of the confocal pinhole and not be detected. Moreover, some of the excitation light will be lost through scattering before reaching the out-of-focus, reducing then the amount of fluorescence detected from the focus. Thus, the fluorescence, the absorbance and excitation signals are increasingly weak with deepness due to the strong light scattering within thick specimen, which will reduce the signal in the image [24]. The background signal is increased due the detection of a high amount of light scattering which originates from a random location resulting to a severely reducing of image contrast.

- Photobleaching and phototoxicity

The use of confocal microscopy requires a bright exciting laser to allow an adequate signal-to-noise ratio because the confocal aperture blocks most of the light emitted by the tissue, including light generated from the plane of focus. When observing living specimen, the strong incident light decreases the viability of the specimen due to the phototoxicity [25]. In fact, several fluorescent dye molecules generate cytotoxins like singlet oxygen or free radicals. Therefore one must limit the scanning time or light intensity to keep the specimen alive. The use of the LSCM brings with it another problem when using a strong incident light : the photobleaching. This light causes fluorescent dyes to fade within minutes of continuous scanning. Thus the fluorescence signal weakens as subsequent scans are made, either to produce a three dimensional image or to observe a single slice at several time points [1, 24].

2.2.1 Nonlinear microscopies

2.2.2.1 Two photons excitation microscope

In this paragraph, the presentation of the basic concepts of Two Photons Excitation Fluorescence (TPEF) microscope will be based on a comparison with the confocal microscope. In the first section, the principle of TPEF microscopy will be discussed. The equipment needed for a typical application of this technique will be then described. In the third section the TPEF benefits will be presented.

- Principle

The theoretical basis of the two-photon excitation concept was proposed in 1931, by Maria Göppert-Mayer in her doctoral dissertation [26]. In 1963, this photophysical effect was then observed experimentally after the invention of the laser by Kaiser and Garret [27].

Contrary to the conventional one-photon excitation process, which involves exciting a fluorophore from the electronic ground state (S_0) to an excited stated (S_1) by a single photon, two-photon excitation is generated by a simultaneous absorption of two photons (Figure 2.10). The one photon-excitation process requires photons in the ultraviolet or blue/green spectral range. After a short period of time in the excited state, the excited fluorophore relaxes back to its ground state by emitting a photon of light. To efficiently excite the fluorophore, the excitation photon should have a wavelength (λ_{1p}) that corresponds to an energy which matches the energy of the excited state of the fluorophore (E_{S1}).

$$E_{S1}\text{-}E_{S0} = \frac{hc}{\lambda_{1p}}$$

Since the fluorescence emission after two-photon excitation is exactly the same as that generated in normal one photon excitation [28], each absorbed photon have a wavelength

(λ_{2p}) (typically in the infrared spectral range) of approximately twice that of the photon required to achieve transition under one-photon excitation.

$$E_{S1}\text{-}E_{S0} = 2\,\frac{hc}{\lambda_{2p}}$$

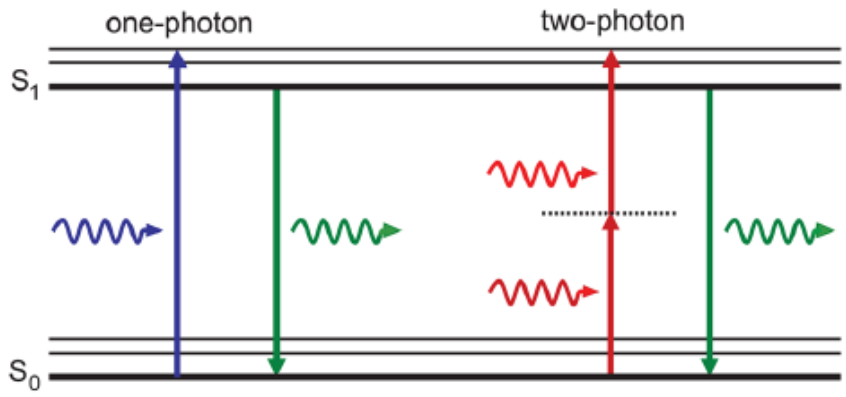

Figure 2.10: Energy diagram of fluorescence with 1-photon and 2-photon excitations [24]

- **Design of two photons microscope**

A schematic drawing of typical components in a two-photon microscope is presented in (Figure 2.11). This system typically consists of a high-peak-power pulsed laser, a high-throughput scanning microscope and high-sensitivity detection circuitry [29]. A pinhole, as in the case of confocal microscope, is not required.

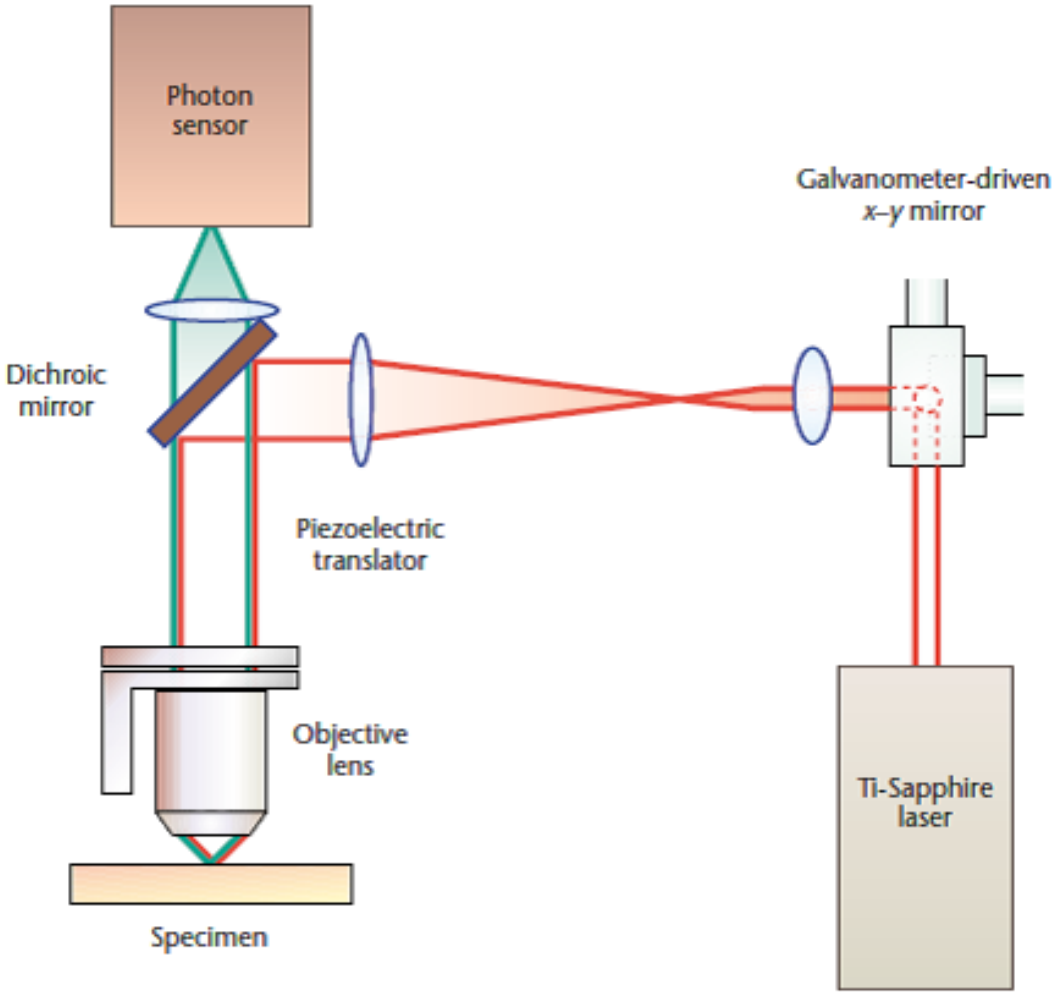

Figure 2.11: A schematic drawing of typical components in a two-photon microscope. This system typically consists of a high-peak-power pulsed laser, a high-throughput scanning microscope and high-sensitivity detection circuitry [29].

i. Laser

The two photon excitation requires an absorption of photons at exactly the same time, within ~ 10^{-18} s. Thus, compared to one photon excitation, a much higher photon flux is necessary (~10^6 times more) to have a significant probability for a fluorophore to be

excited by two photons at the same time. Therefore the laser source should have a higher power compared to that used in a single photon excitation [28,30]. However, the high average laser power is a concern for pigmented biological samples with appreciable one-photon absorption. Therefore, high repetition rate (100 MHz), ultrafast (femtosecond or picosecond pulse widths) lasers, such as titanium–sapphire and Nd:YLF lasers are the best candidates as light sources for two-photon excitation. For these lasers, photons are concentrated into discrete pulses, such that the peak power of the pulse is enhanced relatively to the time-averaged power. Therefore, there is a much greater probability for a fluorophore to absorb two photons simultaneously. The higher peak power and the lower duty cycle of these lasers minimize average power deposition in the specimen while maximizing two-photon excitation efficiency.

ii. Pinhole

For one-photon excitation, the spatial resolution of the image is increased through an adjustable pinhole in front of the detector by rejecting the out-of focus fluorescence signals, that are generated equally from each z-section above and below the focal plane. Whereas, using the two-photon excitation microscope, the out of focus fluorescence is never generated. Thus, the two-photons excitation provides optical sectioning without the need to introduce a pinhole in the detection path of the microscope.

As shown in Figure 2.12, when photon flux is sufficiently high to give rise to two-photon absorption, excitation (and thus emission) is confined to a small ellipsoidal volume around the focal point resulting from the quadratic dependence of the fluorescence probability on the spatial distribution of the excitation radiance [31,32].

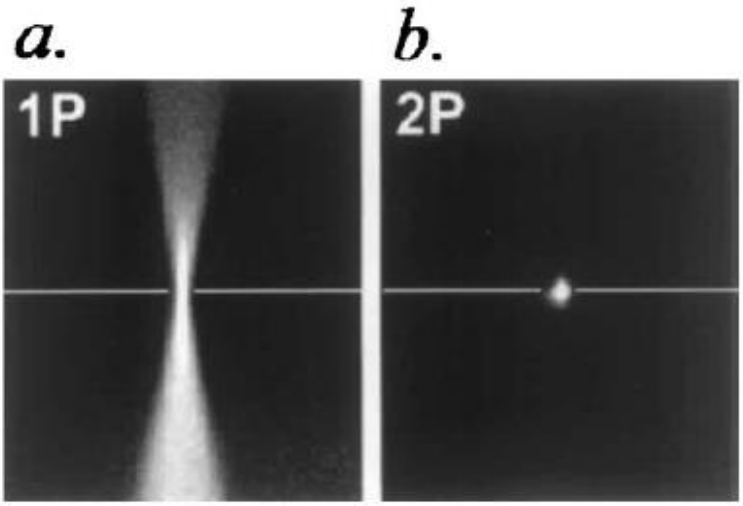

Figure 2.12 : Localization of two-photons excitation. Distribution of fluorescein fluorescence in the *x-z* plane during single photon (1P) excitation by focused 488-nm laser light (a) and during two-photon (2P) excitation using femtosecond pulses of 850nm light (b). The sample was illuminated through the same objective lens during one and two-photon excitation. White lines indicate plane of focus [32].

iii. Non descanned detectors

In two-photon excitation microscope, the fluorescence only originates from a point in the focal plane. Therefore, for thinner samples, it's possible to use the same descanned detection system in confocal microscope by opening the pinhole as maximum as possible. Such a detection is insufficient for imaging within thicker samples. In fact, signal attenuation is the major inconvenient when imaging deeper within biological tissues, due to the strong light scattered by such specimens [30,33,34].

Upon the intrinsic confocality of the descanned method, the scattered light can exit the sample at a high off-axis angle and thus miss the detector, and not be detected, after traversing the relatively long optical path back through the scanning optics. Therefore, in the two-photon excitation microscope, descanning the emitted signal is unnecessary. A detector, which is able to detect as much as possible emitted light, particularly scattered light should then be used. Higher collection efficiency can be ensured by the extremely short coupling of detectors to minimize the detection path length. Therefore some of the newest confocal microscopes place a PhotonMultiplier Tube (PMT) immediately after the objective for using large photo sensor areas, as found in external detectors, which can be

coupled indirectly behind the objective (Reflected Light Detector) or directly behind the condenser (Transmitted Light Detector) [24,33](Figure 2.13).

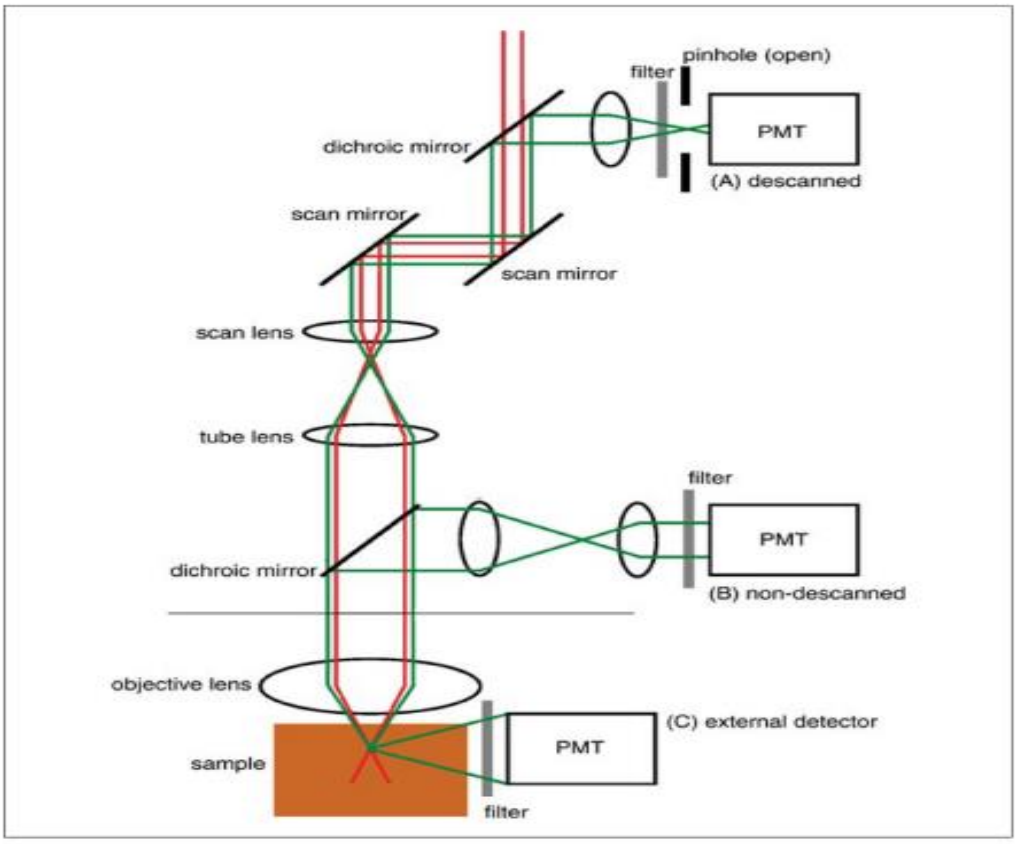

Figure 2.13 : Descanned and nondescanned detection for two-photon excitation. Laser beam is scanned (*x* and *y* scan mirrors) and focused onto the sample by the objective lens. (**A**) Under descanned detection, the fluorescence emission follows a path returning back along the excitation beam path, first collected by the objective, passing by the scan mirrors, and reflected by a dichroic mirror and focused onto the confocal pinhole, to an 'internal' PMT detector. The pinhole is opened to the maximum. (**B**) Under non-descanned detection (NDD), the fluorescence emission is collected by the objective and reflected by a dichroic mirror through a transfer lens, which projects the light from the back aperture of the objective onto an 'internal' PMT. Under NDD, the position of the dichroic/lens/PMT varies by microscope model, but can be immediately behind the objective (reflected light detector). (**C**) Alternatively, fluorescence emission can be directly detected using an external detector before it reaches the objective (transmitted light detector) [24].

iv. Dichroic filters

The wavelength of emitted fluorescence is different form that one of the excitation light. Thus, the fluorescence emission can be resolved from the excitation light through a dichroic mirror. There are some important differences in the dichroic filters used to separate excitation light from fluorescence emission in two-photon microscopy compared to confocal microscopy. For a confocal microscope, a Long-Pass (LP) dichroic mirror is generally used since the fluorescence is at a longer wavelength. Contrariwise, a Short-Pass (SP) dichroic mirror should be used for two-photon microscopy due to the shorter wavelength of emitted fluorescence compared to the excitation light. Generally, an SP filter centered at <700 nm will be available, allowing the full range of excitation wavelengths available from a Ti:sapphire laser (700 nm to 1000 nm), which can excite most available fluorophores [24]. The main filter manufacturers now sell and design 'two-photon' versions on request after selecting the adequate characteristics of the optical filters (bandwidth, center frequency) [35].

- Advantages over confocal microscope

The localization of two-photon excitation to solely the focal plane, arising from the absorption dependence on the square of the excitation intensity, provides most of the advantages over confocal microscopy [24,32].

i. Deeper tissue imaging

Providing superior imaging deep into thick samples is one of the key advantages of two-photon microscopy. There are two mechanisms that allow this increased effectiveness in thick samples. The first mechanism is relayed to the light scattering, which is less detrimental in two-photon microscopy compared to confocal microscopy. Excitation light used in two-photon microscopy (infrared) will generally scatter less than the equivalent excitation light used in confocal microscopy (visible, bluegreen). Moreover, TPEF requires neither an aperture nor focused light at the detector, the emitted light does not have to pass

through the microscope at all. For example, a photodetector could be placed on the far side of the sample. Then, in the TPEF case, both the ballistic (straight line) and scattered photons are collected. Thus in this case less excitation/emission light is lost to scattering. The second mechanism is relayed to the absorbance, which is strongly confined at the focus, since no two-photon excitation occurs at the out-of-focus, no excitation light will be absorbed, such that more excitation light reaches the focus. These two mechanisms provide a high contrast with no bulk fluorescence which increased the signal to noise ratio in depth compared to one photon excitation.

- **Reduced photobleaching and phototoxicity**

Under two-photon excitation, photobleaching and phototoxicity will be restricted to the highly localized region in which fluorescence is excited. Two-photon excitation of fluorescence only occurs at the focal plane, such that the damage to cells caused by light interactions is much lower than for confocal microscopy where fluorescence and thus photodamage occurs throughout the sample. Thus, two-photon microscopy, for instance, is better suited to maintain viability and minimize perturbations to live thick tissue samples compared to confocal microscopy.

2.2.2.2 Second harmonic generation microscope

The nonlinear excitation used for TPEF offers the advantage, too, of being able to generate contrast from Second Harmonic Generation (SHG). Thus, SHG has a quadratic dependence on the laser light intensity like two-photon excitation. Therefore, SHG can be used for high-resolution imaging with instrumentation similar to that of two-photon-excited fluorescence microscopy, providing optical sectioning capabilities [18,21,36-39]. In contrast, SHG is a nonresonant process, which does not involve an excited state, conserving the energy and preserving the coherence of the laser light. SHG does not arise then from absorption, but from hyper Rayleigh scattering. Two photons of the same energy ‘‘coalesce’’ to a virtual state within the specimen to generate a photon of exactly twice the

energy of the incident photon. Figure 2.14 shows the Jablonski diagram for the energy transition of TPEF and SHG.

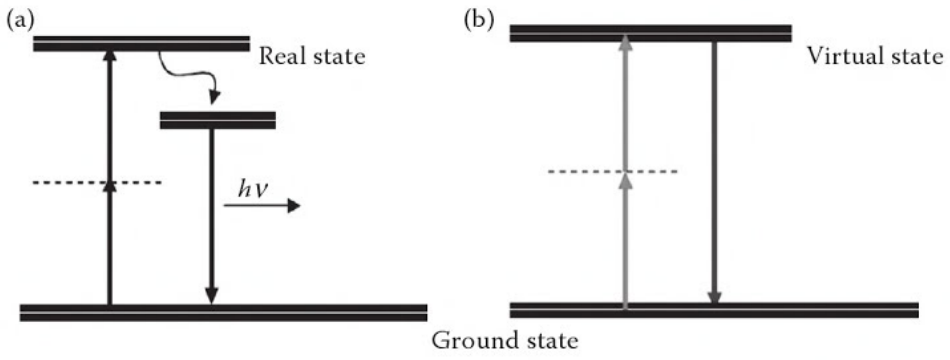

Figure 2.14: Energy level diagram for two-photon excitation fluorescence and second harmonic generation. (a) Depicts two-photon excited fluorescence. The dots lines represents the virtual state; (b) depicts SHG [18].

Due to the coherence of the SHG process, most of the signal propagates in the same direction as the incident laser beam contrarily to the fluorescence signal, which is emitted in all directions. This property raises the issue of directional detection but also makes SHG imaging microscopy unique in allowing one to probe molecular orientation and alignment. Second harmonic generation is a consequence of the nonlinear polarizability *P* of a material which is related to the electric field strength as follows:

$$P = \chi(1)E + \chi(2)E^2 + \chi(3)E^3 + \cdots$$

Where $\chi(1)$ represents the linear susceptibility of the medium independent of the field. The linear component gives rise to refraction, absorption, dispersion and birefringence of the medium. SHG arises from the second term describing the quadratic relation between the polarization and the electric field. The $\chi(2)$ is the second-order nonlinear susceptibility, which is a bulk material property related to the molecular hyperpolarizability. Thus, $\chi(2)$ is maximal for parallely aligned molecular dipoles and

zero for antiparallely oriented molecules. Therefore, the SHG requires a polarizable material with noncentrosymmetric symmetry such as collagen fibers and dipolar protein structures such as microtubule arrays [40,41]. SHG signals are generated owing to the intrinsic structures and do no need any additional labeling such dyes or fluorescence proteins. Because SHG does not arise from absorption, photobleaching and phototoxicity are greatly reduced which is an important advantage over the other optical sectioning microscopies techniques [42].

2.3 Förester resonance energy transfer

The FRET between two molecules is an important physical phenomenon with considerable interest for the understanding of some biological systems and with potential applications in optoelectronic and thin film device development [43,44].

FRET is a mechanism describing energy transfer from an excited donor molecule to an acceptor molecule. The energy is not emitted by the donor as a photon, or absorbed as a photon by the acceptor, but is transferred through non-radiative pathways [45]. This process is highly distance-dependent. The FRET occurs only when the acceptor and donor molecules are in nanometer proximity and have overlapping spectra [46]. Thus, this fluorescent technique is widely used as an effective molecular ruler to obtain structural and conformational dynamics changes informations about biological molecules within nanoscale [45, 47,48]. A small change in distance between two sites of a biological molecule, labeled with the appropriate donor-acceptor fluorochromes, can result in sizable change in the transferred energy [49]. Therefore, structural changes of biological molecules or relative motion between two different molecules can be detected via FRET variation.

2.3.1 Principle of FRET

The theoretical analysis was well developed by Theodor Förester [50]. In this non-radiative transfer mechanism, initially a donor group (D) absorbs the energy under an incident light

excitation with the appropriate wavelength, then relaxes to the lowest excited singlet state, S_1. This donor can then directly excite a nearby acceptor (A) by the released energy when the electron returns to the ground state (S_0). This non-radiative process is referred to as "resonance" [49,51]. After excitation, the excited acceptor emits a photon and returns to the ground state. Thus, activation of the acceptor can be detected by looking for the energy emitted at the new wavelength.

$$D + h\upsilon \rightarrow D^*$$
$$D^* + A \rightarrow D + A^* \text{ [D} \rightarrow \text{donor, A} \rightarrow \text{Acceptor]}$$
$$A^* \rightarrow A + h\upsilon'$$

The decrease or quenching of the donor fluorescence or the reduction of excited state lifetime accompanied also by an increase in acceptor fluorescence intensity are signs of energy transfer. The coupled transitions involved between the donor emission and acceptor absorbance in FRET is illustrated in the Jablonski diagram (Figure 2.15). In presence of a suitable acceptor, the donor fluorophore can transfer its excited state energy directly to the acceptor without emitting a photon.

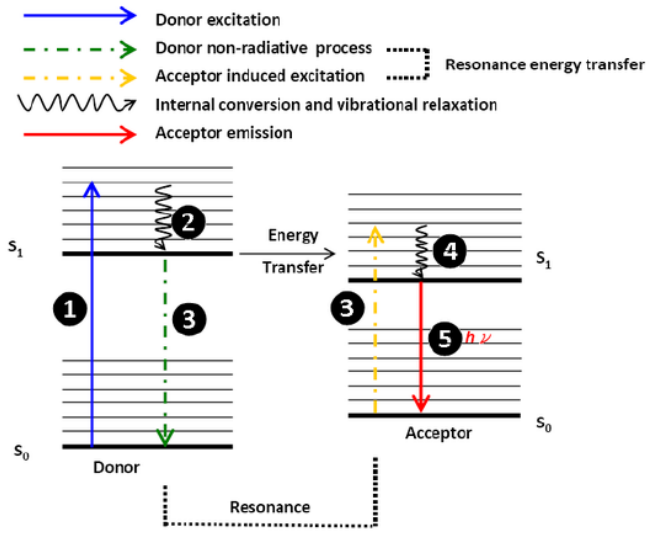

Figure 2.15: Schematic Diagram of Förster Resonance Energy Transfer [49]

Acceptance of donor energy by a FRET acceptor requires that two criteria must simultaneously be satisfied: compatibility and proximity [50,51].

2.3.2 Factors affecting FRET

- Förster distance

Proximity means that an acceptor molecule is "close enough" to the donor for the energy to excite it. The Förster theory shows that FRET efficiency (E_{FRET}) depends primarily on the distance between the donor and acceptor fluorophore and varies as the inverse sixth power of this distance (denoted by *r*):

$$E_{FRET} = \frac{1}{1+\left(\frac{r}{R_0}\right)^6}$$

Where R_0 is the characteristic distance between acceptor and donor, known as the Förster radius at which the FRET efficiency drops to 50 percent [52]. Because of the inverse sixth power dependence on the distance between the two molecules, for distances shorter than R_0, the FRET efficiency is close to maximal, whereas for distances greater than R_0, the efficiency rapidly approaches zero.

- Overlap of spectrum

An acceptor compatible molecule has an absorbance spectrum that overlaps with the emission spectrum of the donor molecule (Figure 2.16). Thereby, the energy lost from excited donor to the ground state could excite the acceptor molecule. This matching energy, which is associated with the coulombic interactions between electrons, is called the resonance phenomenon [49]. The more the quantum yield of the donor molecule and the absorption coefficient of the acceptor are high and the spectrum overlap degree is important, the better the donor can transfer the energy to the acceptor. The degree of overlap referred to as spectral overlap integral $J(\lambda)$, between the donor and the acceptor is given by the following formula:

$$J(\lambda) = \int F_D(\lambda) \times \varepsilon_A(\lambda) \times \lambda^4 d\lambda$$

Where $F_D(\lambda)$, is the normalized donor fluorescence and $\varepsilon_A(\lambda)$ is the acceptor excitation spectra

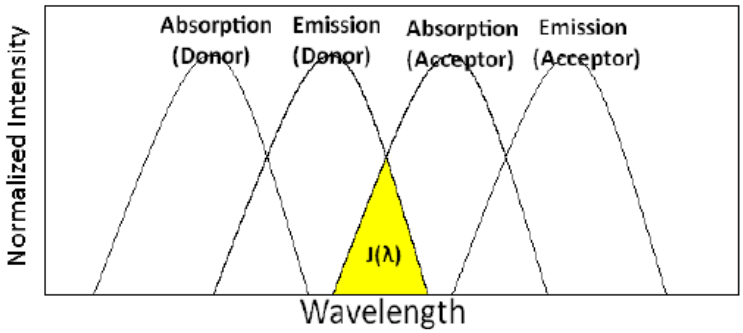

Figure 2.16 : schematic diagram of spectral overlap

- Orientation of transition dipoles

The resonance energy transfer mechanism is also affected by K^2, which represents the orientation factor between the emission transition dipole of the donor and the absorption dipole of the acceptor (Figure 2.17). In fact, the Förster radius R_0 depends on the relative orientation of transition dipoles and the degree of spectral overlap as denoted by the following formula [53]:

$$R_0 = [2.8 \times 10^{17} \times K^2 \times Q_D \times E_A \times J_\lambda]^{1/6}$$

where Q_D is the donor quantum yield, E_A is the maximal acceptor extinction coefficient in reciprocal moles per centimeter.

K^2 theoretically varies from 0 (when dipoles are perpendicular to each other) to 4 (when dipoles are collinear). Although, K^2 is usually assumed to be 2/3, which is the average value integrated over all possible angles for a freely rotational donor and acceptor group (Figure 17).

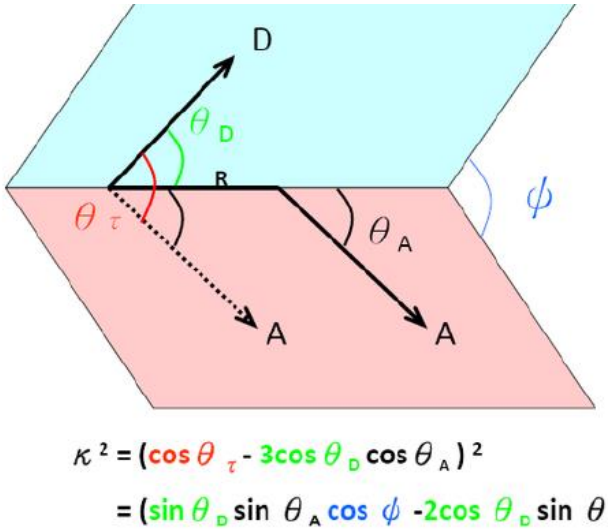

Figure 2.17: The schematic diagram of the directions of transition dipoles [49]

2.3.3 FRET between gold nanoparticles and dyes

FRET systems consisting of dye molecules and noble metal (plasmonic) nanoparticles have recently gained consideration in nanomaterials science, which is currently a very active field [54-57]. In fact, when the size of matter is reduced from bulk to the nanometer scale, materials proprieties including optical, magnetic, electronic, and structural proprieties behave very differently compared to larger scales [58,59]. These new proprieties make nano-sized particles (generally 1-100nm) very promising for a wide range of biological applications such as, for instance, cellular imaging, molecular diagnosis and targeted therapy, depending on the structure, composite and shape of the nanomaterials [60].

Plasmonic nanoparticles distinguish themselves from other nanoplatforms such as semiconductor quantum dots, magnetic and polymeric nanoparticle by their unique Surface Plasmon Resonance (SPR). This SPR, resulting from photon confinement to a small particle size, enhances all the radiative and nonradiative properties of the nanoparticles [61-63] and thus offering multiple modalities for biological and medical applications. For

biological applications, gold nanoparticles (GNPs) are of the best candidates due to their surface chemistry, photostability, water solubility and non toxicity proprieties [64-66].
In this section we throw some light on defining surface plasmons associated with GNPs as a first part before describing subsequently the mechanism of FRET between fluorescent dyes and these nanomaterials.

2.3.3.1 Surface plasmon resonance

A metal nanoparticle can be described as a dielectric with a positively charged core surrounded by negatively charged free electrons. When perturbed by an external electric force, the coulombic attraction between the electrons and positive ions induces a collective coherent oscillation of the electrons (plasmons) of the metal at their natural frequency, called plasma frequency. This electron oscillation around the particle surface causes a charge separation with respect to the ionic lattice, forming a dipole oscillation along the direction of the electric field of the light. The metal nanoparticle acts then like an oscillator, due to the movement of negative charges in the electric field, which causes polarisation on the surface. This phenomenon is represented in Figure 2.18.

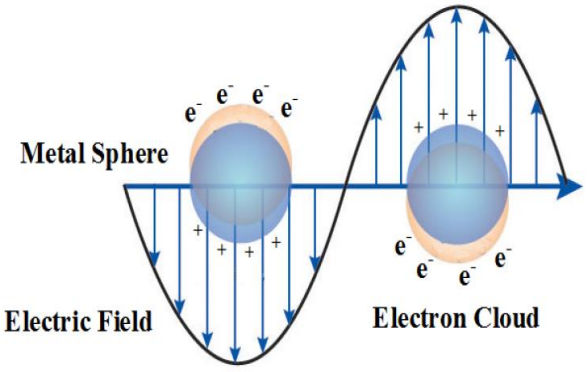

Figure 2.18 : Induced polarization of metal nanoparticle due to the interaction with electromagnetic radiation

The amplitude of the oscillation reaches maximum at a specific frequency, called Surface Plasmon Resonance (SPR) [67,68]. SPR occurs when the oscillating charged particle is in

resonance with the incident electromagnetic wave. The SPR induces a strong absorption of the incident light and thus can be measured using a UV–Vis absorption spectrometer. The SPR band is much stronger for plasmonic nanoparticles , as noble metals, especially Au and Ag, than other metals. Since the wave is on the boundary of the metal and the external medium (air or water for example), the SPR is very sensitive to any change in this boundary, such as the adsorption of molecules on to a metal surface. In fact, as theoretically described by Mie theory, the SPR band intensity and wavelength depends on factors affecting the electron charge density on the particle surface such as the metal type, particle size, shape, structure, composition and the dielectric constant of the surrounding medium [67].

Light of frequencies above plasma frequency is completely transmitted as electrons are not able to respond fast enough to the time-varying electric field. In most of the metals, the plasma frequency lies in the UV region, and that is the reason why most of the metals are quite shiny in the visible spectra. For noble-metal nanoparticles (gold, silver and copper), the plasmon peaks occur in the visible range of the spectrum, which is why they have gained paramount importance. The SPR of gold particles with a size of 40nm in water is at around 520nm, in the visible region [69]. The SPR band is affected by the particle size [70]. The SPR band of GNPs with size smaller than 10 nm is largely damped due to the phase changes resulting from the increased rate of electron-surface collisions compared to larger particles [71]. The SPR wavelength is red shifted with an enhancement of the intensity when the particle size increases. Moreover, due to the dominate contribution from higher order electron oscillation, the band broadening is obvious for a particle with a size larger than 100 nm.

2.3.3.2 Fluorescence manipulation by gold nanoparticles

The energy loss of electromagnetic wave (total light extinction) after passing through a material results from two contributions: absorption and scattering processes. The excitation of localized SPR in metal nanoparticles results in the nanoscale confinement of

electromagnetic fields near the metal surface and a significant enhancement in the local density of optical states. The absorbed and scatter lights by GNPs, are then strongly enhanced, 5–6 orders of magnitude stronger than most strongly absorbing organic dye molecules and than the emission of most strongly fluorescent molecules [72]. These properties have been widely employed to study the interactions between plasmons and fluorophores, which result in a change in the fluorescence emission level, i.e., quenching or enhancement. In fact, one can achieve a desired change in the fluorescence emission level, i.e., quenching or enhancement in the decay rate by appropriately selecting the GNP size and the excitation wavelength.

Establishing the relationship between the plasmon field and the resulting fluorescence level can be beneficial in developing highly efficacious optical contrast agents for bio-sensing/imaging. For example, conditional quenching of fluorescence may be effectively used for another form of sensing (i.e., negative sensing or selective quenching) [73]. Enhancement of fluorescence can offer a greater sensitivity and signal-to-noise ratio for molecular sensing/imaging [74,75], especially for the fluorophore with a low quantum yield.

- Fluorescence enhancement

The fluorescence enhancement is due to a FRET from GNPs to dyes. The fluorescence enhancement rate (ϕ) is the combined effect of the normalized enhancement of the excitation decay rate $\frac{\gamma_{exc}}{\gamma_{exc}^{0}}$ and the change in the quantum yield (q) as shown in the following equation [76]:

$$\phi = \frac{\gamma_{exc}}{\gamma_{exc}^{0}} \frac{q}{q^{0}}$$

where the superscript $^{(0)}$ is for the value of the system without GNP.

The enhancement of the excitation decay rate and the change in the quantum yield are both influenced by the plasmon field. SPR causes an increase in the intensity of the

electromagnetic field in the vicinity of the metal nanoparticle, but this increased intensity decreases rapidly with distance, and becomes insignificant within a few nanometers of the nanoparticle [77]. The intensity on the surface can be two orders of magnitude greater than the initial intensity, depending on the shape of the particle. For that, the suitable dye to obtain a fluorescence enhancement should have an excitation spectrum that overlaps with the SPR band of GNPs. The intense plasmon field, generated around the particle by the incident light with a wavelength within both of the dye excitation spectrum and the SPR of GNPs, increases the normalized enhancement of the excitation decay of the fluorophore $(\frac{\gamma_{exc}}{\gamma_{exc}^0})$,which in turn enhances the level of fluorescence emission (ϕ). The normalized enhancement of the excitation decay has the relationship with the normalized plasmon field strength $\frac{E_p}{E_0}$ as in the following equation

$$\frac{\gamma_{exc}}{\gamma_{exc}^0} = \left(\frac{E_p}{E_0}\right)^2$$

Moreover, fluorescent dyes with a low quantum efficiency receive the greatest enhancement, whereas dyes with a high quantum efficiency (q^0) are not considerably improved. The enhancement factor is greatest for small particles of approximately 10nm and decreases with increasing size. The enhancement rate (ϕ) is also dependent upon distance from the nanoparticle as the electromagnetic field intensity decreases rapidly with increasing distance. The increase is at a maximum when the absorption peak wavelength of the fluorescent dye coincides with the resonance wavelength of the particle.

- **Fluorescence quenching**

The fluorescence quenching takes place for dyes which are in close proximity to GNPs and have an emission spectrum that overlaps with the SPR [76]. The high light absorption by GNPs reduces the ratio of the radiative to non-radiative decay rate and the quantum yield (q) of the fluorophore that can be described as

$$\frac{q}{q^0} = \frac{\frac{\gamma_r}{\gamma_{r0}}}{\frac{\gamma_r}{\gamma_{r0}} + \frac{\gamma_{abs}}{\gamma_r} + \left(\frac{1-q_0}{q_0}\right)}$$

where γ_r is the radiative decay rate, γ_{abs} is the additional non-radiative decay rate resulted from the radiated energy absorbed by the particle, and q^0 is the intrinsic quantum yield of the fluorophore.

GNPs absorb light the strongest at around the plasma resonance peak. However, if the fluorophore has an emission peak close to the plasma resonance peak, q will be decreased significantly due to the large second term value in the denominator of the previous equation, resulting in the fluorescence quenching.

The quenching/enhancement effects depend on factors such as the identity of the metal, the distance of the fluorophore from the NP and the orientation of its transition dipole relative to the GNP surface. In particular, quenching is thought to be favored for particle-dye distances shorter than 6 nm, the dipole energy around the nanoparticle reduces the ratio of the radiative to non-radiative decay rate and the quantum yield of the fluorophore, resulting in the fluorescence quenching, whereas, enhancement has been reported primarily for distances between ~6-10 nm [78,79].

2.4 Conclusion

This chapter explains methods to improve biological imaging. The first section discussed the basic theory and concepts of optical sectioning microscopies. Two modalities of optical sectioning microscopy have been described. Where the confocal microscopy has been introduced firstly as an example of linear microscopy. Then, an overview of TPEF and SHG as two examples of non-linear microscopy was provided due to the fact that the combination of these two techniques has been employed in the experiments described in Chapter 3. In the second part of this chapter, the concept of FRET was discussed. The plasmonic enhancement/quenching of fluorescent dyes in proximity to gold nanoparticles

was then outlined. The combination of confocal microscopy and FRET as a technique to increase the performance in biological imaging, is the focus of the work in the chapters 4 and 5.

References

[1] J. A. Conchello and J. W. Litchaman. Optical sectioning microscopies. *Nature methods*. 2015, 2 (12): 920-931

[2] T. Wilson and A. R. Carlini. Three-Dimensional Imaging in Confocal Imaging Systems with Finite Sized Detectors, *Journal of Microscopy*. 1988, 149: 51-66.

[3] D. B. Murphy. Fundamentals of Light Microscopy and Electronic Imaging. *New York: Wiley-Liss*. 2001.

[4] S. J. Wright and D. J. Wright. Introduction to Confocal Microscopy, in B. Matsumoto (ed.), *Cell Biological Applications of Confocal Microscopy*. *In Methods in Cell Biology, New York:Academic Press*. 2002,70:1-85, 2002.

[5] T. Wilson. Optical Sectioning in Confocal Fluorescence Microscopes. *Journal of Microscopy.* 1989. 154: 143-156.

[6] R. H. Webb, Confocal Optical Microscopy, *Rep. Prog. Phys.* 1996,59:427-471.

[7] J. W. Lichtmann, Confocal Microscopy, *Scientific American*, 40-45, August, 1994.

[8] J. G. White, W. B. Amos, and M. Fordham. An Evaluation of Confocal versus Conventional Imaging of Biological Structures by Fluorescence Light Microscopy, *J. Cell Biol.* 1987, 105: 41-48.

[9] J. R. Swedlow, K. Hu, P. D. Andrews, D. S. Roos, and J. M. Murray. Measuring Tubulin Content in *Toxoplasma gondii*: A Comparison of Laser-Scanning Confocal and Wide-Field Fluorescence Microscopy. *Proc. Natl. Acad. Sci. USA.* 2002 99: 2014-2019.

[10] K. R. Spring and S. Inoué. Video Microscopy: The Fundamentals. *New York: Plenum Press*. 1997.

[11] J. J. Stamnes. Waves in focal regions. *Bristol: IOP Publishing Ltd*. 1986.

[12] M. Muller. Introduction to confocal fluorescence microscopy. *Tutorial Texts in Optical Engineering*, V.69. 2006.

[13] J. E. N. Jonkman and E. H. K. Stelzer, Resolution and Contrast in Confocal and Two-Photon Microscopy, in A. Diaspro (ed.), *Confocal and Two-Photon Microscopy: Foundations, Applications, and Advances*, New York: Wiley-Liss, 2002. 101-125.

[14] E. H. K. Stelzer. Practical Limits to Resolution in Fluorescence Light Microscopy, in R. Yuste, F. Lanni, A. Konnerth (eds.), *Imaging Neurons: A Laboratory Manual*, New York: Cold Spring Harbor Press, 12.1-12.9, 2000

[15] E. H. K. Stelzer. Contrast, Resolution, Pixelation, Dynamic range, and Signal-to-Noise Ratio: Fundamental Limits to Resolution in Fluorescence Light Microscopy. *Journal of Microscopy*. 1997, 189: 15-24.

[16] J. Pawley, Fundamental Limits in Confocal Microscopy, in J. B. Pawley (ed.), *Handbook of Biological Confocal Microscopy*, New York: Plenum Press. 1995. 19-37.

[17] J. Murray. Confocal Microscopy, Deconvolution, and Structured Illumination Methods, in R. D. Goldman and D. L. Spector (eds.), *Live Cell Imaging: A Laboratory Manual*, New York: Cold Spring Harbor Press. 2005. 239-280.

[18] H. Hanry, N. A. Abdul Rahim. Imaging in tissue and cellular engineering. *Taylor and Francis group LLC*. 2013.

[19] R.P. Haugland. Fluorescence tutorials. Invitrogene Molecular Probes. 2005.

[20] J.R. Lakowicz. Principles of Fluorescence Spectroscopy. Plenum Press, New York. 1999

[21] M. Oheim, D. J. Michael, M. Geisbauer, D. Madsen, R. H. Chow. Principles of two-photon excitation fluorescence microscopy and other nonlinear imaging approaches. *Advanced Drug Delivery Reviews*. 2006, 58 : 788–808.

[22] K. W. Dunn and P. A. Young, Principles of multiphoton microscopy. *Nephron Exp. Nephrol. 2006.* 103 :e33-40

[23] D. W. Piston. Imaging living cells and tissues by two-photon excitation microscopy.

Trends in Cell Biology. 1999, 9, 66-69 (1999)

[24] Richard K.P. Benninger1 and David W. Piston. Two-Photon Excitation Microscopy for the Study of Living Cells and Tissues. *Curr Protoc Cell Biol*. 2013.

[25] K. Svoboda and S. M. Bloch. Biological applications of optical forces. *Annu. Rev. Bioph. Biomol. Struc*. 1994, 23: 247-285.

[26] Goppert-Mayer M. Uber Elementarakte mit zwei Quantensprungen. *Ann Physik*. 1931, 9:273–294

[27] Kaiser W, Garrett CGB. Two-photon excitation *in CaF2:Eu2+ Phys Rev Lett*. 1961, 7:229–231

[28] W. Denk, D. W. Piston, W. W. Webb. Two-photon excitation in laser scanning microscopy. In: Pawley, J., editor. Handbook of Biological Confocal Microscopy. *Plenum; New York*: 1995. p. 445-458.

[29] P. TC So. Two-photon fluorescence light microscopy. *Encyclopedia Of Life Sciences. Macmillan Publishers Ltd, Nature Publishing Group*. 2002

[30] W. Denk W, J. H. Strickler, W. W. Webb. Two-Photon laser scanning fluorescence microscopy. *Science*. 1990, 248:73–76.

[31] M. Rubart. Two-photon microscopy of cells and tissues. *Circ Res*. 2004, 95:1154-1166.

[32] C. Soeller. M. B. Cannell. Two-photon microscopy: imaging in scattering samples and three-dimensionally resolved flash photolysis. *Microsc Res Tech*. 1999, 47:182–195.

[33] G. Brown, H. Hempstead. The Benefits of Non-Descanned (External) Detectors in Multi-Photon Microscopy. *Microscopy division. Bio-rad.*

[34] W. Denk. J. P. Stickler, W. W. Webb. Two-photon molecular excitation in laser scanning microscopy. Handbook of Biological Confocal Microscopy. Ed. J. B. Pawley, *Plenum Press, New York*. 1995

[35] Chroma (http://www.chroma.com/) and Semrock (http://www.semrock.com/)

[36] P. J. Campagnola, A. C. Millard, M. Terasaki, P. E. Hoppe, C. J. Malone, and W. A. Mohler. Three-dimensional high-resolution second-harmonic generation imaging of

endogenous structural proteins in biological tissues. *Biophys. J*. 2002. 81:493–508.

[37] R. M. Williams, W. R. Zipfel, and W. W. Webb. Interpreting second-harmonic generation images of collagen I fibrils. *Biophys. J*. 2005, 88: 1377–1386.

[38] A. Zoumi, A. Yeh, and B. J. Tromberg. Imaging cells and extracellular matrix in vivo by using second-harmonic generation and twophoton excited fluorescence. *Proc.Natl. Acad. Sci.USA.* 2002, 99:11014–11019

[39] W. R. Zipfel, R. M. Williams, R. Christie, A. Yu Nikitin, B. T. Hyman, and W. W. Webb. Live tissue intrinsic emission microscopy using multiphoton-excited native fluorescence and second harmonic generation. *Proc. Natl. Acad. Sci. USA*. 2003, 100:7075–7080.

[40] G. Cox, E. Kable, A. Jones, I. Fraser, F. Manconi, and M. D. Gorrell. 3-dimensional imaging of collagen using second harmonic generation. *J. Struct. Biol*. 2003, 141:53–62.

[41] T. Theodossiou, G. S. Rapti, V. Hovhannisyan, E. Georgiou, K. Politopoulos, and D. Yova. Thermally induced irreversible conformational changes in collagen probed by optical second harmonic generation and laser-induced fluorescence. *Lasers Med. Sci.* 2002, 17:34–41.

[42] C. Ricard, B. Vacca, P. Weber. Three-dimensional imaging of small intestine morphology using non-linear optical microscopy and endogenous signals. *J. Anat*. 2012, 221: 279–283

[43] V. G. Kozlov, V. Bulovic, P. E. Burrows, S. R. Forrest. Laser action in organic semiconductor waveguide and
double-heterostructure devices. *Nature.* 1997, 389:362.

[44] C. R. Cantor, P. R. Schimmel. *Biophysical Chemistry* Part-II, Freeman, San Francisco, 1980

[45] K. E. Sapsford, L. Berti, and I. L. Medintz, .Materials for fluorescence resonance energy transfer analysis: beyond traditional donor-acceptor combinations. Angew. *Chem. Int. Ed. Engl*. 2006, 45(28) :4562–4589.

[46] C. S. Yun, A. Javier, T. Jennings, M. Fisher, S. Hira, S. Peterson, B. Hopkins, N. O.

Reich, and G. F. Strouse. Nanometal surface energy transfer in optical rulers, breaking the FRET barrier. *J. Am. Chem. Soc*. 2005, 127(9): 3115–3119.

[47] C. A. Royer. Probing protein folding and conformational transitions with fluorescence. *Chem. Rev*. 2006, 106(5): 1769–1784.

[48] J. R. Lakowicz, .Principles of Fluorescence Spectroscopy.*3rd ed. Plenum*. 2006.

[49] UC Davis ChemWiki.https://netfiles.uiuc.edu/tjha/www/newTechnique.html

[50] T. Forster. Intermolecular energy transfer and fluorescence. *Ann. Physics*. 1948 2:55-75.

[51] J. R. Lakowicz. Principles of fluorescence spectroscopy. *Kluwer Academic/ Plenum Publishers, New York*. 1999.

[52] T. Förster. Transfer mechanisms of electronic excitation. *Discuss Farady Soc*. 1959, 27 (7)

[53] E. Haas, M. Wilchek, E. Katchalski-Katzir, and I. Z. Steinberg. Distribution of end-to-end distances of oligopeptides in solution as estimated by energy transfer. *Proc. Natl. Acad. Sci*. USA. 1975, 72 :1807

[54] T. H. Taminiau, F. D. Stefani, F. B. Segerink, N. F. van Hulst. Optical antennas direct single-molecule emission. *Nat. Photonics*. 2008, 2 : 234−237.

[55] A. Grubisic, V. Schweikhard, T. A. Baker, D.J. Nesbitt. Coherent multiphoton photoelectron emission from single Au nanorods: The critical role of plasmonic electric near-field enhancement. *ACS Nano*. 2013, 7: 87−99.

[56] L. Zhao, T. Ming, H.J. Chen, Y. Liang, J.F. Wang. Plasmoninduced modulation of the emission spectra of the fluorescent molecules near gold nanorods. *Nanoscale*. 2011, 3: 3849−3859.

[57] N. Narband, M. Uppal, C.W. Dunnill, G. Hyett, M. Wilson, I.P. Parkin. The interaction between gold nanoparticles and cationic and anionic dyes: enhanced UV-visible absorption. *Phys. Chem. Chem.Phys*. 2009, 11: 10513−10518.

[58] M.A. El-Sayed. Small is different: Shape-, size- and composition-dependent properties of some colloidal semiconductor nanocrystals. *Acc Chem Res*. 2004,37(5):326–33.

[59] M.A. El-Sayed. Some interesting properties of metals confined in time and nanometer space of different shapes. *Acc Chem Res*. 2001, 34(4):257–64.

[60] S. Nie, Y. Xing, G.J. Kim, J.W.Simons. Nanotechnology applications in cancer. *Annu Rev Biomed Eng*. 2007,9:257–88.

[61] D. Link S, M.A. El-Sayed. Spectral properties and relaxation dynamics of surface plasmon electronic oscillations in gold and silver nanodots and nanorods. *J Phys Chem B*. 1999, 103(40):8410–26.

[62] S. Link S, M.A. El-Sayed. Shape and size dependence of radiative, non-radiative and photothermal properties of gold nanocrystals. *Int Rev Phys Chem*, 2000, 19(3):409–53.

[63] S. Link, M.A.El-Sayed. Optical properties and ultrafast dynamics of metallic nanocrystals. *Annu Rev Phys Chem*. 2003, 54:331–66.

[64] S. Kumar, N. Harrison, R. Richards-Kortum, and K. Sokolov. Plasmonic Nanosensors for Imaging Intracellular Biomarkers in Live Cells. *Nano Lett*. 2007, 7(5): 1338-1343.

[65] B. D. Chithrani, A. A. Ghazani, W.C. W. Chan. Determining the size and shape dependence of gold nanoparticle uptake into Mammalian cells. *Nano Lett.* 2006, 6, 662-668.

[66] P. Yang, X. Sun, J. Chiu, H. Sun, Q. He. Transferrin-mediated gold nanoparticle cellular uptake. *Bioconjugate Chem*. 2005, 16: 494-496.

[67] G. Mie. A contribution to the optics of turbid media, especially colloidal metallic suspensions. *Ann Phys*. 1908,25:377–445.

[68] U. Kreibig, M. Vollmer. Optical properties of metal clusters. *Springer*. 1995.

[69] X. Huang, M. A. El-Sayed .Gold nanoparticles: Optical properties and implementations in cancer diagnosis and photothermal therapy. *Journal of Advanced Research* . 2010, 1: 13–28.

[70] S. Link, M. A. El-Sayed. Size and temperature dependence of the plasmon absorption of colloidal gold nanoparticles. *J Phys Chem B*. 1999,103(21):4212–7.

[71] U. Kreibig, C. von Fragsetein. The limitation of electron mean free path in small

silver particles. *Z Phys.* 1969, 224:307–23.

[72] P. K. Jain, K. S. Lee, I. H. El-Sayed, M. A. El-Sayed. Calculated absorption and scattering properties of gold nanoparticles of different size, shape, and composition: applications in biological imaging and biomedicine. *J Phys Chem B*. 2006, 110(14):7238–48.

[73] B. Hong, K. A. Kang. Biocompatible, nanogold-particle fluorescence enhancer for fluorophore mediated. *optical immunosensor. Biosensors and Bioelectronics*. 2006, 21:1333-1338.

[74] N. MY, L.WC. Fluorescence enhancements of fiber-optic biosensor with metallic nanoparticles. *Opt Express. 2009*, 17:5867-5878.

[75] K. A. Kang, B. Hong . Biocompatible nano-metal particle fluorescence enhancers. *Critical Reviews in Eukaryotic Gene Expression* 2006, 16:45-60.

[76] A.K. Kang, J. Wang, J. B. Jasinski and S. Achilefu.Fluorescence Manipulation by Gold

Nanoparticles: From Complete Quenching to Extensive Enhancement. *Journal of Nanobiotechnology*. 2011, 9:16.

[77] D. D. Evano, R. L. White, and G. Chumanov. Measuring the distance dependence of the local electromagnetic field from silver nanoparticles. *Journal of physical Chemistry B*. 2004,108:1522-1524.

[78] T. Huang and R. W. Murray. Quenching of [Ru(bpy)3]2+ fluorescence by binding to Au nanoparticles. *Langmuir*. 2002, 18:7077-7081.

[79] R.R. Chance, A. Prock, and R. Silbey. Molecular uorescence and energy transfer near interfaces. *Adv. Chem. Phys*. 1978, 60:1-65.

Chapter 3

Three dimensional visualization of human corneal tissue

3.1 Introduction

When performing a live-cell imaging experiment or observation, several challenges must be considered to maintain cells alive as long as possible [1-5]. For example, contrarily to fixed cells, the classic procedure of labeling the sample, as the histology technique, induces a perturbation of the cells structures in live biological specimen [6-9]. Challenges related to this procedure are even more complicated mainly when the tissue has an important thickness. In fact, with increasing depth, it becomes increasingly difficult to introduce fluorescent labels into the cells and tissue of interest. With advances in optical imaging technology, the limitations imposed by the viability and the thickness of the sample are now being overcome [10-13]. In fact, these imaging technologies, offer greater sample penetration and avoid photobleaching of marker dyes which increase the viability of the cell.

The human cornea is served in this work as an example to illustrate that the combination of SHG and TPEF microscopies is a suitable tool for visualizing, close to *in vivo* conditions, morphologic features of a biological sample with an important thickness.

.

Various observable components within the ocular surface are of structural and functional significance [14,15]. Morphologically, it is known that the cornea is covered with epithelium followed by stroma, which is composed mainly of collagen fibers with an interwoven lamellar arrangement and responsible for the transparency, the mechanical stability and convex shape of the cornea [16,17]. Diseases affecting cornea are associated to the deviations of the orientation of collagen fibrils[18-20]. Although histologic procedures are available to monitor changes to the cornea, the transparent nature of the cornea prevents its internal structures to be analyzed easily [21].

Therefore the ability to acquire structural information and specially resolving the collagen from corneal connective tissue without histologic procedures is of key significance in the physiological studies and disease diagnosis of the eye [22,23]. Moreover, the change of autofluoroscence in diabetic patients and diseases such as corneal and conjunctival tumors are potential imaging targets of multiphoton microscopy[24-26]. Thus, in this work, the features of interest are the collagen and connective tissues.

The two nonlinear microscopy techniques used in this work are the second harmonic generation and the two photon excitation fluorescence microscopies. Connective tissues have some intrinsic level of autofluorescence, which is commonly caused by NADH, riboflavins, and flavin coenzymes. This autofluorescence can be generated under an excitation with a wavelength in the 250-500 nm range (Fig. 3.1)[27]. Thus, these tissues are able to absorb simultaneously, two photons with the same wavelength in the 500-1000nm range. On the other hand, the noncentrosymmetric molecules within the cornea (collagen), generate a second harmonic signal under an excitation with a wavelength between 790 and 860 nm[28]. Thus, the two signals SHG and TPEF emitted respectively from collagen and connective tissues strongly overlap.

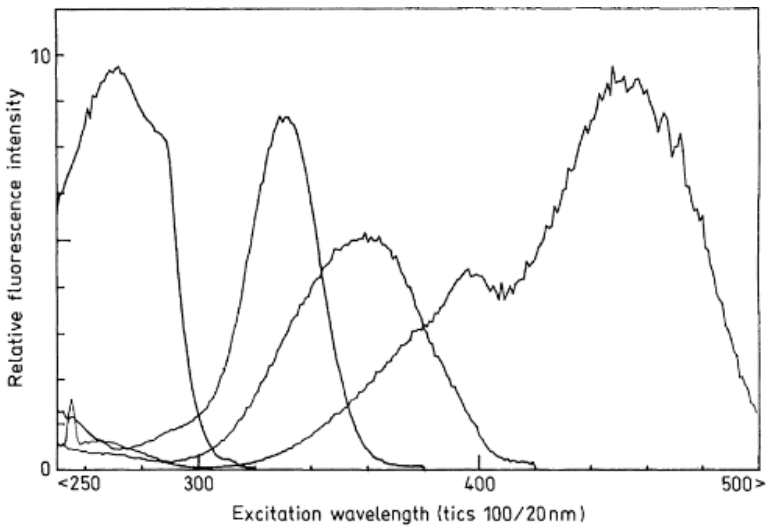

Figure 3.1: Excitation spectra of the four major cellular fluorophores- excitation wavelength vs relative fluorescence intensity. The spectra from left to right corresponds to the fluorophores of, tryptophan, pytidoxine, NADH, and riboflavin respectively [27]

In this work, based on a combination of the SHG and TPEF microscopies, we will show that the introducing of the adequate filters and dichroic mirrors within the channel detection allows a separation of the collagen signal from connective tissues autofluorescence to acquire corneal morphologic features on two important layers: the epithelium and stroma.

3.2 Materials and methods

3.2.1 Acquisition and processing of human cornea

3.2.1.1 Corneal tissues

Eye bank–donor corneoscleral tissues from different donors that are not suitable for transplantation were obtained from the Veneto Eye Bank Foundation (Venezia Zelarino, Italy). The tissues were explanted between 3 and 22 hours after death (mean, 12 ± 5 hours) and cultivated at 30°C in corneal storage medium [28,29]. Donors did not have a history of corneal pathologies or eye surgery. Inclusion criteria included an endothelial cell

density of 1700 cells/mm^2 or greater. All human tissues were used in compliance with the guidelines of the Declaration of Helsinki for research involving the use of human tissue, and the experimental protocol was approved by the National Research Council (CNR) research ethics and bioethics advisory committee. Each corneoscleral tissue was kept in 20% dextran-enriched storage solution at room temperature for 30 minutes before commencing each session of experiments.

3.2.1.2 Corneal support

For the realization of the corneal support it was necessary to take into account the diameter of the corneal curvature (8mm) and the focal length of the objective lens. The cornea is placed in a holder sample equipped by an anterior room (Fig. 3.2). A drop of dextran between the cornea and the glass door of the sample is necessary to avoid dehydration during the experiment. It is also essential to eliminate any air bubbles trapped beneath the corneal tissue, which can produce side effects of scattering or aberrations. Another drop of dextran stabilized via a silicone ring was necessary as a liquid bridge between the objective and the corneal surface.

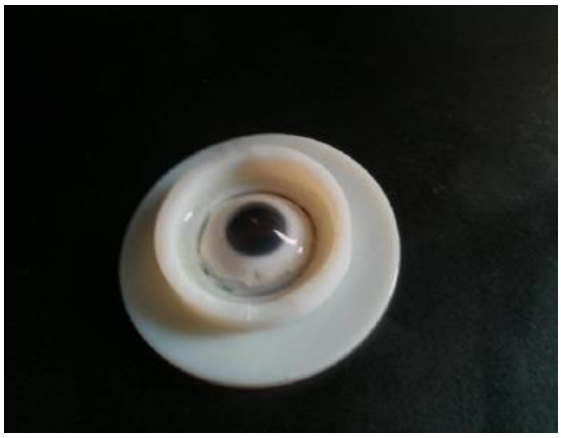

Figure 3.2*:* a holder sample for human cornea equipped by an anterior room

3.2.2. Non-linear instrumentation

3.2.2.1 Laser

Experimental characterizations are realized through the non-linear two-photon microscope of the Leica system (Leica DM6000CS; Leica Microsystems GmbH, Wetzlar, Germany). In particular, The non-linear microscope is equipped with Ti:sapphire IR laser source (VISION II; Coherent Inc., Santa Clara, CA, USA). This laser presents a tunable wavelength range from 680 nm to 1080 nm pulsed at high frequency (a pulse width of 140 fs at 80-MHz repetition rate). The excitation pump beam with the 810 nm wavelength is focused into a spot within the sample by the scan head (Leica SP8-Spectral Scan-Head; Leica Microsystems GmbH) allowing the Z-movement of the microscope water-immersion objective 25X (HCX IRAPO L 25x / 0.95 W) which has a working distance of 2.5 mm (figure2). The spot is rastered across the lateral plan with the x-y scanning module.

Figure 3.3 : the water immersion objective in contact with the surface of the cornea

3.2.2.2 Dichroic filters and detectors

Three non descanned detectors are used in this experiment. Two detectors (NDD1) and (NDD2) placed in the reflection path of the microscope collecting respectively in a backward direction the SHG signal from collagen in the corneal stroma and TPEF signal from autofluorescent molecules. A third detector (NDD) in the transmission path collecting the SHG in a forward direction. To ensure a high efficiency in preventing stray light from reaching detectors, reflected and transmitted light are filtered with the suitable filters and dichroic beam splitter mirror assembled into a cubic block Dichroic filters (Semrock, Inc.) (Figure 3.4). The excitation filter, barrier filter and dichroic mirror need to be matched to the excitation and emission characteristics of components of interest (collagen and autofluorescent molecules) to ensure a high signal to noise ratio between the positive signal and the background light. The ideal combination of barrier filters and excitation filters is one that lets no undesired light pass when combined. For the transmission NDD unit, In order to image only the SHG forward signal emitted by the corneal stroma and to avoid a contamination from the autofluorescence and the excitation beam, the incoming light first goes through a short pass filter (SP680; Leica Microsystems GmbH) ($\lambda < 680$ nm) and then is filtered by a 10-nm full width at half-maximum band-pass filter centered at 405 nm (FF01-405/10-25; Semrock, Inc.). For the reflection, NDD1 and NDD2 unit detected light is filtered through the cubic filter, which assembles an infrared filter (SP680; Leica Microsystems GmbH) to reject the excitation wavelength, a dichroic mirror to split respectively the incoming light beam into a two beams, a transmitted beam and a reflected beam at an angle of 90°, and a 10-nm full width at half-maximum band-pass filter centered at 405 nm (FF01-405/10-25; Semrock, Inc.), which separates the SHG signal from the TPEF signal. A schematic of the optical setup is summarized in Figure 3.5.

The filter transmission spectra used to isolate the SHG signal from the TPFE signal in the backward direction (A) and the forward direction (B) are presented in Figure 3.6.

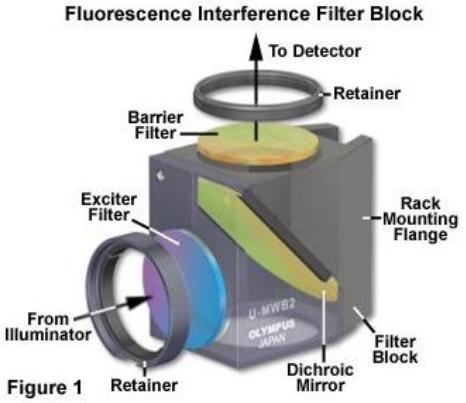

Figure 3.4: Cubic block dichroic filter : where dichroic beam splitter mirror and excitation filter are assembled

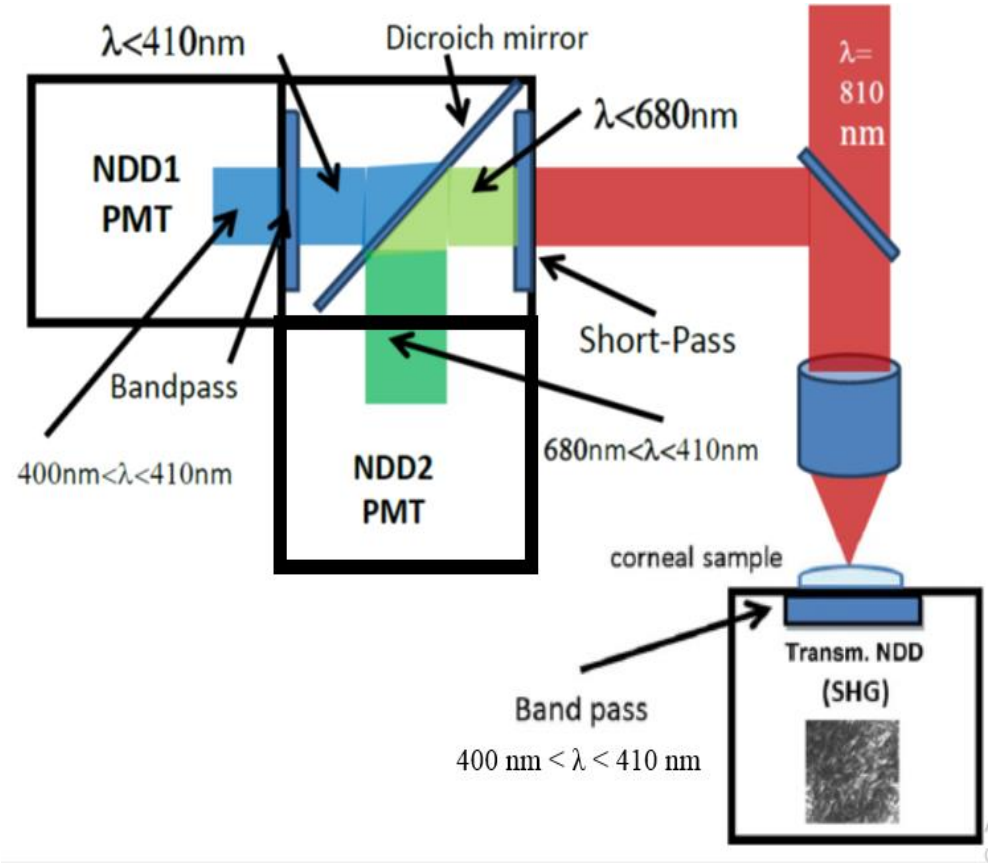

Figure 3.5 : Optical setup of the non linear microscopy used in the present study. Near-infrared femtosecond-pulsed excitation with a wavelength of 810 nm provides both morphological and structural information within the corneal stroma. By using two detection channels in the forward and backward directions, the SHG signal from collagen and TPEF from autofluorescent molecules are respectively detected.

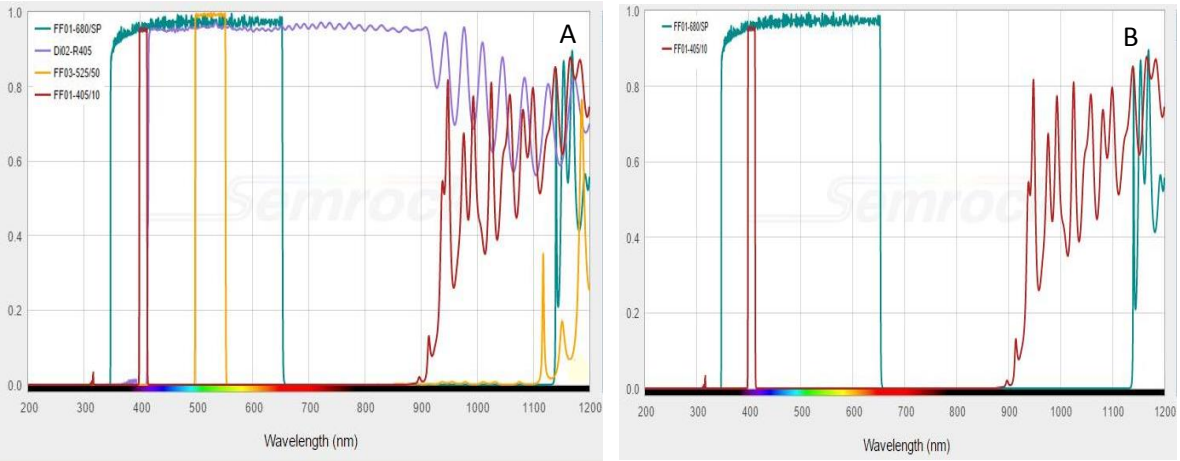

Figure 3.6: Filter transmission spectra used to isolate the SHG signal from the TPFE signal in the forward direction (A) and the backward direction (B)

3.3 Results and discussion

3.3.1 Autofluorescent cells

The figure 3.7 shows a two photon three dimensional scan of the cornea at the depth indicated in the figure legend. Images were acquired within a lateral cross section from the epithelium (Figure 3.7A) and a vertical cross section with increasing depth within the cornea based on the z-stacks of lateral cross sections from the epithelial layer and the stroma (Figure 3.7B). Under an excitation with a wavelength of 810 nm, the cytoplasm within the epithelial layer and the NADPH components absorbs simultaneously two photons at the wavelength of 405 nm and emit light in the range of 410-680 nm. These cells are then distinguished due to their endogenous proprieties. The maximum intensities of the autofluorescent molecules emission occur at 450 nm. Therefore, the detection bandwidth of emitted light is set to be beyond the SHG signal band and to contain the maximum of autofluorescent molecules emission. The brightness of the detected autofluorescence emission shows a large difference between the two cell layers, the epithelial layer and the stroma, as revealed in the image of the vertical cross sectioning (Figure 3.7B). The brighter signal was detected from the basal epithelial cells. The lowest

fluorescent intensity was detected from the stroma. These results support the fact that the cells in the basal region are the most metabolically active [15].

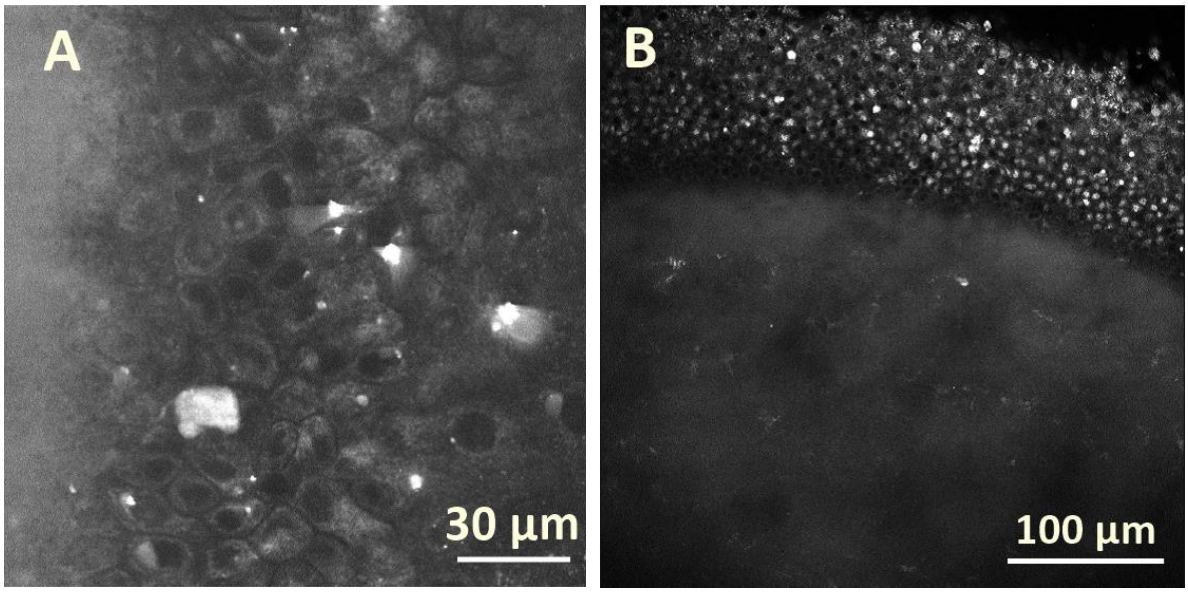

Figure 3.7: Three dimensional TPEF imaging: A) A lateral cross sectioning image through endothelial cells recorded at an axial depth of 50 µm into the corneal endothelium. B) A vertical cross sectioning visualization of corneal endothelium and stroma based on the z stacks of 800 lateral sections recorded at an axial step of 0.57 µm into a deepness of 456 µm within the sample. The excitation power is approximately 15 mW at the wavelength of 810 nm. The nonlinear signal of the autofluorescence from corneal tissue is detected in the backward direction with the NDD2 in the range of 410-680 nm.

3.3.2 Collagen

SHG vertical cross section imaging are reported in the figures 3.8 and 3.9 . Images are acquired under the wavelength of 810nm and detected with the non descanned detectors NDD and NDD1 placed respectively in the forward and the backward directions. The SHG signal is detected in the 400-410 nm range to avoid a maximum of contamination from autofluorescent molecules. The SHG is detected only in stroma due to the highly organization of stromal collagen in stroma. Collagen are embedded in an optically homogeneous ground substance, the stromal matrix, consisting of glycosaminoglycans and proteoglycans [2]; in addition, they show a highly heterogeneous distribution over the

stromal depth. As shown in the SHG images of lateral sections (Figures 3.8B), the collagen distribution varies with deepness throughout stroma. This fibril bundles in the most anterior stroma show pseudo-random spatial distribution (Figure3.8, B1 and B2), across the posterior stroma (Figure 3.8 B3), they are arranged in lamellae that run almost parallel to the corneal surface, forming a grid-like lamellar structure with more ordered organization if compared to the anterior [29,30]. Moreover, the SHG signal from collagen in the forward direction is much more brighter compared to the signal detected in the backward direction. This strong difference between the intensity of the two signals can be attributed to the shorter optical pathway in the forward direction.

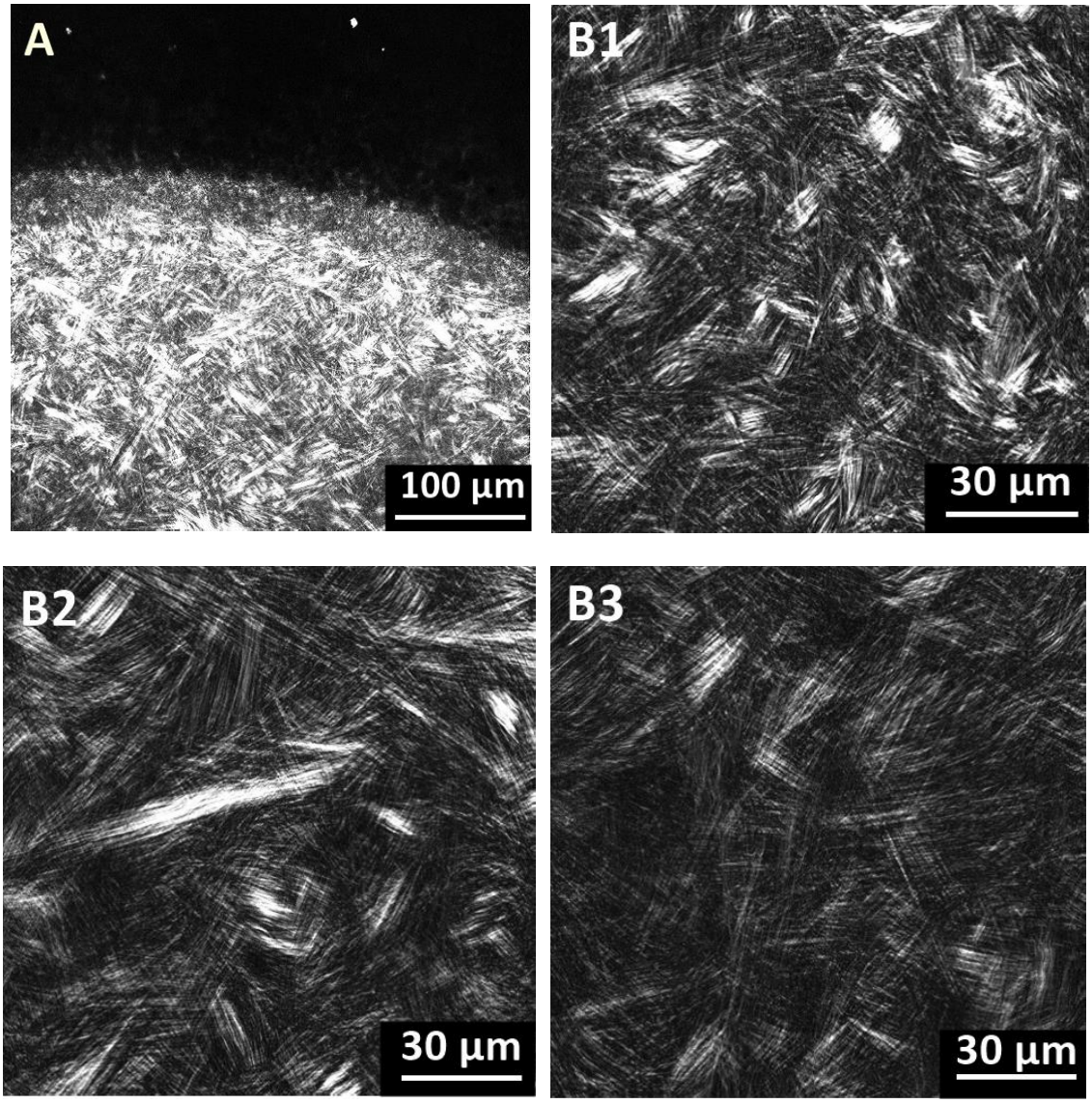

Figure 3.8: Three dimensional SHG imaging: A) A vertical cross sectioning visualization of collagen within the stroma based on the z stacks of 800 lateral sections recorded at an axial step of 0.57 µm into a deepness of 456 µm within the sample. B) A lateral cross sectioning image through the stroma recorded at three different axial depth: from an anterior zone (B1), an intermediate zone (B2) to posterior zone (B3). The excitation power is approximately 15 mW at the wavelength of 810 nm. The nonlinear signal from the collagen within the corneal stroma is detected in the forward direction with the NDD in the range of 400-410 nm.

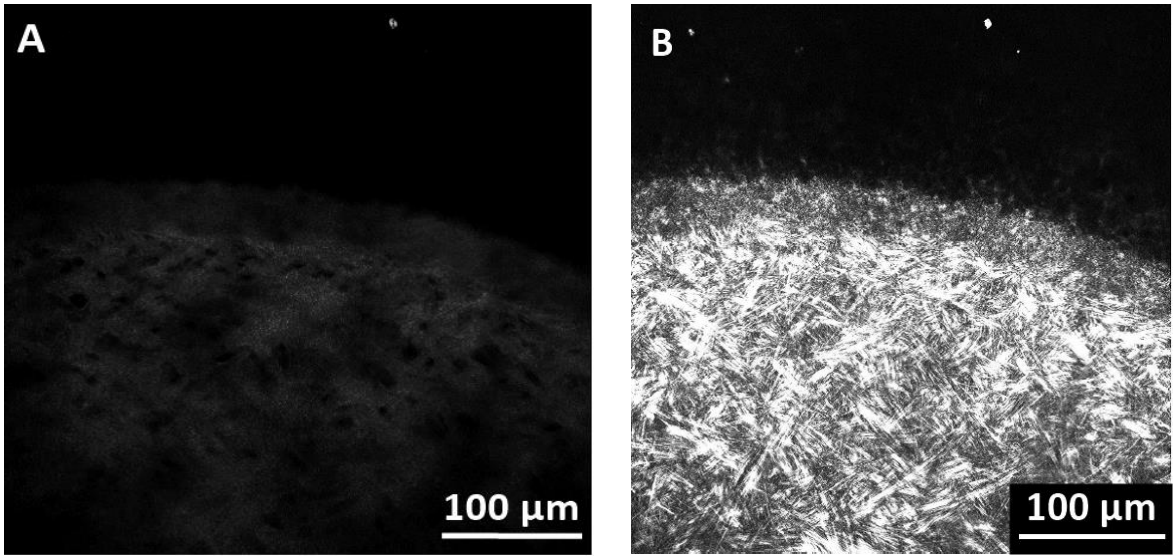

Figure 3.9: Images of SHG vertical cross-section from the collagen within the stroma detected in the backward (A) and in the forward (B) directions. The excitation power is approximately 15 mW at the wavelength of 810 nm. The SHG signal from the collagen is detected in the backward direction with the NDD1 and in the forward direction with the NDD in the range of 400-410 nm.

3.4 Conclusion

In this work, we demonstrate 3D manipulation and nonlinear imaging capabilities of the SHG/TPEF integrated setup, where the human cornea was tested as an example of a biological tissue with a high thickness close to *ex vivo* condition. The 3-D high resolution imaging demonstrated the feasibility of nonlinear optical microscopies in the visualization of the morphology and the structural arrangement within corneal tissue. As a result, multiphoton microscopy can be used to achieve in-depth bioimaging without invasive histologic procedures. This knowledge would enhance our understanding of the arrangement and interactions between stromal components, which have been shown to be highly correlated to corneal depth.

We demonstrated the feasibility of introducing the suitable filter in the detection channel in resolving the SHG signal from the TPEF signal. Thus, autofluorescence imaging can be

used to identify cellular components of the cornea as epithelial cells and cells within connective tissues, whereas SHG is useful in imaging corneal collagen fibers. To image then in deep tissue with live cells, the non linear optical microscopies are the most effective optical sectioning microscopies. Whereas, for imaging thinner samples two-photon excitation microscopy does not provide significant advantages over confocal microscopy or other 3-D imaging techniques. In fact, the wavelength of light for two-photon excitation is approximately twice that for one photon excitation. Thus, the axial and lateral resolution will actually be worse for two-photon microscopy compared to a perfect confocal microscope with an equivalent microscope objective. In the following chapter, the feasibility of using confocal microscope for imaging thin, fixed and labelled tissues will be demonstrated.

References

[1] M. E. Dailey, E. Manders, D. R. Soll, and M. Terasaki. Confocal microscopy of living cells. *Handbook of Biological Confocal Microscopy, third edition, edited by James B. Pawley, Springer Science+Business Media, New Yor*k, 2006, 19: 381-403.

[2] M. Chalfie, Y. Tu, G. Euskirchen, W. W. Ward, and D. C. Prasher. Green fluorescent protein as a marker for gene expression. *Science*. 1994, 263:802–805.

[3] P. I. Bastiaens, R. Pepperkok. Observing proteins in their natural habitat: The living cell. *Trends Biochem. Sci*. 2000, 25:631–637.

[4] N. A. O'Rourke, S. E. Fraser. Dynamic changes in optic fiber terminal arbors lead to retinotopic map formation: An *in vivo* confocal microscopic study. *Neuron*. 1990, 5:159–171.

[5] U. Tauer. Advantages and risks of multiphoton microscopy in physiology. *Exp. Physiol*. 2002, 87:709–714.

[6] D. W. Piston, B. R. Masters, W. W. Webb. Three-dimensionally resolved NAD(P)H cellular metabolic redox imaging of the in situ cornea with two-photon excitation

laser scanning microscopy. *J Microsc.* 1995, 178:20–27.

[7] D. Huang D, E. A. Swanson, C. P. Lin. Optical coherence tomography. *Science.* 1991;254:1178–1181.

[8] J. G. Fujimoto, C. Pitris, S. A. Boppart, M. E. Brezinski. Optical coherence tomography: an emerging technology for biomedical imaging and optical biopsy. *Neoplasia*. 2000, 2:9 –25.

[9] A. F. Fercher, W. Drexler, C. K. Hitzenberger, T. Lasser. Optical coherence tomography: principles and applications. *Rep Prog Phys*. 2003, 66:239–303.

[10] W. Denk, J. H. Strickler, W. W. Webb. 2-Photon laser scanning fluorescence microscopy. *Science*. 1990, 248:73–76.

[11] P. T. C. So, C. Y. Dong, B. R. Masters, K. M. Berland. Two-photon excitation fluorescence microscopy. *Annu Rev Biomed Eng*. 2000, 2:399–429.

[12] C. Ricard, B. Vacca, P. Weber. Three-dimensional imaging of small intestine morphology using non-linear optical microscopy and endogenous signals. *J. Anat*. 2012, 221: 279–283

[13] J. A. Palero, H. S. de Bruijn, A. P. Heuvel, H. J. C. M. Sterenborg, H. C. Gerritsen. Spectrally Resolved Multiphoton Imaging of In Vivo and Excised Mouse Skin Tissues. *Biophysical Journal*. 2007, 93: 992–1007.

[14] J. P. Whitcher, M. Srinivasan, and M. P. Upadhyay. Corneal blindness: a global perspective. *Bull. World Health Organ*. 2001, 79(3), 214–221.

[15] A. Kruger, M. Hovakimyan, D. F. Ramírez Ojeda, O. Stachs, A. Wree, R. F. Guthoff, A. Heisterkamp. Combined Nonlinear and Femtosecond Confocal Laser-Scanning Microscopy of Rabbit Corneas after Photochemical Cross-Linking. *Investigative Ophthalmology & Visual Science.* 2011, 52 (7): 4247-4255.

[16] M. H. Ross, G. I. Kaye, W. Pawlina. *Histology.* 4th ed. Baltimore, MD: Lippincott Williams & Wilkins. 2003:788–810.

[17] D. M. Maurice. The structure and transparency of the cornea. *J. Physiol*. 1957, 136(2): 263–286.

[18] R. Brinkmann, B. Radt, C. Flamm, J. Kampmeier, N. Koop, R. Birngruber.

Influence of temperature and time on thermally induced forces in corneal collagen and the effect on laser thermokeratoplasty. *J Cataract Refr Surg*. 2000, 26:744–754.

[19] D. D. Koch, T. Kohnen, J. A. Anderson . Histologic changes and wound healing response following 10-pulse noncontact holmium: YAG laser thermal keratoplasty. *J Refract Surg*. 1996, 12:623–634.

[20] T. Kohnen, S. E. Husain, D. D. Koch. Corneal topographic changes after noncontact holmium: YAG laser thermal keratoplasty to correct hyperopia. *J Cataract Refract Surg*. 1996, 22:427–435.

[21] M. N. AsiyoVogel, R. Brinkmann, H. Notbohm, R. Eggers, H. Lubatschowski , H. Laqua. Histologic analysis of thermal effects of laser thermokeratoplasty and corneal ablation using sirius-red polarization microscopy. *J Cataract Refract Surg*. 1997, 23:515–526.

[22] H. S. Dua, A. Azuara-Blanco. Limbal stem cells of the corneal epithelium. *Surv Ophthalmol*. 2000, 44:415–425.

[23] J. M. Wolosin, X. L. Xiong, M. Schutte, Z. Stegman, A. Tieng. Stem cells and differentiation stages in the limbo-corneal epithelium. *Prog Retin Eye Res*.2000,19:223–255.

[24] H. J. Van Schaik, C. Alkemade, W. Swart, J. A. Van Best. Autofluorescence of the diabetic and healthy human cornea in vivo at different excitation wavelengths. *Exp Eye Res*. 1999, 68:1– 8.

[25] C. L. Shields, J. A. Shields. Tumors of the conjunctiva and cornea. *Surv Ophthalmol*. 2004, 49:3–24.

[26] P. G. Watson, R. D. Young. Scleral structure, organisation and disease: a review. *Exp Eye Res.* 2004,78:609–623.

[27] H. Hanry, N. A. Abdul Rahim. Imaging in tissue and cellular engineering. *Taylor and Francis group LLC*. 2013.

[28] G. Lombardo, N. L. Micali, V. Villari, S. Serrao, M. Lombardo. All-Optical Method to Assess Stromal Concentration of Riboflavin in Conventional and Accelerated UV-A Irradiation of the Human Cornea. *IOVS*. 2016, 57(2): 476-483

[29] M. Lombardo, D. Merino, P. Loza-Alvarez, G. Lombardo. Translational label-free nonlinear imaging biomarkers to classify the human corneal microstructure. *Biomedical Optics Express.* 2015, 6(8): 2803-2818.

[30] S. W. Teng, H.Y. Tan, J. L. Peng, H. H. Lin, K. H.Kim, W. Lo,Y. Sun, W. C. Lin, S. J. Lin, S. H. Jee, P. T. C. So, C. Y. Dong. Multiphoton Autofluorescence and Second-Harmonic Generation Imaging of the Ex Vivo Porcine Eye. *Invest Ophthalmol Vis Sci.* 2006;47:1216–1224.

Chapter 4

Endothelial-like nitric oxide synthase immunolocalization by using gold nanoparticles and dyes

4.1 Introduction

In this chapter, skeletal muscle cells from lungfish Protopterus annectens are served in this work as an example to illustrate that confocal microscopy is a suitable tool for the localization of microstructures within fixed tissues with a thickness of several micrometers. The features of interest are the endothelial-like NOS protein.

Nitric oxide (NO), produced by the different nitric oxide synthases (NOSs) isoforms including endothelial-like NOS (eNOS) have ubiquitous tissue locations, including skeletal muscles. It exerts an universal multi-faceted regulatory role, including modulation of the aerobic biome (redox and energy balance) and cardio-circulatory homeostasis and muscle contractile efficiency [1–4]. In previous studies by using immunofluorescence technique the eNOS enzyme has been localized in different tissues including skeletal muscles of mammalian and non mammalian vertebrates (for example in the lungfish *Protopterus*

annectens). On the basis of our previous experience on the morphology and NOS/NO system in lungfish skeletal muscle, we used, in the present work, this experimental model. Immunofluorescence is a biological technique that, exploiting the antigen-antibody reaction, where the antibody is labelled with a fluorescent dye, allows displaying the localization of the target molecule (antigen) through a fluorescent microscope. The major limits of immunofluorescence was represented by autofluorescence of some tissues, which can interfere with the fluorescence of labeled antibody [5,6]. All cells have some intrinsic level of autofluorescence, which is most commonly caused by NADH, riboflavins, and flavin coenzymes [7,8]. These molecules excite over a broad range of wavelengths including the blue region of the spectra. The emission wavelengths of these autofluorescent molecules when excited in the blue is broad (500–700 nm) and overlaps emission spectra of commonly used fluorescent dyes. The peak autofluorescence emission after 488 nm excitation is in the green region of the spectra [9], heavily overlapping with the FITC fluorescence detection region.

Thus, the immunofluorescence technique is negatively impacted by this overlap and effective contrast agents are highly desirable for these technique. The fluorescence emission can be altered when the fluorophore is placed near a material possessing a surface electromagnetic (plasmon) field as described in chapter 2. Nano-sized metal particles form high plasmon field around them, upon receiving optical energy [10,11] and therefore are investigated as contrast agents. Exemplary metal entities for this purpose are nanoparticles of gold, silver, platinum, copper, etc [12,13]. For biological imaging, gold is one of the best candidates due to its surfacechemistry, photostability, water solubility and non toxicity proprieties [14–16].

In this work we will show the feasibility of combining the LSCM microscopy to an other fluorescent technique which is the forester resonance energy based on the interaction between gold nanoparticles (AuNPs) and FITC dyes to enhance contrast images between autofluorescence and emitted signal from target eNOS.

4.2 Materials and methods

4.2.1 Gold nanoparticles

For our experiments we used commercially available GNPs, obtained from Sigma Aldrich as stabilized suspension in citrate buffer with a core size of 37-43 nm and a mean hydrodynamic diameter of 48-56 nm. GNPs are typically synthesized using citrate-reduction of Au ions in an aqueous solution, which results in the GNPs surfaces covered with citrate anions. To minimize their aggregation, the versatile surface chemistry of citrate capped GNps allows them to be coated with hydrophilic polymer layer on their surface via electrostatic interaction. Usually, the cetyltrimethylammonium bromide (CTAB), a cationic surfactant with a positive hydrophilic ammonium head group and a hydrophobic long hydrocarbon tail, is used to convert the surface charge from negative to positive (Figure 4.1)[17]. The absorption spectrum of the solution containing the dispersed GNPs (Figure 4.2) was measured through a UV-vis-NIR spectrophotometer AVASPE-2048 Avantes. Since surface plasmon resonance (SPR) is a collective oscillation of free electrons in a metallic nanoparticle, it will cause a strong scattering as well as absorption of light simultaneously. Therefore, the SPR band of GNPs can be identified by using the absorption spectrum of dispersed GNPs. Our observations show that SPR band of the GNPs used for this work ranges from 400 nm to 600 nm, with a peak at 525 nm (Figure 4.1).

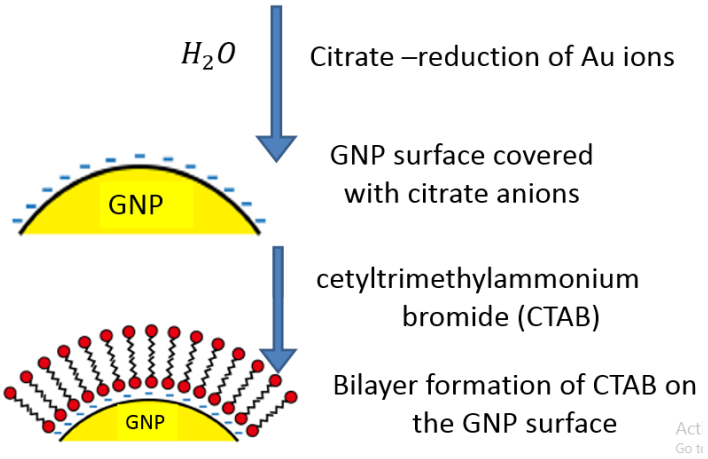

Figure 4.1: GNP covered with a bilayer film of surfactants with positively charged hydrophilic head groups

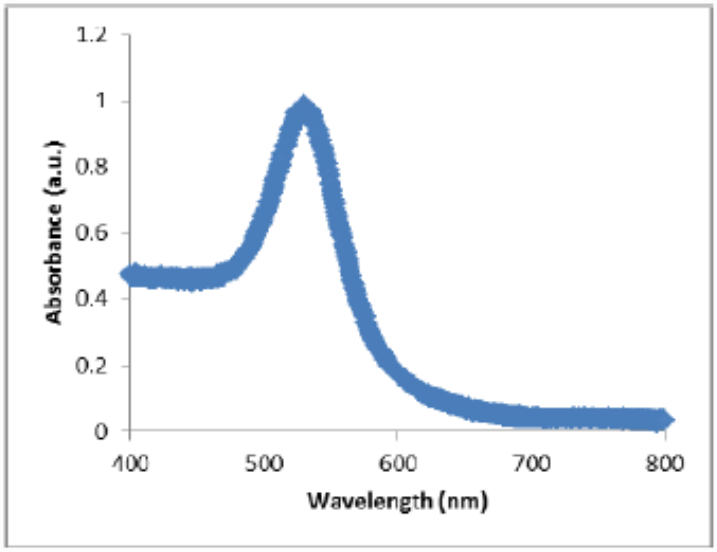

Figure 4.2. The absorption spectrum of GNPs stabilized suspension in citrate buffer.

4.2.2. Tissue samples

Skeletal muscles from lungfish *Protopterus annectens* (n = 3) were flushed in phosphatebuffered saline (PBS). Then samples were fixed in a solution (methanol:acetone:water = 2:2:1), dehydrated in graded ethanol (90% and 100%), cleared in xylol, embedded in paraplast (Sigma), and serially sectioned at 8 μm. The sections were placed onto Superfrost Plus slides (Menzel-Glaser, Braunschwerg, Germany), deparaffined in xylene, and rehydrated in an alcohol gradient. Several sections were stained with either hematoxylin and eosin for a general assessment of tissue structure.

4.2.3 Immunofluorescence

Tissue sections, obtained as previously described, were rinsed in tris-buffered saline (TBS) and incubated with 1.5% bovine serum albumin (BSA) in TBS for 1 h. Later they were incubated overnight at 4°C with rabbit polyclonal primary antibody directed against eNOS (Sigma, 1:100). For signal detection, slides were washed in TBS (3 x 10 min), and incubated with FITC-conjugated anti-rabbit secondary antibody (Sigma; 1:100). For

nuclear counterstaining, sections were incubated with Propidium Iodide (PI, Sigma; 1:10.000) for 5 min. Negative controls were performed omitting the incubation with both AuNPs and the primary antibody anti-eNOS. To verify the influence of GNPs on FITC emitted signal some slides were pretreated overnight at 4°C with GNPs suspension in citrate buffer. Slides were then mounted with mounting medium (Vectashield, Vector Laboratories), and observed under a Leica TCS SP8 LSCM.

4.2.4 Lasers and detections bandwidths of LSCM

The Ar+ laser 458/488/496/514 nm was used as pump beam. For each imaging, a single laser beam is used to irradiate the sample, the fluorescent emission was sent to a photomultiplier (PMT). Concerning the setting of the PMT1 detection range, the excitation and emission spectra of the dyes as well as the wavelength of the laser need to be taken into account. The excitation band of FITC is from 450 nm to 520 nm, where the maximum excitation occurs at 495 nm, and the emission band of FITC is from 490 nm to 630 nm, where the maximum emission of the fluorescence is at about 520 nm [18]. Therefore, only when the wavelength of laser is within the excitation spectrum of the FITC, the fluorescence can be induced, whose emission spectrum shows a narrow Stokes shift (20 nm). To avoid also the contamination from the scattered light, the detection range is set to be beyond the excitation wavelength. For that, a gap of 10 nm at least between the excitation wavelength and the detection range was taken into account in our experiments as listed in Table 4.1.

Table 4.1. The detection ranges of PMT for cells treated with FITC

laser	458 nm	488nm	496nm	514nm
PMT range	490-700 nm	498-700 nm	506-750 nm	524-750nm

In addition, using a pinhole, the out-of-focus signals are rejected, so the optical section image of the focal plane can be obtained. The size of the confocal pinhole is set to be 1 airy

units. The optical-section images are obtained at the same depth inside the sample (middle). Slides were observed with the 25 × / 0.95 NA and 40 × / 0.12 NA water immersion objectives.

4.2.5 Scanning electron microscopy

An environmental scanning electron microscope (ESEM) Quanta 400F by FEI Company has been used to image the tissue samples prepared with GNPs at pressure of 1 mbar and voltage 5-10 kV.

4.2.6 Statistical analysis

Analysis of fluorescence intensity (according to Lichocka and Schmelzer, 2014) [19] and Plot Profiles were performed using ImageJ software (ver. 1.46r, NIH, USA). Differences between the two groups (i.e. with and without GNPs) were evaluated by non-parametric Mann– Whitney U test. Statistical significance was established at §$p < 0.05$, §§$p < 0.005$ and §§§$p < 0.0005$. The statistical analysis of the data was performed using GraphPad InStat® software, version 3.10 for Windows.

4.3. Results and discussion

4.3.1 Localisation of eNOS

Haematoxilin eosin stained sections (Figure 4.3) showed basic structural features of *P. annectens* skeletal muscle. In particular skeletal muscle fibers appears with nuclei located close to the sarcolemma. The tissue appears vascularised by capillary vessels whose lumen is coated by vascular endothelium.

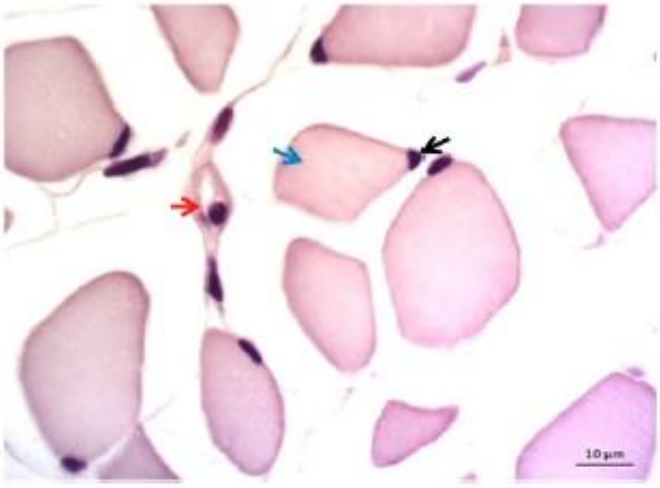

Figure 4.3. Basic histological features of the *P. annectens* skeletal muscle Hematoxylin–eosin stained. Blu arrow = skeletal muscle cell, black arrow = nuclei of muscle cell, red arrow = capillary vessel with nucleus of vascular endothelium.

According to Amelio et al., 2013 [1], in the skeletal muscle of *P. annectens*, eNOS was densely localized on the sarcolemma (Fig. 4.4(b); Fig. 4.4(a) represents the negative control). Autofluorescence in cells is due NADH, riboflavins, and flavin coenzymes. The emission wavelengths of these autofluorescent molecules when excited in the blue is broad (500–700 nm) [7,8,18]. As the excitation band of FITC is from 450 nm to 520 nm and its emission band is from 490 nm to 630 nm [18], there is a strong overlap between autofluorescence and emitted fluorescence from eNOS, which explains the weak contrast between the two signals as shown in Fig. 4.3(b). This overlap observation is in agreement with the ratio, measured on Fig. 4.3(b), of average fluorescence intensity from eNOS within the sarcolemma (positive signal = P) *versus* average autofluorescence intensity (negative signal = N) (P/N = 1.016263).

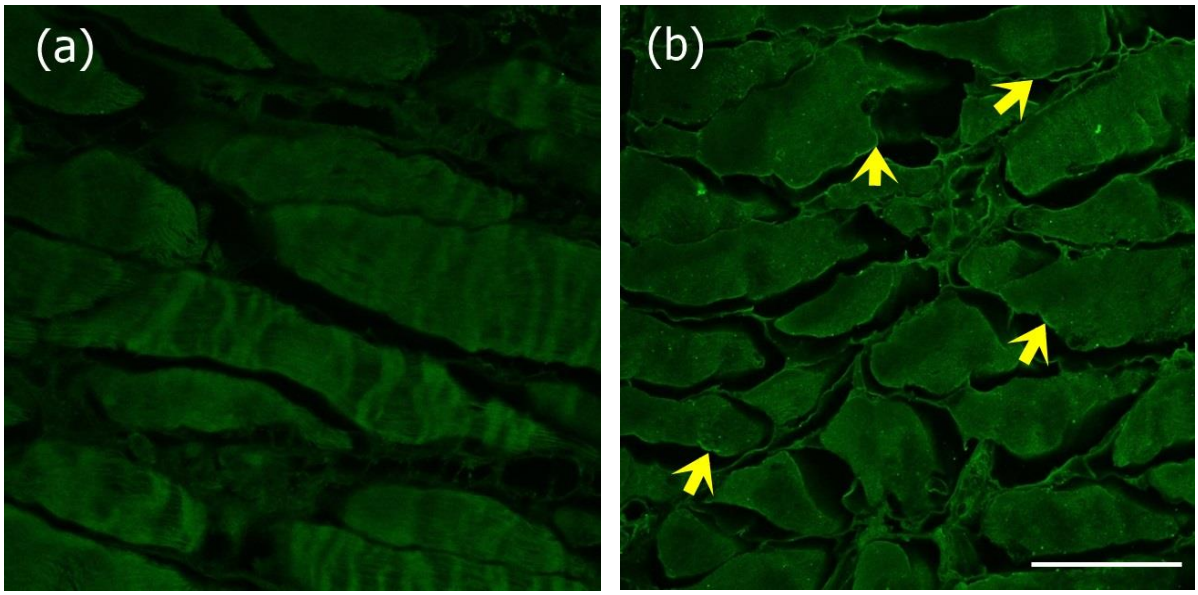

Figure 4.4. Immunolocalization of eNOS (b) in the skeletal muscle of *P. annectens*. eNOS is localized mainly in sarcolemma (yellow arrows). Negative control is shown in (a). The 496 nm wavelength is used as pump beam. The emitted signal is detected with the PMT1 in the range of 506-750 nm. Images are observed with the of 25 × water immersion objective. The scale bar denotes 75μm, which is the same for the two images.

4.3.2 Immunolocalization of eNOS with GNPs

Getting the best data from the LSCM images requires to obtain the largest possible difference between the signal from fluorescent labelled targets (eNOS) and the autofluorescence. As depicted in Figure 4.4, under different laser illumination conditions (458 nm, 488 nm, 496 nm, and 514nm), the contrast between the autofluorescence and emitted fluorescence from eNOS is enhanced in images of tissues treated with GNPs (Figs. 4.5(A) 4.5(e), 4.5(f), 4.5(g), 4.5(h)) compared to untreated tissues (Figs. 4.5(A) 4.5(a), 4.5(b), 4.5(c), 4.5(d)). The results of calculated ratios (P/N) in each image in Fig. 4.5(A) are reported as a diagram (Fig. 4.5(B)). This diagram shows an enhancement of the ratio measured for images of tissues treated with GNPs. This contrast optimization is due to an

enhancement of emitted fluorescence from eNOS, which is explained by a resonant energy transfer (RET) between GNPs (donor) and FITC (acceptor).

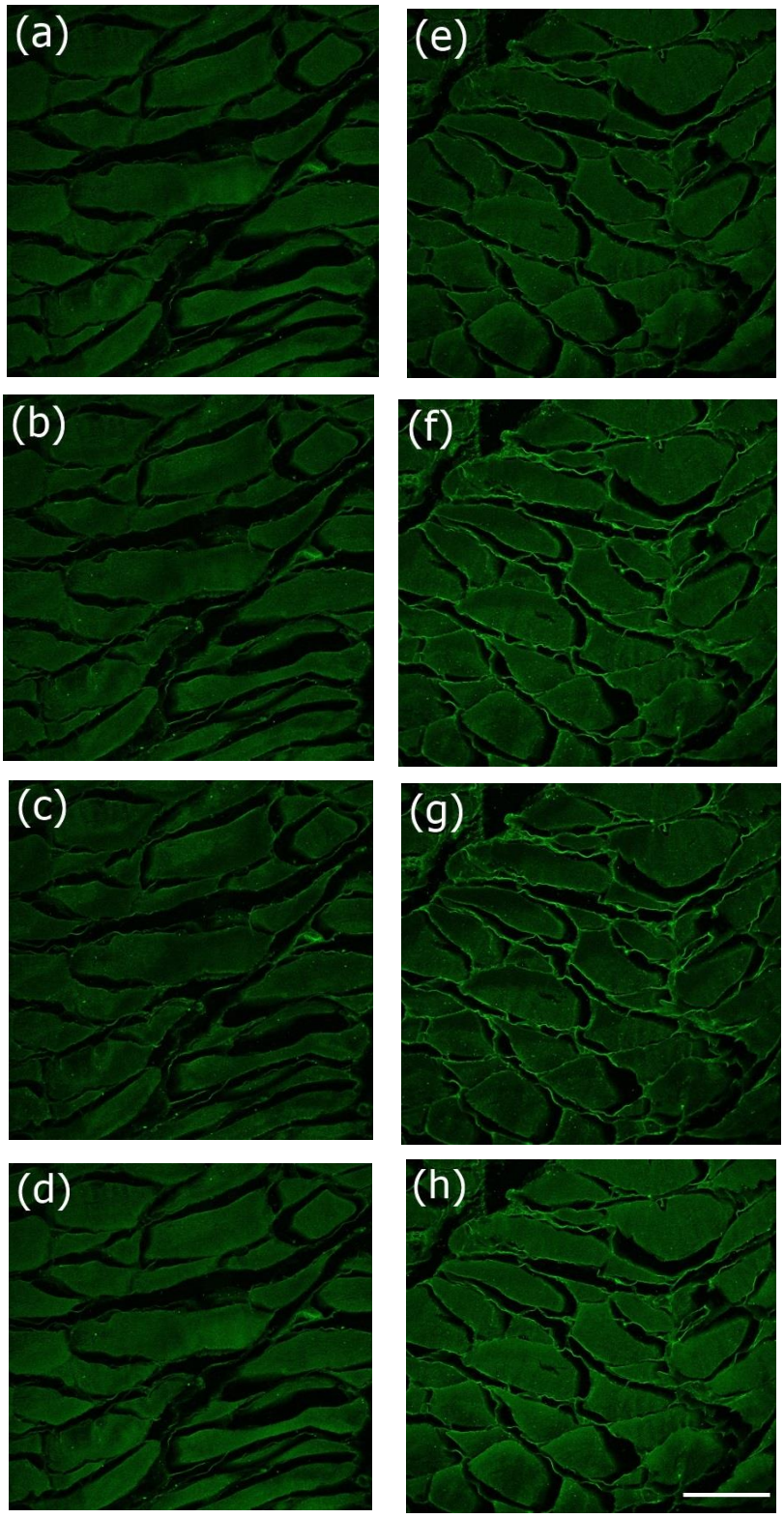

Figure 4.5.A.

Immunolocalization of eNOS in skeletal muscles of *P. annectens* without treatment with GNPs (top) and after incubation with GNPs (bottom) under an excitation of different lasers: (a) and (e) 458nm, (b) and (f) 488nm, (c) and (g) 496nm, (d) and (h) 514nm. The detection ranges of emitted light are listed in Table 4.1. Each two images observed under the same excitation wavelength (with and without GNPs) are acquired under the same set of the offset, gain of PMT1 and power of the laser. All images are observed with the 25 × water immersion

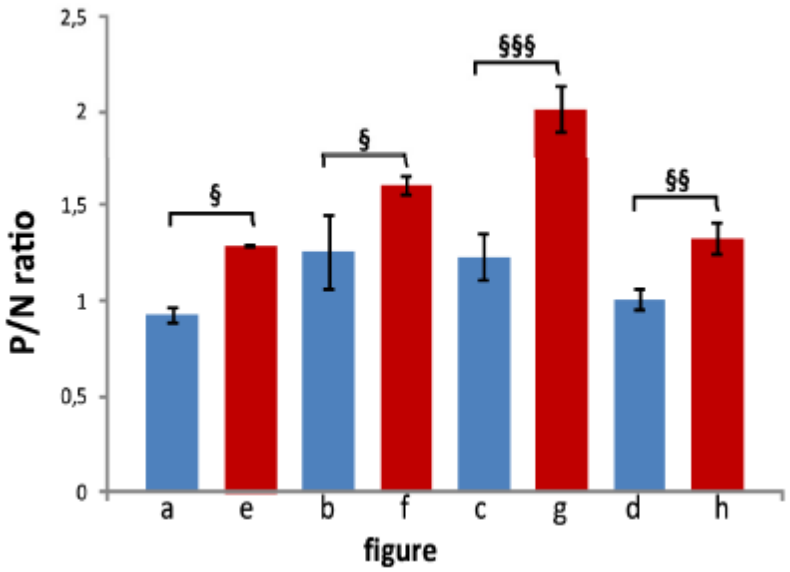

Figure.4.5.B. The diagram shows the ratios of the average intensity from eNOS *vs* the average of the autofluorescence intensity (P/N ratio) in each image in 4.5.A. Statistical differences were evaluated by non-parametric Mann–Whitney U test (§$p < 0.05$, §§$p < 0.005$ and §§§$p < 0.0005$).

The ESEM images (Fig. 4.6) show a distribution of GNPs in the sarcoplasm and in the vascular endothelium avoiding the nuclei. The sarcoplasm is made up of mostly water and salt. The endothelium also, contains the channels of molecule water, the aquaporins [20]. That means that the attachment of GNPs to skeletal muscle cells is due to the hydrophilic interaction between the head groups of the polymeric film covering their surface and molecules of water in sarcoplasm and endothelium.

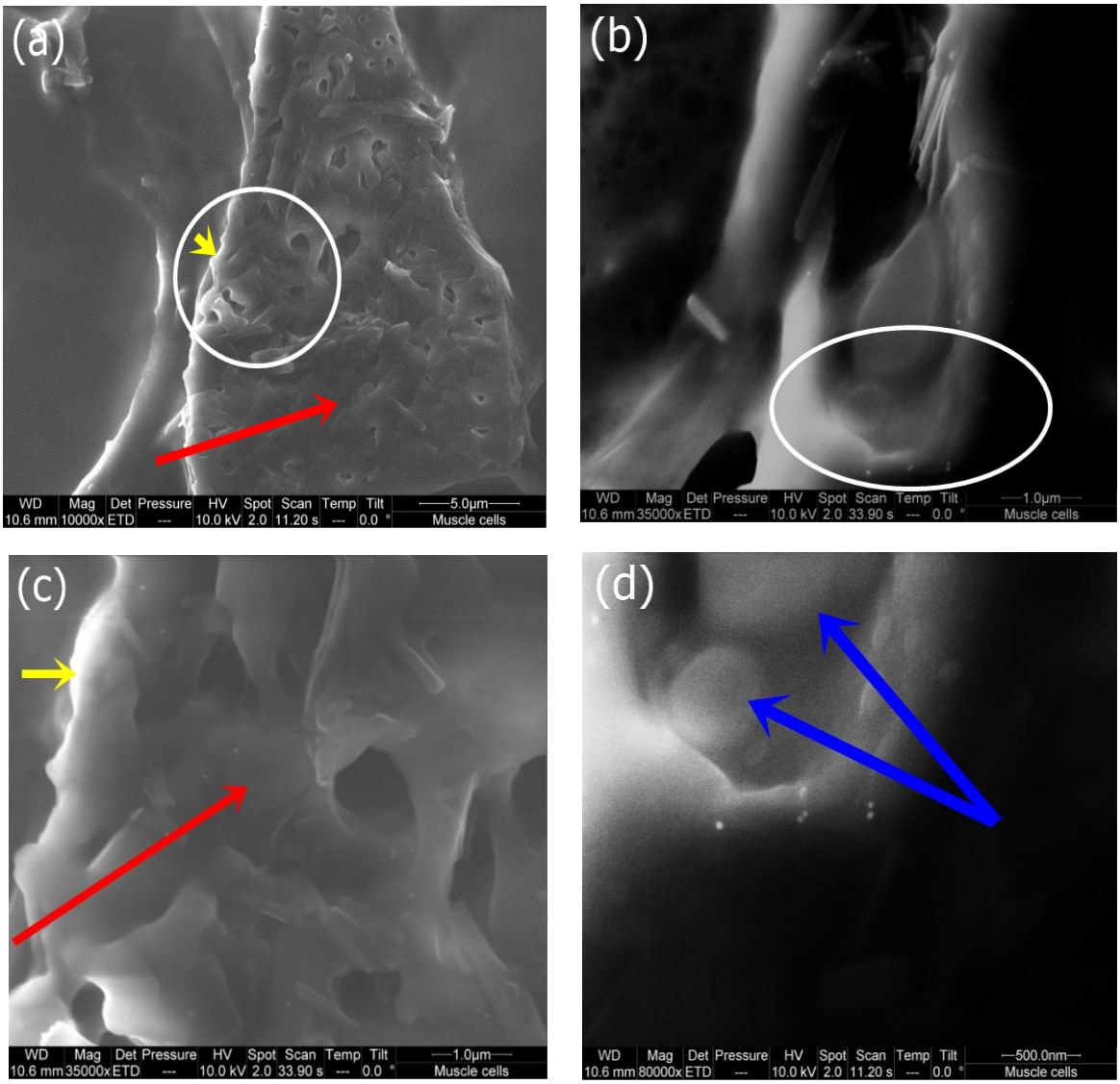

Figure 4.6. ESEM images of skeletal muscle cells, (a) and (c), with sarcoplasm (red arrows), sarcolemma (yellow arrows) and vascular endothelium, (b) and (d), in which are evident the nuclei (blue arrows) after incubation with GNPs for 24 hours. (c) and (d) are images of higher magnification of images (a) and (b) respectively at the regions marked with the white contour. The GNPs appear at higher magnification as spots brighter than the tissue.

The localization of GNPs within the sarcoplasm and vascular endothelium explain the enhancement of emitted fluorescence from eNOS. When a fluorophore is placed at a

relatively short distance, for instance within 10 nm, from a metal particle possessing a strong plasmon field, the electrons of the fluorophore participating in the excitation/emission interact with the field. The interaction results in a change in the fluorescence emission level, i.e. quenching or enhancement [10,21] as discussed in section 2.3.3.2. When the excitation decay rate of the fluorophore is increased due to the plasmon field generated around the particle by the incident light, the level of fluorescence emission is enhanced improving the performance of the fluorescence contrast agents [22,23].

As shown in Figure 4.5, the contrast between emitted fluorescence from eNOS and the autofluorescence is improved in all of the images e, f, g and h acquired respectively when the sample with GNPs is irradiated with the lasers of 458, 488, 496, and 514nm wavelengths. Since the wavelength of these laser beams are within both the excitation band of FITC and the SPR band of GNPs, the resonance energy transfer is induced. As depicted in Fig. 4.5(c), 4.5(g) and Fig. 4.7, the greater image contrast is obtained when the sample is irradiated with the laser beam at 496 nm and the emitted signal is detected in the 506-750 nm range. The Plot Profile of fluorescence intensity in a single cell (Fig. 4.7(A), a1 and b1) and the ratio diagram (Fig. 4.7(B)) show the stronger enhancement of the fluorescence from eNOS within the sarcolemma in image of tissue treated with GNPs (Fig. 4.7(A), 4.7(b)) compared to untreated tissues (Fig. 4.7(A), 4.7(a)) (the average of the fluorescence intensity from eNOS is doubly enhanced compared to the autofluorescence in the presence of GNPs, P/N = 2.114). Thus, the laser of 496 nm is the best candidate to obtain the higher contrast since this wavelength is the closer one to the excitation peak of FITC (495nm). Moreover, the contrast between the desired signal from target eNOS and autofluorescence for treated sample with GNPs observed with the 40 × /0.12 NA water immersion objective (Fig. 4.7) is larger than in observations under the 25 × /0.95 NA water immersion objective, which is explained by the aberration reduction for lower numerical aperture.

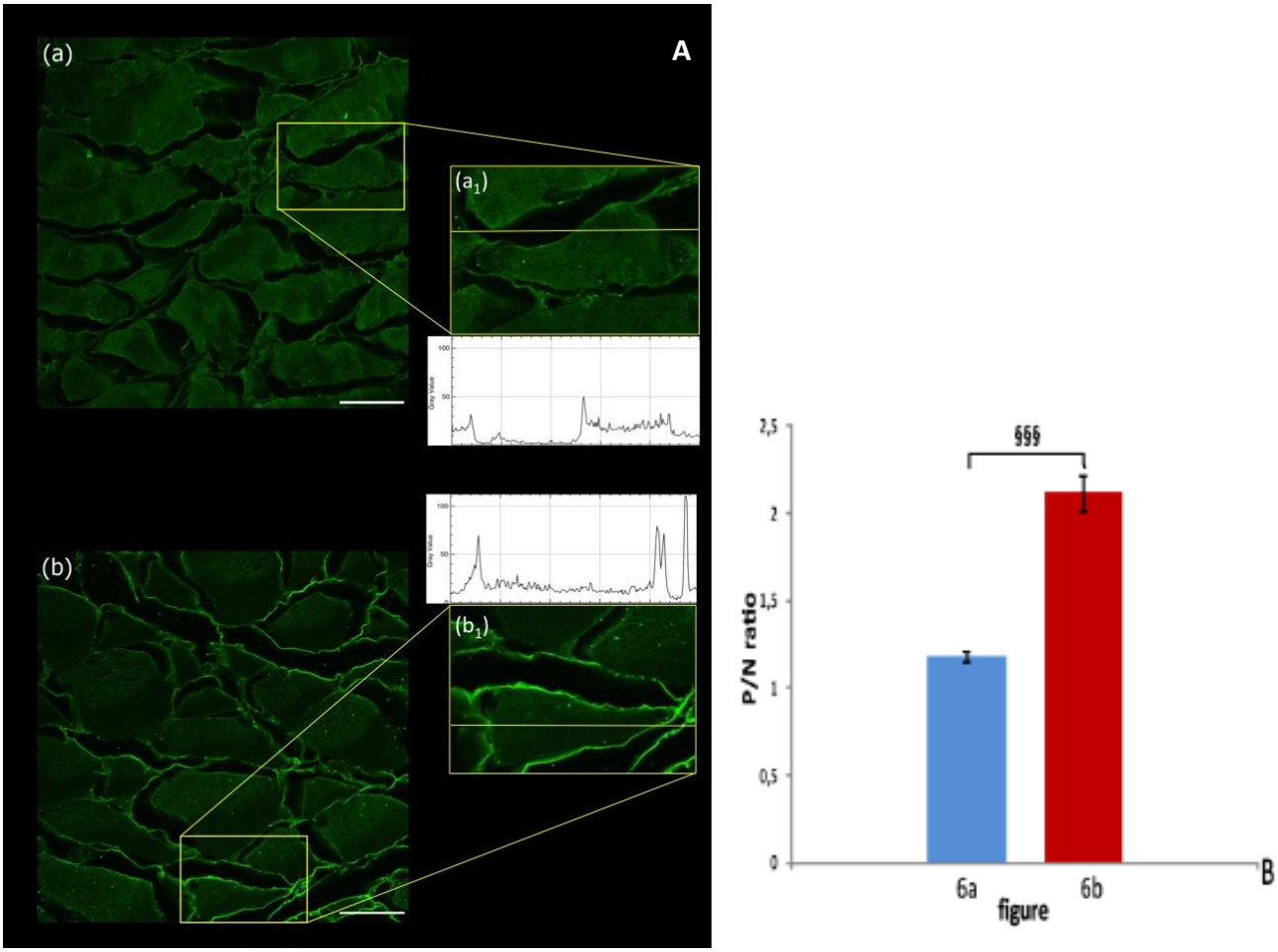

Figure 4.7. A. Immunolocalization of eNOS in lungfish skeletal muscles of *P. annectens* without treatment with GNPs (a) and after incubation with GNPs (b) under an excitation of the 496 nm laser beam. The detection range of emitted light is 506-750 nm. The two images are acquired under the same set of offset, gain of PMT1 and power of the laser. Images are observed with the 40 × water immersion objective. The scale bar denotes 50 μm, which is the same for the two images. In a1 and b1 are reported the plot profile of fluorescent intensity in a single cell. 7. B. Diagram of the ratios of the average intensity from eNOS *vs* the average of the autofluorescence intensity (P/N ratio) in each image in A. Statistical differences were evaluated by non-parametric Mann–Whitney U test (§$p < 0.05$, §§$p < 0.005$ and §§§$p < 0.0005$).

4.3.3. Immunolocalization of eNOS in the presence of PI

Previously we showed that it's easier to detect signal from eNOS localized in sarcolemma, which became brighter when the sample was incubated with GNPs (Fig. 4.7(A), 4.7(b)). According to Amelio et al [2], eNOS is localized also in vascular endothelium. Therefore, in our case, to distinguish the eNOS localisation in vascular endothelium from sarcolemma, a nuclear counterstaining is necessary. Amelio et al stained nuclei with Hoechst 33342 [2]. The excitation band of Hoechst 33342 is from 307 nm to 409 nm, where the maximum excitation occurs at 350 nm, and its emission band is from 370 nm to 639 nm, where the maximum emission of fluorescence is at 461 nm [24]. With our LSCM setting it's not recommended to use the combination of Hoechst 33342 and FITC dyes since the FITC maximum emission occurs at the wavelength of 518 nm which is within the emission band of Hoechst. Thus, the Propidium Iodide (PI) is chosen in our experiments for nuclei counterstaining. The excitation band of PI is from 450 nm to 600 nm, where the maximum excitation occurs at 535 nm, and the emission band of PI is from 585 nm to 720 nm, where the maximum emission of fluorescence is at 620 nm [25]. After nuclear counterstaining with PI, another PMT2 is used PMT1 (FITC fluorescence detector) depends on the excitation/emission of each dye.

As shown in Fig. 4.8 there is also an overlap between the fluorescence spectra of FITC conjugated anti-rabbit polyclonal antibodies bound to eNOS and PI bound to nuclei recorded with lambda scan mode in respectively points marked as A and B in Fig. 4.9(A), 4.9(c). But contrarily to Hoechst, the maximum emission of FITC occurs outside the emission band of PI, thus it's possible to detect the maximum of FITC emission without contamination from PI fluorescence emission. Under an excitation of 496 nm, the range of PMT1 is set to be 500-565 nm to reject the fluorescence of PI. On the other hand, the range of PMT2 is set to 696-794 nm to avoid the maximum of contamination from the fluorescence of FITC. In this experiment the best candidate to irradiate the sample is the laser beam at 496 nm since this wavelength is within the excitation spectrum of the two

dyes and the SPR band of GNPs and it is also the closer wavelength to the FITC excitation peak (495 nm).

With the aid of the two PMTs, two cellular images are acquired individually. Each image is colorized by an artificial colour, according to the detection ranges of PMT1 and PMT2, where the green area is the expression of autofluorescence and fluorescence from eNOS (brighter green is from eNOS) and the red domains are the expressions of PI from nuclei. Furthermore, a compound image is obtained by merging the two images. Slides were observed with the 40 × /0.12 NA water immersion objective.

After nuclei counterstaining with PI, it's easier to distinguish between the localisation of eNOS in sarcolemma and in the vascular endothelium as shown in Fig. 4.9(A), 4.9(b) and 4.9(d). Moreover, even after the reduction of the detection bandwidth of emitted light from eNOS to avoid the maximum of contamination from PI fluorescence, the images of samples treated with GNPs showed a higher contrast between autofluorescence and emitted light from eNOS since the FITC emission maximum occurs at the wavelength of 518 nm, which is within the detection range of PMT1, rejecting the PI fluorescence. The ratio diagram (Fig. 4.9(B)) shows a fluorescence enhancement of FITC bound to eNOS localized in vascular endothelium in the presence of GNPs (P/N = 1.30782 for untreated sample whereas when the sample is treated with GNPs, P/N = 2.31865). Moreover, as depicted in Fig. 4.9(A), 4.9(b), the GNPs treatment improves the eNOS signal even in the sarcoplasm, which, in untreated tissues, was undetectable (Fig. 4.9(A), 4.9(a)). Therefore we considered arbitrarily equal to 1 the value of the P/N ratio for localized eNOS in the sarcoplasm for GNPs untreated tissues (darker pink histogram in Fig. 4.9(B)).

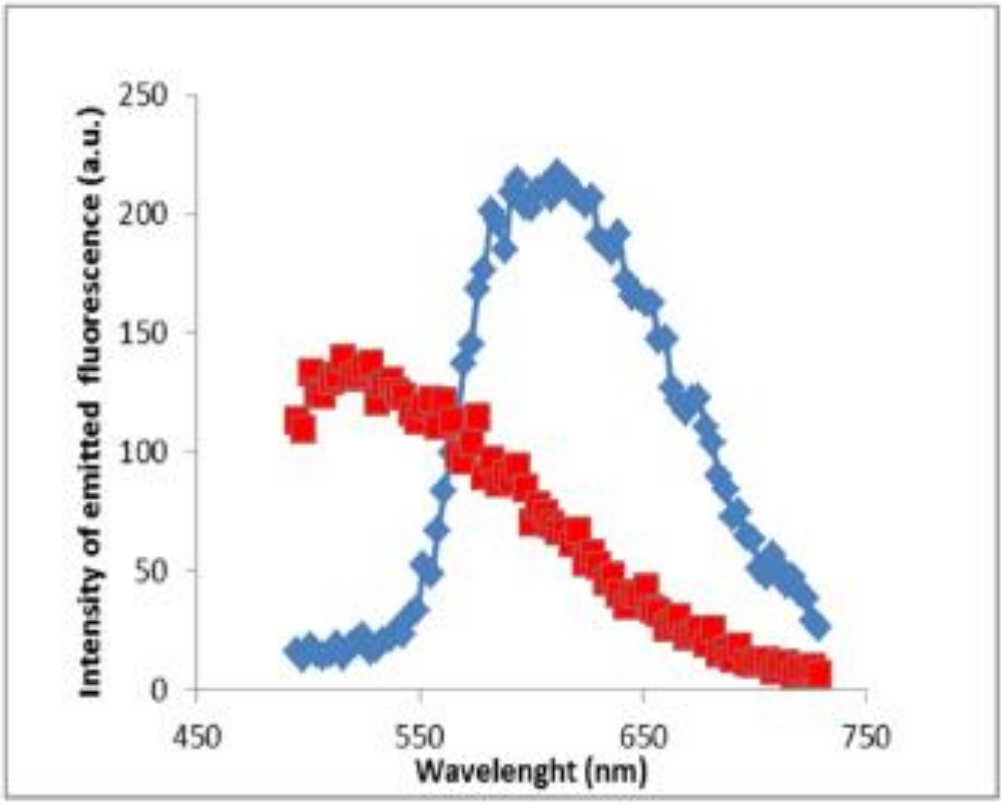

Figure 4.8. Fluorescence spectra of FITC bound to eNOS (red) and PI bound to nuclei (blue) recorded with lambda scan mode in respectively points marked as A and B in Fig. 4.8(A), 4.8(c). The emission is obtained under an excitation of 496 nm and it is detected in the 500-730 nm range.

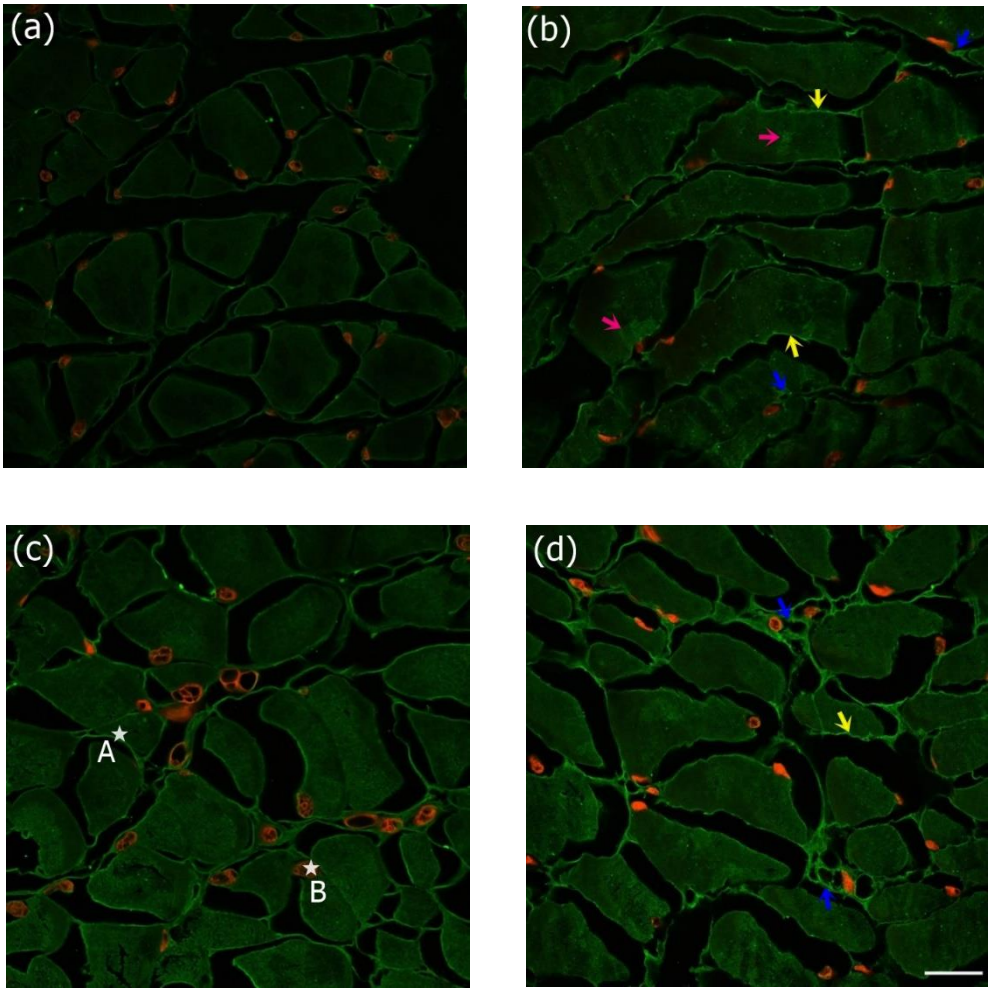

Figure 4.9. A. Higher LSCM images contrast for the localization of eNOS in vascular endothelium (blue arrows) in lungfish skeletal muscles *P. annectens* after incubation with GNPs and nuclei counterstaining with PI ((b) and (d)) in addition to their localization in sarcolemma (yellow arrows) and sarcoplasm (pink arrows) compared to images without GNPs ((a) and (c)) under an excitation of 496 nm. Emitted light from nuclei is detected in the 696-794 nm range and emitted light from eNOS and autofluorescence are detected in the 500-565 nm interval. Each couple of observed images, ((a), (b)) and ((c), (d)), is acquired under the same set of offset, gain of the two PMTs and power of the laser. All images are observed with the of 40 × water immersion objective. The scale bar denotes 50 µm, which is the same for all images.

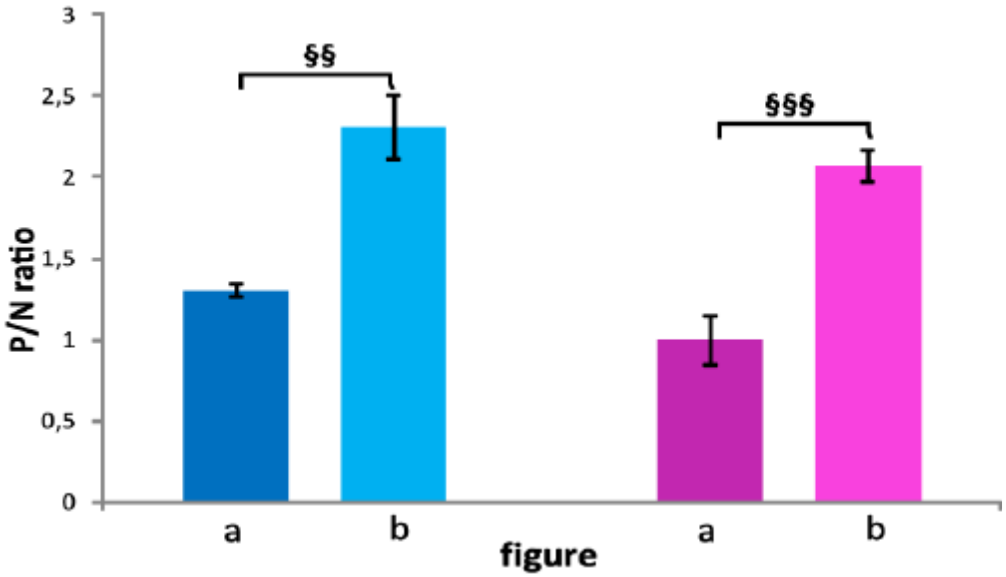

Figure.4.9.B. The diagram shows the ratios of the average intensity from eNOS vs the average of the autofluorescence intensity (P/N ratio) in images (a) and (b) in 4.9.A (blue histograms correspond to the P/N ratio for localized eNOS in vascular endothelium and pink histograms correspond to the P/N ratio for localized eNOS in sarcoplasm). Statistical differences were evaluated by nonparametric Mann–Whitney U test (§$p < 0.05$, §§$p < 0.005$ and §§§$p < 0.0005$).

4.5 Conclusion

Surface plasmon field of metal nanoparticles, in particular of GNPs, may be used for artificially manipulating fluorescence and, for instance, to improve biological imaging. In this work, we used a combination of GNPs and the fluorescence dye (FITC) for a cellular imaging of LSCM, where the skeletal muscle cells from lungfish *Protopterus annectens* were tested for the endothelial NOS localization. The Ar+ laser 458/488/496/514 nm was used as pump beam for the eNOS localization in sarcolemma. For each LSCM imaging, a single laser is used to irradiate the sample. The higher optical contrast between the autofluorescence and eNOS emitted signal is obtained when the GNPs treated sample is

irradiated with the laser beam at 496 nm and the emitted signal is detected in the 506-750 nm range, since this wavelength is within the SPR band of GNPs and it is the closer one to the excitation peak of FITC (494nm). ESEM images provide more information about the GNPs distribution in cells. The GNPs are localized in the sarcoplasm and the vascular endothelium avoiding nuclei, which confirms the GNPs attachment via hydrophilic forces. These GNPs result to be ideal to skirt the overlap problem between the autofluorescence and the FITC emitted signal, since they are placed closely to FITC dyes bound to eNOS, which results to an enhancement of FITC fluorescence, providing higher optical contrast. To distinguish between eNOS localized in sarcolemma and eNOS localized in vascular endothelium, nuclei are counterstained with PI. For that, in addition to the PMT1 detecting the FITC emitted signal, the PMT2 was set to detect the PI emitted signal. Since there is an overlap between the fluorescence spectra of PI bound to nuclei and FITC-conjugated anti-rabbit polyclonal antibodies bound to eNOS, the PMTs detected ranges were set in order to minimize the maximum crosstalk between the two signals.

References :

[1] S. Ahanchi, N. Tsihlis, M. Kibbe. The role of nitric oxide in the pathophysiology of intimal hyperplasia. *J Vasc Surg* , 2007, 45:64–73.

[2] D. Amelio , F. Garofalo, W.P. Wong, S.F. Chew, Y.K. Ip, M.C. Cerra, B. Tota. Nitric oxide synthase- dependent ‘‘On/Off’’ switch and apoptosis in freshwater and aestivating lungfish, Protopterus annectens: Skeletal muscle versus cardiac muscle. *Nitric oxide*, 2013, 32 :1-12.

[3] S. Imbrogno, B. Tota, A. Gattuso. The evolutionary functions of cardiac NOS/NO in vertebrates tracked by fish and amphibian paradigms. *Nitric Oxide*. 2011, 25 (1): 1–10.

[4] W. Shen, R. Tian, K.W. Saupe, M. Spindler, J.S. Ingwall. Endogenous nitric oxide enhances coupling between O2 consumption and ATP synthesis in guinea

pig hearts. *Am. J. Physiol. Heart Circ. Physiol*. 2001, 281 (2): 838–846.

[5] W. Baschong, R. Suetterlin, R. Hubert Laeng. Control of Autofluorescence of Archival Formaldehyde-fixed, Paraffin-embedded Tissue in Confocal Laser Scanning Microscopy (CLSM). *J Histochem Cytochem*. 2001, 49 (12): 1565-1571.

[6] R. Kittelberger, P. F. Davis,W. E. Stehbens . An improved immunofluorescence techniquefor the histological examination of blood vessel tissue. *Acta Histochemica* 1989, 86, (2): 137–142.

[7] J. Aubin. Autofluorescence of viable cultured mammalian cells. *J Histochem Cytochem*. 1979, 27: 36–43,

[8] R. Benson, R. Meyer, M. Zaruba,G. McKhann . Cellular auto fluorescence: Is it due to flavins?. *J Histochem Cytochem.1979,* 27:44–48.

[9] H. Shapiro. Practical Flow Cytometry. *Alan R. Liss, Inc., New York.* 1988.

[10] K. A Kang, J. Wang, J. B Jasinski and S. Achilefu .Fluorescence Manipulation by Gold Nanoparticles: From Complete Quenching to Extensive Enhancement. *Journal of Nanobiotechnology* . 2011, 9(16): 1-13.

[11] J. R. Lakowicz, M. H. Chowdhury, K. Ray, J. Zhang, Y. Fu, R. Badugu, C. R. Sabanayagam, K. Nowaczyk, H. Szmacinski, K. Aslan and C. D. Geddes. Plasmon-controlled fluorescence: A new detection technology. *Proceedings of SPIE Vol*. 2006, 6099(609909):1-15.

[12] M. Iosin, P. Baldeck, S. Astilean. Plasmon-enhanced fluorescence of dye molecules. *Nucl Instrum Meth B.* 2009, 267:403-405.

[13] E. Hutter and J. Fendler. Exploitation of localized surface plasmon resonance. *Adv Mater*. 2004,16:1685-1706.

[14] S. Kumar, N. Harrison, R. Richards-Kortum, and K. Sokolov. Plasmonic

Nanosensors for Imaging Intracellular Biomarkers in Live Cells. *Nano Lett*. 2007, 7(5): 1338-1343.

[15] B. D. Chithrani, A. A. Ghazani, W.C. W. Chan. Determining the size and shape dependence of gold nanoparticle uptake into Mammalian cells. *Nano Lett*. 2006, 6: 662-668.

[16] P. Yang, X. Sun, J. Chiu, H. Sun, Q. He. Transferrin-mediated gold nanoparticle cellular uptake. Bioconjugate Chem. 2005,16:494-496.

[17] J. Lim, N. Lee, E. Lee, and S. Yoon. Surface Modification of Citrate-Capped Gold Nanoparticles Using CTAB Micelles. *Bull. Korean Chem. Soc*. 2014, 35 (8): 2567-2569.

[18] J. Paul Robinson PhD, Jennifer Sturgis BS and George L. Kumar PhD, IHC Staining Methods, *5th Edition year,* Chap. 10.

[19] M. Lichocka and E. Schmelzer. Subcellular Localization Experiments and FRET-FLIM Measurements in Plants. *J.bioprotocol*.2014, 4 (1): 1-12.

[20] B. Yang, J. Vervabatz, Y. Song, L. Vetrivel, G. Manley, W. Kao, T. Ma, A. S. Verkman. Skeletal muscle function and water permeability in aquaporin-4 deficient mice. *Am J Physiol Cell Physiol*. 2000, 278:1108–1115.

[21] G. Schneider, G. Decher, N. Nerambourg, R. Praho, M. H. V. Werts, M. Blanchard- Desce. Distance-dependent fluorescence quenching on gold nanoparticles ensheathed with layer-by-layer assembled polyelectrolytes. *Nano letters* .2006, 6: 530-536.

[22] N. MY, L. WC. Fluorescence enhancements of fiber-optic biosensor with metallic nanoparticles. *Opt Express* 2009, 17: 5867-5878.

[23] KA. Kang and B. Hong. Biocompatible nano-metal particle fluorescence enhancers. *Critical Reviews in Eukaryotic Gene Expression*. 2006, 16:45-60.

[24] Life technologies by a Thermo Fisher Scientific Brand, https://www.lifetechnologies.com/it/en/home/life-science/cell-analysis/labeling-chemistry/fluorescence-spectraviewer.html?ICID=svtool&UID=1398dna_3

[25] S.Tsai , Y. Chen and J.Liaw. Compound Cellular Imaging of Laser Scanning Confocal Microscopy by Using Gold Nanoparticles and Dyes. *Sensors*. 2008, 8*:* 2306-2316.

Chapter 5

Detection of gold nanoparticles aggregation growth through Laser Scanning Confocal Microscope

5.1 Introduction

Individual particles and assemblies of GNPs show different optical and electrical properties. For instance, the colour change due to aggregation of GNPs is an indicator of the surface plasmon shift, allowing potential applications in sensors to recognize DNA or its components [1].

Life processes strongly depends on nucleic acids and proteins, which therefore are used as probe for measurements of other components in biological systems [2]. The development of nanobiotechnology is helped by a deep understanding of the interaction of GNPs with nucleic acids, which are used as a basic tool for nanobiotechnological devices [3-4].

Examples of this approach are the organization of metal and semiconductor nanoclusters [5], several bioanalytical techniques [6], the biomolecular electronics [7] and nanomechanical systems. Therefore, the DNA efficiency for inducing GNPs self assembly is a very interesting subject of research. J. Yang et al [8] demonstrated how single stranded DNA could be used to manage the placement of two different sized GNPs in a complex particle system. K. N. Ganesh et al [9] have studied electrostatic assembly of cationic surfactants-capped GNPs on DNA duplex. H. Nakao et al [10] have reported the highly ordered assemblies of GNPs in well-aligned and long-range order on DNA molecules.

Colour change, UV-VIS spectroscopy and dynamic light scattering have been used as techniques for the detection of GNPs aggregation [11-13]. Confocal and two photon microscopies and single-cell plasmonically-enhanced Rayleigh-scattering imaging spectroscopy were used as imaging techniques to observe the GNPs aggregation after their accumulation within living cells through endocytosic processes [14-16]. These approaches take advantage of the characteristic optical properties of plasmonic GNPs, namely, their ability to strongly scatter light, and the coupling of their plasmonic fields when particles come into close proximity.

In this work, the laser scanning confocal microscopy (LSCM) is used to observe the double stranded DNA induced aggregate growth of cationic surfactants-capped GNPs. The observation based on the light scattering enhancement from GNPs aggregates is not enough in our experiments since there is a strong overlap between the light scattering from DNA/cationic surfactants complexes and the light scattering from GNPs aggregates. Therefore, to skirt this overlap problem we detected the GNPs aggregation through the Förster Resonance Energy Transfer (FRET) process. Nile Blue perchlorate (NB) is used as probe because in addition to the NB molecules ability to be intercalated inside the DNA helix [17,18], it seems that this probe can be also entrapped within the hydrophobic part of the surfactants bilayer films coating the aggregated GNPs. This entrapment place this probe at proximity to metallic surfaces leading to FRET. Due to the strong GNPs absorption light at around the plasma resonance a highly quenching fluorescence is produced allowing the localization of GNPs aggregates.

5.2. Preparation of Samples and Methods

5.2.1 Gold nanoparticles

Our experiments are performed by using the commercially GNPs obtained from Sigma Aldrich. Their proprieties were explained in details in the previous chapter.

5.2.2 Preparation of the DNA solution

Nucleic acid solution was prepared by dissolving 10 mg of commercially available deoxyribonucleic acid (double-stranded (ds) molecule), DNA, fish sperm from salmon testes (Sigma-Aldrich) in 10 ml of doubly distilled water. 24 hours or more were needed for the dissolution at 4°C, accompanied by occasional gentle shaking.

5.2.3 LSCM measurements

The fluorescence of NB is very sensitive to the hydrophobicity of the environment. R. K. Mitra et al [17] reported studies on the nature of binding of a small ligand/drug Nile blue (NB) with sodium dodecyl sulfate (SDS) micelles, bis-(2-ethylehexyl) sulfosuccinate (AOT)/isooctane reverse micelles (RM) and a genomic DNA extracted from Salmon sperm. When the polarity increases, the fluorescence of NB is red shifted due to the interaction of this dye with DNA. The planar hydrophobic phenoxazine moiety of NB is known to facilitate the intercalation of NB inside the DNA helix. It is also known that the NB can be electrostatically bound with the DNA surface at low DNA concentration. When the DNA concentration increases, the fraction of bound NB decreases and more NB molecules will interact with the DNA base pairs [17,18]. Whereas the location of this probe in the nonpolar core region of the micelles is indicted by an enhancement of the fluorescence and a blue shift [17].

For the observation of the GNPs aggregation growth induced by DNA based on the NB fluorescence analysis, four solutions were prepared. The DNA/GNPs/NB solution is prepared at first. We added to 1.6 g of the GNPs stabilized suspension in citrate buffer,

0.002 g of the crystallized probe Nile Blue A perchlorate (NB; Figure 5.1) purchased from Sigma-Aldrich. This mixture is left in a shaker for 15 minutes at 50°C in order to dissolve the probe. Then, 1.3 ml from the dissolved DNA was transported to the previous GNPs/NB mixture. The three other solutions were prepared for control experiments. The first one was prepared with the same procedure described above except that this mixture was free from DNA. To have the same concentration of GNPs in DNA/GNPs/NB solution described previously, 1.3 ml of double distilled water was added to GNPs/NB solution (solution N°1 for control experiments).

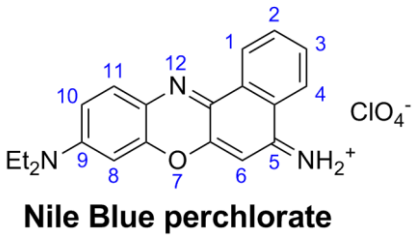

Figure 5.1. Molecular structure of the fluorescence probe NB.

To study the effect of GNPs on the fluorescence of NB bound to the cationic surfactants present as stabilizer in the GNPs suspension in citrate buffer, the solution N°2 was prepared with the same procedure described above for the GNPs/NB solution (solution N°1) except that GNPs were removed from the buffer solution by centrifugation at 3,000 rpm for an hour. The final solution for control experiments (solution N°3) was prepared by adding 0.002 g of NB to 1.3 ml from the dissolved DNA. Then, the resulting solutions were gently shacked at room temperature for 5 min, stored at 4°C for 48 hours, and 0.25 ml from each solution was deposited by drop coating to the glass slide treated by deionised water. The four coated films on substrate were stored for 24 hours at room temperature to let the water evaporate completely resulting to four precipitates.

(LSCM) was used to image the fluorescent emission on each of the four samples. All samples were imaged on a Leica TCS SP8 using a 25×/0.95NA water immersion objective and identical setting. The small droplet of the immersive water was placed on the opposite

side of the coated film on the glass slide with the thickness of 1.13 mm. The 514 nm was used as pump beam and the fluorescent emission was sent simultaneously to 2 PMTs (PMT1 and PMT2) collecting respectively the light in the (550-600) nm and (600-750) nm ranges. The excitation spectrum of NB has the (470-690) nm range [19]. Since the NB emission depends on the polarity of the environment, which is red shifted with higher polarity, emitted light was detected in (550-600) nm and (600-750) nm ranges [17]. The 514 nm was chosen for the irradiation. The use of two PMTs allowed the simultaneous acquisition of two images. In order to enhance the contrast, each image is colorized by an artificial colour, according to the detection ranges of PMT1 and PMT2, where the green or the yellow areas are the expression of the fluorescence from NB bound to the hydrophobic part of cationic surfactants and the red or the grey domains are the expressions of NB bound to DNA.

5.2.4 Scanning Electron Microscopy

The environmental scanning electron microscope (ESEM) Quanta 400F by FEI Company has been used, as in the previous experiment, to image the samples prepared with GNPs at pressure of 1 mbar and voltage 5-10 kV.

5.3. Experimental Results & Discussion

5.3.1 Images of LSCM and fluorescence spectroscopy

5.3.1.1 Effect of gold nanoparticles on the fluorescence of NB bound to cationic surfactants

The evaporation of the coated films prepared from the solutions N°1 and 2 induced respectively a precipitation of aggregated cationic surfactants complexes with and without GNPs. Before the dry of the coated film (solution N°2), NB as hydrophobic probe moves closely to the hydrophobic part of cationic surfactants [17]. As depicted in figure 5.2, the fluorescence spectra of the GNPs untreated precipitation recorded with the lambda scan mode across the 530-775 nm range under an excitation of 514nm shows a maximum at the

wavelength of 565.59 nm (grey curve, Figure 5.2). Under the same excitation, the fluorescence spectra of GNPs treated precipitation recorded with the lambda scan mode across the same range is broadened and slightly red shifted compared to fluorescence spectra in the absence of GNPs (orange curve, Figure 5.2). For the sample treated with GNPs, the evaporation of the solution induced their aggregation, which was expected since that the dipole-dipole interaction between these nanoparticles is stronger when the distance between them decreases. The SPR of GNPs presents a broadening and red shift when they aggregate [20]. Moreover, it seems that NB entrapment inside the hydrophobic part of the bilayer polymeric film covering aggregated GNPs is responsible of a FRET between NB (acceptor) and aggregated GNPs (donor), which explains the apparition of a second peak due to an enhancement of the light scattered in the 565.59-706.59 nm range from aggregated GNPs (Figure 5.2). In fact as explained in the second chapter, when a fluorophore is quite close to a plasmonic particle, for instance within 10 nm, and this fluorophore has an emission peak close to the plasma resonance peak, the quantum yield will decrease significantly due to the strong absorbance of GNPs, which results to a fluorescence quenching. In this case when GNPs aggregate, the SPR resonance is broadened and red shifted compared to dispersed GNPs. Thus, the emission maxima of NB coincides with the new SPR of aggregated GNPs. Around the SPR, the absorption and light scattering are at their maximum. Thus, the broadening and red shift of the fluorescence spectra of NB bound to cationic surfactants complexes is due in fact to the apparition of a second peak which corresponds to the enhanced light scattering form aggregated GNPs due to the FRET process.

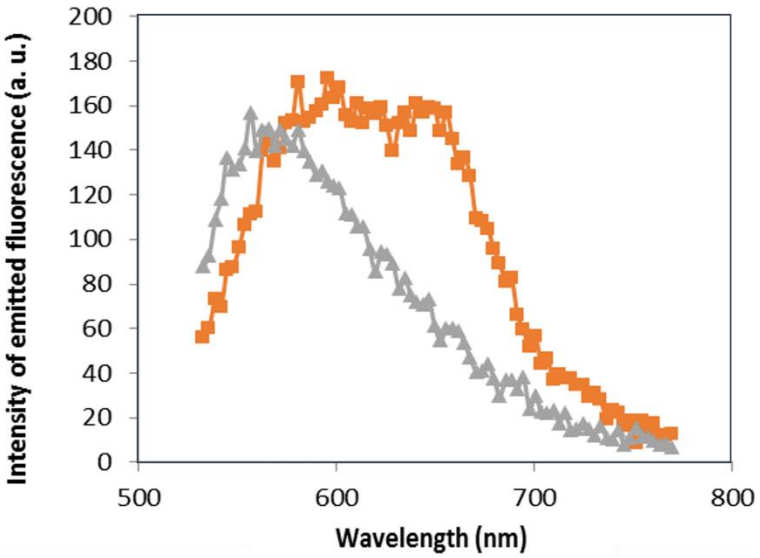

Figure 5.2. Effect of GNPs on the fluorescence spectra of NB bound to cationic surfactants complexes (grey and orange curves are recorded respectively from precipitations of aggregated cationic surfactants complexes without and with GNPs). Emission obtained from 514 nm excitation (lambda scan mode from a confocal microscope) and detected in the (530-775) nm range.

5.3.1.2 Effect of DNA on GNPs aggregation

In the previous paragraph we showed that the broadening and the red shift of the fluorescence spectra of NB bound to cationic surfactants complexes was an indicator of GNPs aggregation.

In the following paragraph, the effect of DNA on GNPs aggregation size will be discussed. As the DNA is concentrated (> 1mg/ml; solution N°3), the molecules were precipitated into liquid crystalline phase after the drying of the solution deposited via drop coating on the glass slide [21]. Figure 5.3 shows emitted fluorescence from NB bound to DNA molecules organized into the flower like texture which is a highly ordered liquid crystalline form of DNA [22], detected in the 550-750 nm range under the wavelength of 514 nm. As depicted in figure 5.4, the fluorescence spectra of NB bound to DNA molecules organized into liquid crystalline phase recorded with lambda scan mode from point marked as A is

red shifted compared to the fluorescence spectral of NB bound to cationic surfactants complexes (Figure 5.2). This shift is explained by the sensitivity of NB to the polarity of the environment. The hydrophobic part of cationic surfactants, where NB is placed is non polar whereas in the case of DNA stained with NB, there is an amount of this probe which is bound to the polar negatively charged phosphate backbone.

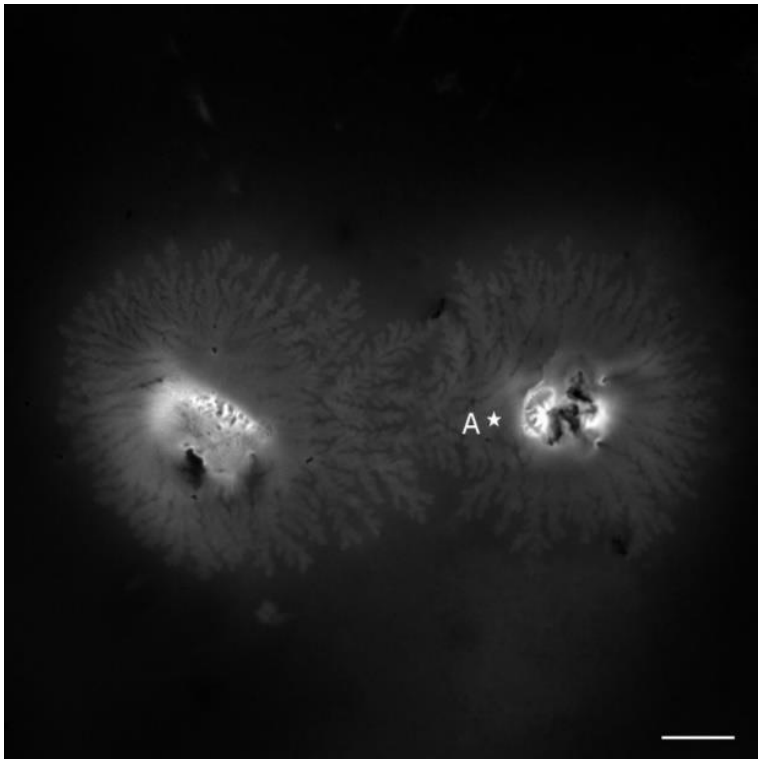

Figure 5.3. LSCM image of precipitated DNA (evaporated solution N°3). The 514 nm was used as pump beam and the fluorescent emission was detected in the (550-650) nm and (650-750) nm ranges. The scale bar indicates 40 µm.

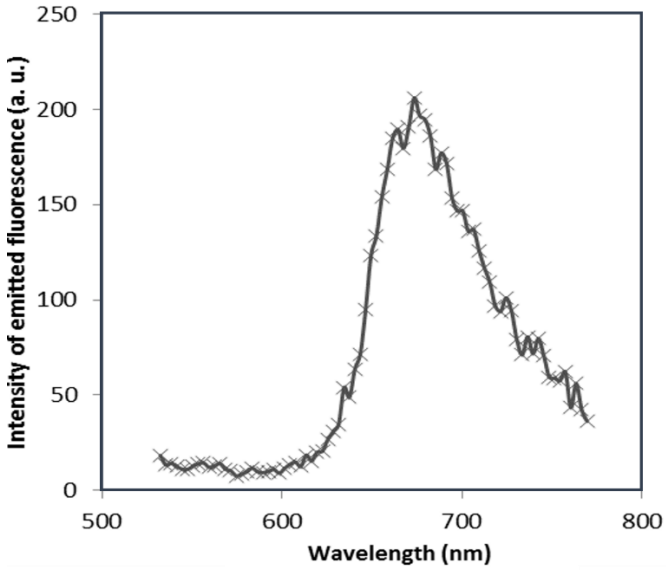

Figure 5.4. Fluorescence spectra of NB bound to DNA molecules organized into liquid crystalline phase recorded with lambda scan mode from point marked as A (Figure 5.3). Emission obtained from 514 nm excitation and detected in the (530-775) nm range.

Figure 5.5 shows the emitted fluorescence, detected in the (550-750) nm ranges, from precipitated dried DNA/GNPs/NB solution under the excitation wavelength of 514 nm. A strong emitted light enhancement (green and yellow regions in figure 5.5) is detected in the (550-560) nm range compared to untreated sample with GNPs (Figure 5.3 and 5.4). The emitted light detected in this range is attributed to an amount of NB entrapped inside the hydrophobic part of cationic surfactants stabilizing the GNPs suspension in citrate buffer. Moreover, as shown inside the region marked with the green colour in figure 5.5 (C), brighter spots are detected which suggested that GNPs are aggregated into spherical clusters. When NB are placed at proximity to GNPs surface, a light scattering enhancement is induced due to the FRET process. Also, GNPs plasmonic fields couple together when they are in close proximity [16]. For denser GNPs clusters, the plasmonic field coupling is increased, resulting in significantly higher absorption and higher light scattering [23], which induced a higher FRET and brighter signal.

As shown in figure 5.6 the fluorescence spectra recorded in point marked as a in figure 5.5 (B) is the same in point marked as A in figure 5.3. Whereas, the fluorescence spectra recorded in point marked as b in figure 5.5 (B) is broadened and blue shifted (Figure 5.6). As explained in the previous paragraph, the broadening of the fluorescence spectra is an indicator of GNPs aggregation. When GNPs are aggregated in the presence of DNA, an amount of NB inside the hydrophobic part of cationic surfactants bilayer film surrounding GNPs is responsible of the blue shift.

The fluorescence spectra recorded from aggregated GNPs in the presence of DNA (Figure 5.6, blue curve) is slightly red shifted compared to the fluorescence spectra recorded from aggregated GNPs without DNA (Figure 5.2, orange curve).

This red shift seems to be attributed to a growth of GNPs aggregation size induced by DNA compared to the spontaneous smaller GNPs aggregation induced by dipole-dipole interaction.

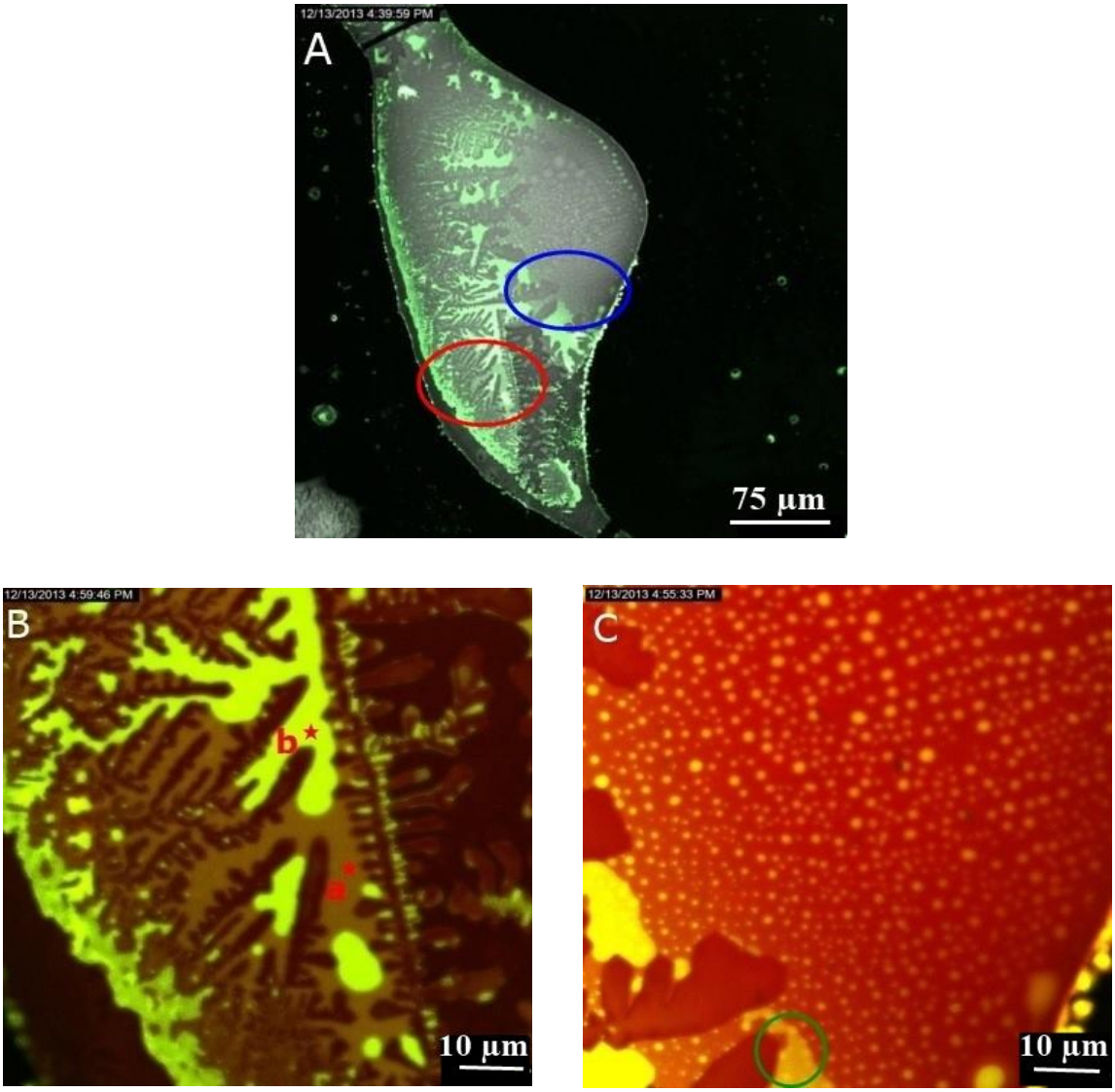

Figure 5.5. LSCM images of precipitated DNA/GNPs/solution. (B) and (C) are images of higher magnification at respectively the red and blue markets location in image (A). The 514 nm was used as pump beam. Light detected in (550-650) nm is green (Figure A, B) or yellow (Figure C) and light detected in (650-750) nm is red (Figure B, C) or grey (Figure A). The representation colours have been chosen to enhance the contrast.

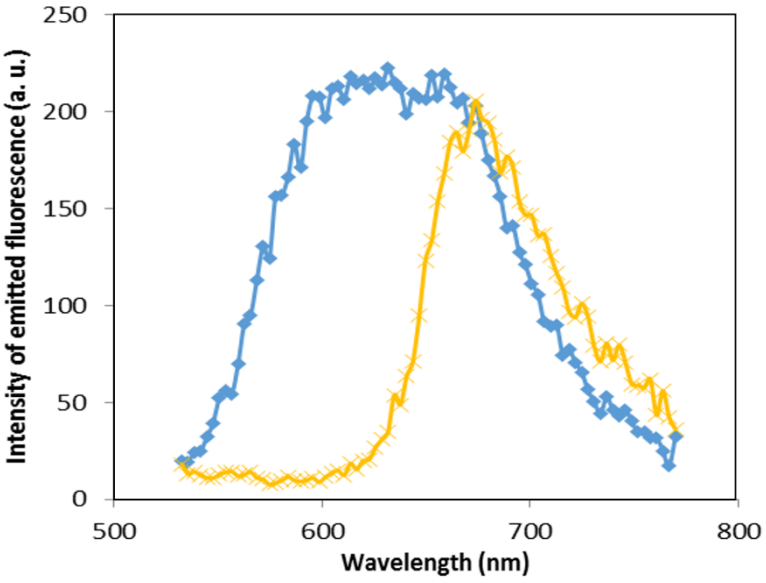

Figure 5.6. Fluorescence spectra of NB bound to precipitated DNA in the absence (yellow) and in the presence (blue) of GNPs aggregation recorded with lambda scan mode in respectively points marked as a and b in figure 5.5.B. The emission is obtained under an excitation of 514 nm and it is detected in the (530-775) nm range.

5.3.2 Images of ESEM

After their observations with confocal microscopy, the two precipitations of GNPs stabilized suspension in citrate buffer with and without DNA were stored at 4°C for 24 hours before ESEM observations. Figure 5.7 (A) shows that for the sample untreated with DNA, GNPs are aggregated into some clusters. As previously discussed, this self assembly is due to a dipole-dipole interaction between nanoparticles. In the presence of DNA, the GNPs aggregation size increased. GNPs are aggregated into denser three dimensional clusters (Figure 5.7 (B)). Moreover, for a higher magnification (100nm scale bar), GNPs are assembled in 3-D structures following the helix morphology of DNA (Figure 5.7 (C)).

This aggregation growth is due to electrostatic and hydrophobic interactions between positive charged hydrophobic head groups of the bilayer cationic surfactants film around GNPs and negative charged DNA phosphate backbone [9,24].

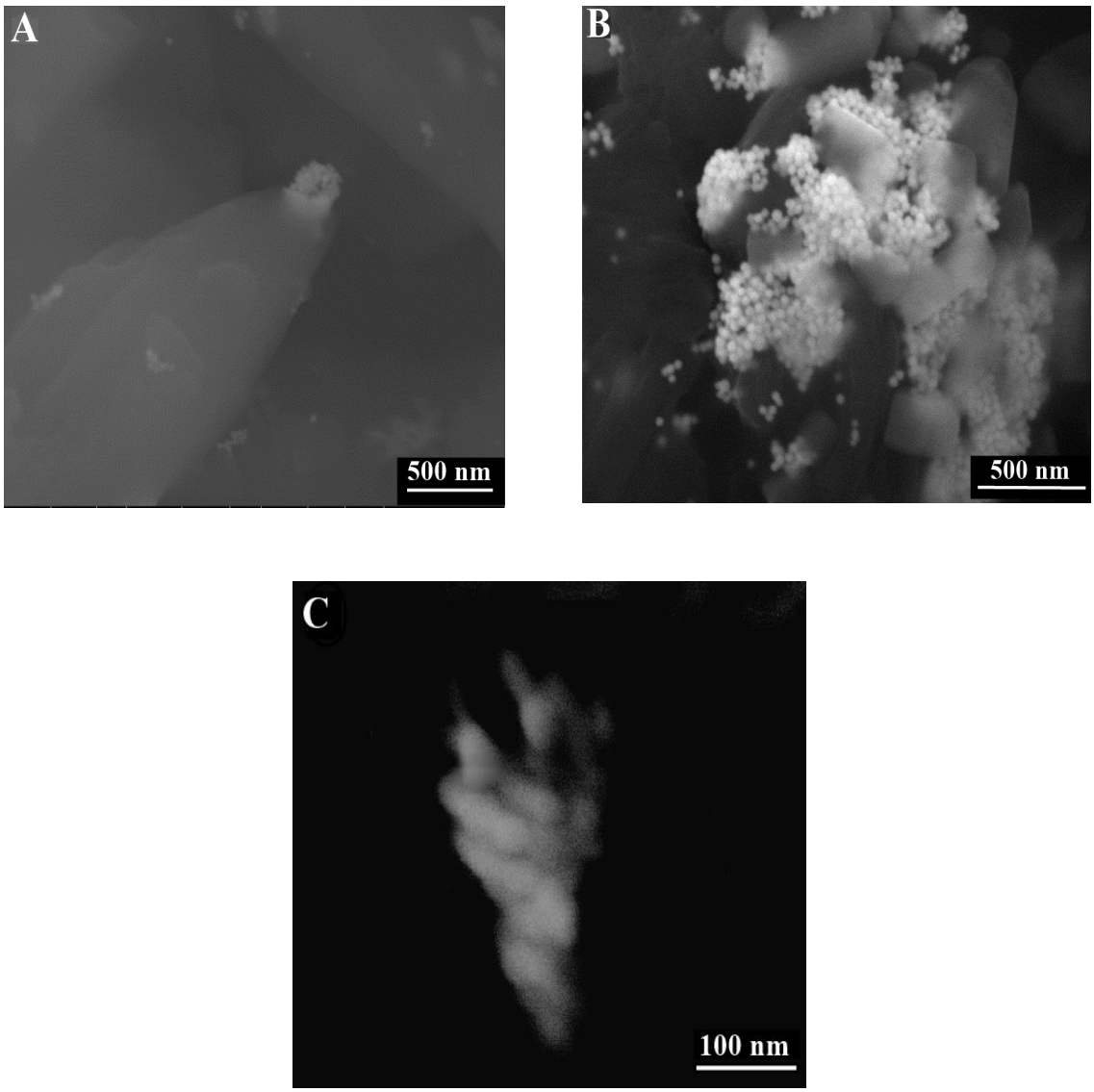

Figure 5.7: ESEM images of precipitates of evaporated; (A) GNPs stabilized suspension in citrate buffer, (B, C) DNA/ GNPs solutions.

5.4 Light scattering overlap problem

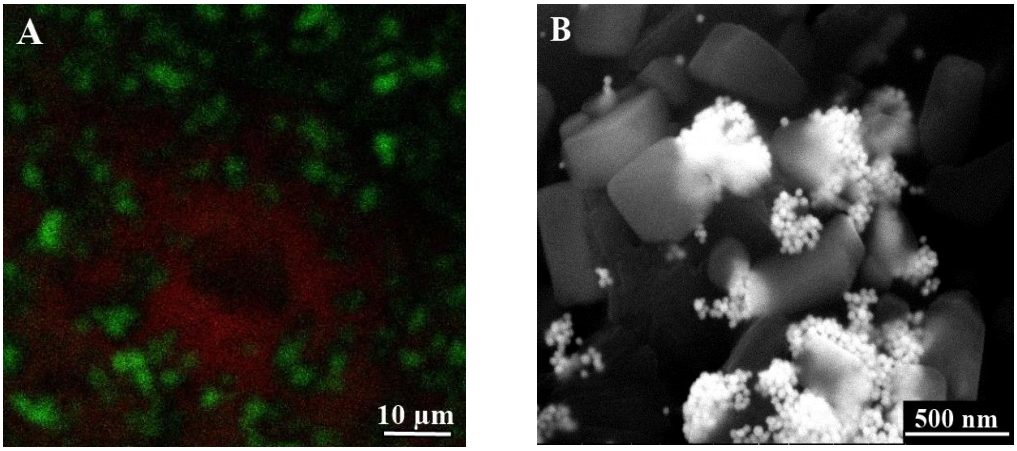

Figure 5.8: (A) LSCM image of precipitate of evaporated DNA/ GNPs solution. The 514 nm was used as pump beam. Green spots correspond to scattered light from CTAB/DNA complexes and GNPs aggregations. The red area corresponds to emitted light from NB bound to DNA molecules, organised in a liquid crystalline phase, detected in the (650-750) nm range. (B) ESEM image of evaporated DNA/GNPs solution. The DNA/CTAB complexes are in the form of cubic structures.

The excess of the CTAB amount introduced as stabilizer in the citrate buffer of GNPs suspension is responsible of a strong interaction of these surfactants molecules with DNA which induced CTAB/DNA complexes in the form of cubic structures as depicted in figure 5.8 (B). In addition to the strong light scattering from aggregated GNPs, the DNA/CTAB complexes also scatter light. This strong overlap makes impossible the detection of aggregated GNPs with the light scattering technique in the presence of CTAB and DNA compounds (Figure 5.8 (A)). Therefore, to skirt this overlap problem we detected the GNPs aggregation through the FRET process, observing the resulting enhanced fluorescence produced by GNPs aggregates.

5.5 Conclusion

In this chapter, FRET between GNPs (donors) and dyes (acceptors) is used for the detection of GNPs aggregation through LSCM. Moreover, DNA form salmon tests was tested for the GNPs aggregation growth. The fluorescence was manipulated with the SPR through the FRET process. The fluorescence spectra and peak are respectively broadened and shifted, which allowed the detection of the GNPs aggregation. In the presence of DNA, the fluorescence spectra is more red shifted due to the size increase of GNPs aggregation induced by DNA. This result is confirmed with ESEM images which showed also a GNPs assembly into denser clusters in the presence of DNA. Moreover, for a higher ESEM image magnification, GNPs are assembled in 3-D structures following the helical morphology of DNA. DNA induced a GNPs aggregation growth due to the electrostatic and hydrophobic interactions between positively charged head groups of cationic surfactants coating GNPs and negatively charged DNA phosphate backbone. Furthermore, these results may be helpful in the world of nanobiotechnology (gene delivery, cancer therapy…) mainly that the DNA-binding NB molecules is not toxic [17,18] and aggregated GNPs was usually detected via light scattering techniques, which can present problems since several structures within biological tissues scatter also light strongly. Thus, FRET between GNPs and dyes detected through LSCM result to be ideal for further bio application to discriminate aggregated GNPs and complex structures of tissue and cells.

References

[1] C.A. Mirkin, R.L. Letsinger, R.C. Mucic, J.J. Stohoff. A DNA-based method for rationally assembling nanoparticles into macroscopic materials. *Nature*. 1996, 382: 607-609.

[2] M. Rahban, A. Divsalar, A.A. Saboury, A. Golestani. Nanotoxicity and Spectroscopy Studies of Silver Nanoparticle: Calf Thymus DNA and K562 as Targets. *J. Phys. Chem. C.* 2010, 114 : 5798–5803.

[3] S. Basu, S. Jana, S. Pande, T. Pal. Interaction of DNA bases with silver nanoparticles: Assembly quantified through SPRS and SERS. *J. Colloid Interface Sci*. 2008, 321 : 288-293.

[4] M. Niemeyer, C.A. Mirkin . *NanoBiotechnology: Concepts, Methods and Applications*. Wiley-VCH, *Weinheim*. 2004.

[5] J.J. Storhoff, C.A. Mirkin. Programmed materials synthesis with DNA. *Chem. Rev*. 1999, 99: 1849 – 1862.

[6] C.M. Niemeyer. Nanopartikel, Proteine und Nucleinsäuren: Die Biotechnologie begegnet den Materialwissenschaften. *Angewandte Chemie*. 2001, 113: 4254 – 4287.

[7] E. Braun, Y. Eichen, U. Sivan, G. Ben-Yoseph. DNA-templated assembly and electrode attachment of a conducting silver wire. *Nature.* 1998, 391:775 – 778.

[8] J. Yang, J.Y. Lee, T. C. Deivaraj. H.P. Too. Single Stranded DNA Induced Assembly of Gold Nanoparticles. *Singapore-MIT Alliance*. 2003.

[9] K.N. Ganech, M. Sastry, M. DNA-amine interactions: From monolayers to nanoparticles. *J. Indian Inst. Sci.* 2002, 82: 105-112.

[10] H. Nakao, H. Shiigi, Y. Yamamoto, S. Tokonami, T. Nagaoka, S. Sugiyama, T. Ohtani. Highly Ordered Assemblies of Au Nanoparticles Organized on DNA. *Nano Letters* 2003, 3 (10):1391-1394.

[11] J.S. Lee, M.S. Han, C.A. Mirkin. Colorimetric Detection of Mercuric Ion (Hg^{2+}) in Aqueous Media using DNA-Functionalized Gold Nanoparticles. *Angew. Chem*. 2007,119: 4171-4174.

[12] N. Kanayama, T. Takarada, M. Maeda. Rapid naked-eye detection of mercury ions based on non-crosslinking aggregation of double-stranded DNA-carrying gold nanoparticles. *Chem. Commun*. 2011, 47 : 2077-2086.

[13] R. De la Rica, M. Stevens. Plasmonic ELISA for the ultrasensitive detection of disease biomarkers with the naked eye. *Nat.Nanotechnol*. 2012, 7 : 821-824.

[14] S. Tsai, Y. Chen, J. Liaw. Compound Cellular Imaging of Laser Scanning Confocal Microscopy by Using Gold Nanoparticles and Dyes. *Sensors*. 2008, 8*:* 2306-2316.

[15] N.J. Durr, T. Larson, D.K. Smith, B.A. Korgel, K. Sokolov, A. Ben-Yarkar. Two-Photon Luminescence Imaging of Cancer Cells Using Molecularly Targeted Gold Nanorods. *Nano Letters*. 2007, 7 (4) :941-945.

[16] M. Aioub, B. Kang, M.A. Mackey, M.A. El-Sayed. Biological Targeting of Plasmonic Nanoparticles Improves Cellular Imaging via the Enhanced Scattering in the Aggregates Formed. *J. Phys. Chem. Lett.* 2014, 5, 2555−2561.

[17] R.K. Mitra, S.S. Sinha, S. Maiti, S.K. Pal. Interactions of Nile Blue with Micelles, Reverse Micelles and a Genomic DNA. *J Fluoresc.* 2008, 18, 423–432.

[18] R.K. Mitra, S.S. Sinha, S. Maiti, S.K. Pal. Sequence Dependent Ultrafast Electron Transfer of Nile Blue in Oligonucleotides. *J Fluoresc.* 2009, 19, 353–361.

[19] Oregon Medical Laser Center. Nile blue. Avalable on line : http://omlc.org/spectra/PhotochemCAD/html/068.html

[20] Q. Gao, Y. Zheng, C. Song, L. Lu, X. Tian, A. Xu. Selective and sensitive colorimetric detection of copper ions based on anti-aggregation of the glutathioneinduced aggregated gold nanoparticles and its application for determining sulfide anions. *RSC Adv.* 2013, 3, 21424–21430.

[21] F. Livolant. A. Leforestier. Condensed phases of DNA: structures and phase transitions. *Prog. Polymer. Sci*. 1996, 21:1115-1164.

[22] M. Saminathan, T. Thomas, A. Shirahata, C.K.S Pillai, T.J. Thomas. Polyamine structural effects on the induction and stabilization of liquid crystalline DNA: potential applications to DNA packaging, gene therapy and polyamine therapeutics. *Nucleic Acids Research.* 2002, 30, (17): 3722-3731.

[23] N.T.K. Thanh, A. Vernhet, Z. Rosenzweig. Gold Nanoparticles in Bioanalytical Assays and Sensors. *Springer Ser Chem Sens Biosens*. 2005, 3 :261-277.

[24] L. Sun, Y. Sun, F.X Zhang, T. Yang, C. Guo, Z. Liu, Z. Li. Atomic force microscopy and surface-enhanced Raman scattering detection of DNA based on

DNA–nanoparticle complexes. *Nanotechnology* 2009, 20: 125502-125514.

Chapter 6

Conclusion and perspectives

Three different biological samples have been successfully employed to demonstrate that the adequate choice of the combination of optical sectioning microscopies and the FRET as a fluorescent technique to countering pitfalls arising from spectral overlap between emitted signals from features within biological tissues depends on the thickness and the viability of the sample. In chapter 3, results of experiments carried out on human cornea under conditions close to *ex vivo,* were shown the feasibility of combining the SHG and TPEF microscopies integrated in the same setup to resolve collagen from autofluorescence in connective tissues of the stroma. In fact the SHG signal form collagen has been resolved from autofluorescent cells by introducing the adequate combined dichroic mirrors and filters in the optical pathway of the microscope before reaching the detection channel. As a result, multiphoton microscopy can be used to achieve in-depth 3-D high resolution bioimaging without invasive histologic procedures.

Whereas, for imaging thinner samples two-photon excitation microscopy does not provide significant advantages over confocal microscopy or other 3-D imaging techniques. In fact, the wavelength of light for two-photon excitation is approximately twice that for one photon excitation. Thus, the axial and lateral resolution will actually be worse for two-photon microscopy compared to a perfect confocal microscope with an equivalent microscope objective. The feasibility of using confocal microscope for imaging thin, fixed

and labelled tissues were demonstrated in chapter 4 and 5. Moreover, the FRET has been combined to LSCM technique as a fluorescent technique to enhance the contrast between the signal from target structures and the undesired signal. The FRET process was based in this work on the interaction between GNPs and fluorescent dyes. The theoretical reasoning presented in chapter 2, validated the experimental results in both of the chapters. In fact, results of the fluorescence enhancement and quenching experiments have been respectively expected in chapter 4 and 5 as predicted in chapter 2. The skeletal muscle cells have been tested as an example of thin and fixed tissue in chapter 4. When irradiating GNPs treated cells with an excitation beam with a wavelength within both of the SPR and the excitation spectra of the fluorescent dyes (FITC), the strong plasmonic field generated around GNPs excites the dyes resulting to an enhancement of the emitted signal from target protein (eNOS). The same combination of techniques has been used in the chapter 5. Except that, the FRET process was based on a quenching of fluorescence, which offered a great sensitivity for the detection of the GNPs aggregation growth induced by DNA. Dispersed and assemblies of gold nanoparticles (GNPs) show different optical and electrical properties. The SPR of aggregated GNPs is broadened and red shifted. The entrapment of the dyes within the bilayer film around GNPs places this probe at proximity to metallic surfaces. In addition to the proximity, the wavelength of dyes emitted signal maximum is close to the wavelength of the SPR maximum of aggregated GNPs. Thus, due to the strong GNPs absorption light at around the plasma resonance a highly quenching fluorescence is produced, allowing the localization of GNPs aggregates.

In this thesis, we have then, successfully showed the FRET efficiency on countering one of the biggest challenges during the microscopical examination of biological samples, which is the low contrast between the different parts or the various compartments.

GNPs result to be ideal to skirt the overlap problem within labeled samples. SPR of GNPs may be used for artificially manipulating fluorescence and, for instance, to improve biological imaging. Such a result seems to be ideal for further bio application for the discrimination between complex structures within tissues and cells. Moreover, a major focus of this thesis work, has significant potential for extending the range of the FRET

interaction and hence opening up a broader range of applications, as the use of the combination of GNPs and dyes within live tissue. In fact, the art of successful live-cell microscopy is finding the balance between image quality and cell vitality. The success of live-cell microscopy is very much dependent on minimizing or avoiding any toxic effect of light on the biological system under observation. Thus, for live tissues, which lack autofluorescence or noncentrosymmetric molecules, the treatment with the GNPs and dyes combination can help to overcome these hurdles thanks to the nontoxicity proprieties of GNPs.

The fluorescent emission intensity is proportional to the concentration of fluorescent dye, but there are practical limitations to this concentration. In fact, a very high concentration could have toxic effects, which decrease the viability or leave a large amount of nonspecific fluorescence. These pitfalls can be avoided by keeping a low concentration of fluorescent dye, giving arise to a low fluorescence intensity, that brings a low signal to noise ratio. Thus, the appropriate combination of GNPs and dyes can help to reduce these problems.

Much work should be accomplished to clarify more the theory of the plasmon-FRET interaction and to establish and characterize in detail the optimum experimental conditions for enhanced FRET in terms of GNPs size, shape and composition, FRET dyes, GNPs-dye separation and experimental configuration.

In our laboratory, experimental and theoretical investigations will be continued, in in order to improve the design rules for more efficient and adjustable plasmon-enhanced FRET platform, which can be used to extend the application fields for optical biosensors.

List of publications and conferences presentations

Publications

1. Ramla Gary, Daniela Amelio, Filippo Garofalo, Gia Petriashvili, Maria Penelope De Santo, Yuen Kwong Ip and Riccardo Barberi, «Endothelial-like nitric oxide synthase immunolocalization by using gold nanoparticles and dyes", *Biomedical Optics Express* 2015, 6, 12, 4738.
2. Ramla Gary, Giovani Carbone, Gia Petriashvili, Maria Penelope De Santo, and Riccardo Barberi ,«Gold Nanoparticles aggregation growth induced by Nucleic Acid through laser scanning confocal microscope", *Sensors* 2016, 16, 258.

Conferences presentations

1. "New Frontiers in Plasmonics and NanoOptics" Cetraro(CS)-Italy-16-20 June 2014 with a poster "Cellular Imaging of Laser Scanning Confocal Microscopy by Using Gold Nanoparticles and Dyes"

2. The conference of "Italian Soft Days 2014"Rome, La Sapienza University on September 17 and 18 with a poster "CTAB capped gold nanoparticles: high affinity with negative charged polymeric nanostructures".

3. The 3rd International Nanotech Conference and Exhibition, Nanotech Tunisia 2015, April 22-24, Yasmine Hammamet. With a poster " Nucleic acid Induced Assembly of Gold Nanoparticles"
4. "Nanoplasm 2016", Cetraro- 13-17 June, with an oral presentation (invited speaker) "Endothelial-like nitric oxide synthase immunolocalization by using gold nanoparticles and dyes".